



Christian Endres



**Terahertz Spectroscopy
of Dimethyl Ether**



Cuvillier Verlag Göttingen
Internationaler wissenschaftlicher Fachverlag

Terahertz Spectroscopy of Dimethyl Ether

Inaugural-Dissertation
zur
Erlangung des Doktorgrades
der Mathematisch-Naturwissenschaftlichen Fakultät
der Universität zu Köln

vorgelegt von

Christian P. Endres
aus Bergisch Gladbach

Köln 2009

Bibliografische Information der Deutschen Nationalbibliothek

Die Deutsche Nationalbibliothek verzeichnet diese Publikation in der Deutschen Nationalbibliographie; detaillierte bibliographische Daten sind im Internet über <http://dnb.d-nb.de> abrufbar.

1. Aufl. - Göttingen: Cuvillier, 2010
Zugl.: Köln, Univ., Diss., 2009

978-3-86955-554-6

Berichterstatter: Prof. Dr. T.F. Giesen
Prof. Dr. S. Schlemmer
Prof. Dr. P. Jensen

Tag der mündlichen Prüfung: 2. Dezember 2009

© CUVILLIER VERLAG, Göttingen 2010
Nonnenstieg 8, 37075 Göttingen
Telefon: 0551-54724-0
Telefax: 0551-54724-21
www.cuvillier.de

Alle Rechte vorbehalten. Ohne ausdrückliche Genehmigung des Verlages ist es nicht gestattet, das Buch oder Teile daraus auf fotomechanischem Weg (Fotokopie, Mikrokopie) zu vervielfältigen.

1. Auflage 2010

Gedruckt auf säurefreiem Papier.

978-3-86955-554-6

Abstract

Dimethyl ether (CH_3OCH_3) is one of the largest organic molecules detected in the interstellar medium. As an asymmetric top molecule with two methyl groups which undergo large amplitude motions and a dipole moment of $\mu = 1.3$ D, it conveys a dense spectrum throughout the terahertz region and contributes to the spectral line confusion in astronomical observations at these frequencies.

In this thesis, rotational spectra of dimethyl ether in its ground vibrational state and the two lowest excited torsional states $\nu_{11} = 1$ and $\nu_{15} = 1$ have been measured in the laboratory up to 2.1 THz and have been analyzed. About 15000 transitions have been assigned for the first time. They improve the dataset for the vibrational ground state considerably and provide comprehensive datasets for the torsional states. The analysis is based on an effective Hamiltonian for a symmetric two-top rotor and includes experimental data published so far. Frequency predictions are presented up to 2.5 THz for astronomical applications. They enabled the first interstellar detection of transitions within excited torsional states and so demonstrate the importance of the data. An important prerequisite for these measurements was the development of a new spectrometer, which extends the frequency coverage of the Cologne spectrometers considerably. This has been realized by the application of a novel type of frequency multiplier, a superlattice multiplier (SL), which has been applied in the field of high resolution spectroscopy for the first time. In combination with backward wave oscillators, multiplication factors up to 13 and frequencies up to 3.1 THz have been achieved and used to record spectra of rotational transitions of various molecules. The presented measurements confirm not only the effective generation of higher harmonics, but also the broadband use. Due to these properties SL devices are also well suited as mixer elements in heterodyne receivers. This has been proved by the assembly of a heterodyne receiver working at room-temperature. Further investigations using extremely sensitive THz-heterodyne receivers have been carried out in order to explore their potential in scope of future applications.

Kurzzusammenfassung

Dimethylether (CH_3OCH_3) ist eines der größten, bisher interstellar entdeckten, organischen Moleküle. Aufgrund der zwei Methylgruppen, die Großamplituden-Bewegungen durchführen, und einem Dipolmoment von $\mu=1.3$ D hat dieses asymmetrische Kreisel-Molekül ein dichtes Spektrum im gesamten Terahertz-Bereich. Es trägt daher erheblich zur Linienkonfusion in astronomischen Beobachtungen in diesem Frequenzbereich bei.

In dieser Arbeit sind Rotationsspektren von Dimethylether im Vibrationsgrundzustand und den niedrigsten angeregten Torsionszuständen $\nu_{11} = 1$ und $\nu_{15} = 1$ im Labor bis zu Frequenzen von 2.1 THz gemessen und ausgewertet worden. Mit fast 15.000 neu zugeordneten Übergängen konnte der Datensatz für den Vibrationsgrundzustand erheblich verbessert und ein umfangreicher Datensatz für die beiden Torsionszustände erstellt werden. Die Analyse basiert auf einem effektiven Hamiltonian für Moleküle mit zwei symmetrischen internen Rotoren und umfasst alle bisher veröffentlichten experimentellen Daten. Frequenzvorhersagen bis 2.5 THz für die Auswertung astronomischer Spektren wurden erarbeitet und ermöglichten die erste interstellare Detektion von Übergängen innerhalb der angeregten Torsionszustände. Eine wichtige Voraussetzung für diese Messungen war der Aufbau eines neuen Spektrometers, welches den Frequenzbereich der Kölner Spektrometer erheblich erweiterte. Dies gelang durch den Einsatz eines neuen Typs von Frequenzvervielfachern, so genannten Übergitter-Vervielfachern, die erstmalig in der hochauflösenden Spektroskopie eingesetzt wurden. In Kombination mit Rückwärtswellen-Oszillatoren sind Vervielfachungsfaktoren bis zu 13 und Frequenzen bis zu 3.1 THz erzielt worden. Dies wird anhand von Rotationspektren mehrerer Moleküle belegt und untersucht. Die vorgenommenen Messungen bestätigen nicht nur die effiziente Erzeugung hoher Oberwellen, sondern auch die Einsetzbarkeit über einen breiten Frequenzbereich. Aufgrund dieser Eigenschaften sind Übergitter auch hervorragend als Mischerelement in Heterodyn-Detektoren geeignet, was durch einen neu aufgebauten, bei Raumtemperatur arbeitenden Heterodyn-Detektor nachgewiesen werden konnte. Weitergehende Untersuchungen wurden mit höchstempfindlichen THz-Heterodyn-Empfängern im Hinblick auf einen zukünftigen Einsatz in der Laborspektroskopie durchgeführt.

Zusammenfassung

In dieser Arbeit werden Messungen und die Analyse von Rotationspektren von Dimethylether (CH_3OCH_3) im Vibrationsgrundzustand, als auch in den ersten angeregten Torsionszuständen vorgestellt. Die interne Rotation beider Methylgruppen führt zur Aufspaltung der Rotationsniveaus durch den Tunneleffekt. Gepaart mit einem relativ großen permanenten Dipolmoment erzeugt dies ein sehr komplexes Spektrum mit Übergängen im gesamten THz-Frequenzbereich. Dimethylether ist von großer astrophysikalischer Bedeutung, da große Vorkommen in Sternentstehungsgebieten beobachtet werden. Aufgrund der Komplexität des Spektrums hat es einen großen Anteil an den in astronomischen Spektren solcher Regionen beobachteten Übergängen. Die genaue Kenntnis des Rotationspektrums von Dimethylether ist daher von großer Bedeutung für das Verständnis und die Auswertung solcher Spektren.

Umfassende Messungen im gesamten mm- und THz-Frequenzbereich mit hoher Frequenzgenauigkeit sind eine Grundvoraussetzung für die Vorhersage präziser Übergangsfrequenzen. Für den Vibrationsgrundzustand existieren bereits umfangreiche Messungen, die sich allerdings auf den Frequenzbereich unterhalb von 550 GHz beschränken. Obwohl darauf aufbauende Frequenzvorhersagen bereits sehr genau sind, genügt die Frequenzgenauigkeit oberhalb von 1 THz nicht den gewünschten Anforderungen. Frequenzvorhersagen von Rotationsübergängen in angeregten Vibrationszuständen waren bislang nicht verfügbar, da der Datensatz experimentell bestimmter Frequenzen mit weniger als 32 Übergängen pro Zustand zu limitiert war.

Im Rahmen dieser Arbeit wurden deshalb Messungen im Frequenzbereich zwischen 38 und 2100 GHz mit verschiedenen Kölner Spektrometern durchgeführt. Zur Erschließung des Frequenzbereichs oberhalb von 1 THz war dabei der Aufbau eines neuen Spektrometers notwendig. Dies gelang durch den Einsatz eines so genannten Übergitters, das durch die effektive Erzeugung von Oberwellen der eingestrahlten Strahlung als Frequenzvervielfacher dient. Des Weiteren sind Spektren ausgewertet worden, die am Jet Propulsion Laboratory (JPL, Kalifornien) und an der Ohio State University in Columbus (Ohio) aufgenommen und für diese Arbeit zur Verfügung gestellt wurden. Insgesamt konnte der experimentelle Datensatz um etwa 15.000 Rotationsübergänge erweitert werden. Mit je knapp 5.000 Übergängen steht

damit auch erstmalig ein umfassender Datensatz für die beiden angeregten Torsionszustände bereit.

Die Auswertung der Spektren basiert auf einem effektiven Hamiltonian, der von Peter Groner für Moleküle mit zwei symmetrischen internen Rotoren entwickelt wurde. Auf diese Weise gelang es, einen präzisen Parametersatz für den Vibrationsgrundzustand zu bestimmen. Mit diesem Parametersatz konnten die gemessenen Rotationsübergänge bis zur experimentellen Genauigkeit angepasst und sehr exakte Frequenzvorhersagen für den gesamten Terahertz-Bereich bis 2.5 THz berechnet werden.

Auch für die Rotationspektren in den Torsionszuständen $\nu_{11} = 1$ und $\nu_{15} = 1$ konnten Parametersätze bestimmt werden. Es zeigte sich, dass eine erhebliche Anzahl von Energieniveaus durch Wechselwirkungen zwischen den Torsionszuständen gestört sind, was die Zuordnungen und die Analyse erheblich erschwerte. Dennoch konnte ein Parametersatz erarbeitet werden, der sowohl die Aufspaltung der Rotationsniveaus, als auch die Wechselwirkung beschreibt. Obwohl der Parametersatz die zugeordneten Übergangsfrequenzen nicht mit experimenteller Genauigkeit anpasst, konnten Frequenzvorhersagen für diese Zustände berechnet werden. Diese genügen größtenteils den Anforderungen, die für die Analyse astronomischer Spektren notwendig sind. Anhand der erstellten Frequenzvorhersagen gelang die erste astronomische Detektion von Rotationsübergängen in den angeregten Torsionszuständen.

Die durchgeführte Analyse der Wechselwirkungen ermöglichte erstmals die genaue Bestimmung des Energieunterschieds zwischen beiden angeregten Zuständen durch einen globalen Fit. Außerdem konnte die Potentialfunktion der Torsionsbewegung anhand der bestimmten Parametersätze verbessert werden, da sowohl die Tunnelaufspaltung der Torsionszustände, als auch experimentell bestimmte Torsionsübergänge gemeinsam angepasst werden. Neben den in dieser Arbeit erarbeiteten Daten verwendet die Anpassung auch die verfügbaren Literaturdaten, die sowohl Infrarot- als auch Raman-Messungen umfassen.

Im technischen Teil der Arbeit wird die Eignung des Übergitter-Frequenzvervielfachers als Strahlungsquelle in Spektrometern anhand von Rotationspektren verschiedener Moleküle untersucht. Übergitter-Vervielfacher erzeugen sehr effektiv hohe ungradzahlige Oberwellen der Eingangsstrahlung und lassen sich daher im gesamten THz-Bereich als Strahlungsquelle einsetzen. Erstmals wurde ein Spektrometer aufgebaut, das diese neuen Vervielfacher als Strahlungsquellen einsetzt. Oberwellen zwischen der dritten und der dreizenten konnten zur Messung von Spektren benutzt werden. Dadurch wird eine fast vollständige Frequenzabdeckung des Frequenzbereiches zwischen 240 und 3100 GHz erreicht. Des Weiteren wurden Heterodyn-Detektionsverfahren untersucht. Gerade in Kombination mit Vervielfachern ist diese Technik interessant, da sie eine extrem schmalbandige Detektion der Strahlung erlaubt und so eine selektive Detektion einer Oberwelle ermöglicht. Da diese hochempfindliche Detektionstechnik aber auch weitere interessante Optionen bietet, wurden verschiedene Empfänger bezüglich ihres Einsatzes

in der Laborspektroskopie ausgewertet. Mit hochempfindlichen Empfängern, wie sie an Teleskopen im THz-Bereich eingesetzt werden, wurden Emissions- als auch Absorptionsspektren im Labor aufgenommen und im Hinblick auf zukünftige Einsatzbereiche im Labor untersucht. Weniger empfindliche, dafür aber sehr kompakte, bei Raumtemperatur arbeitende Heterodyn-Detektoren wurden erstmalig auch mit Übergittern als Mischer aufgebaut. In Kombination mit Übergitter-Vervielfachern als Strahlungsquelle wurde mit diesem Spektrometer eine Frequenzabdeckung von 250 bis 600 GHz erreicht. Mit verschiedenen Detektionsverfahren wurden Spektren in diesem Frequenzbereich aufgenommen und sind im Hinblick auf die Empfindlichkeit des Empfängers ausgewertet worden. Für zukünftige Anwendungen wurde die Grenzempfindlichkeit abgeschätzt und die verschiedenen Verfahren miteinander verglichen.

Contents

Abstract	i
Kurzzusammenfassung	iii
Zusammenfassung	v
1 Introduction	1
I Spectroscopy of Dimethyl Ether	7
2 Introduction	9
2.1 Astronomical Relevance	9
2.2 Previous Laboratory Work	10
3 Theory	13
3.1 General	13
3.2 Molecular Symmetry Group	14
3.3 Correlation Table	15
3.4 Selection Rules	16
3.5 Spin Statistic	17
3.6 Effective Rotational Hamiltonian	18
3.6.1 Separation of the Hamiltonian	19
3.6.2 Solutions of $H_I(K_1, K_2)$	22
3.6.3 Basis Transformation	25

3.6.4	Calculation of the Matrix Elements	26
3.6.5	Effective Hamiltonian for Dimethyl Ether	28
3.6.6	Discussion of the Hamiltonian	29
3.6.7	Determination of the Potential Function $V(\tau_1, \tau_2)$	35
3.7	Perturbations in Excited Torsional States	37
3.8	Level Crossings	37
3.9	Fitting Spectra and Calculating Transition Frequencies	39
3.10	The RIAS Approach	40
4	Observed Spectrum and Analysis	43
4.1	Experimental Details	43
4.2	Ground State Spectrum	44
4.3	Excited Torsional States	49
4.4	Astronomical Identifications	55
4.5	Torsional Potential Function	56
5	Conclusion	63
 II High Resolution THz Spectrometers: Techniques and Perspectives		67
6	Introduction	69
7	Cologne Spectrometers	73
7.1	Synthesizer and Multiplier Chains	73
7.2	BWO-THz-Spectrometer	74
8	Superlattice Spectrometer	77
8.1	The Superlattice Device	77
8.2	Spectrometer Setup	78
8.3	Spectra	79
8.3.1	Output Intensities at Higher Harmonics	80
8.3.2	Accuracy in Frequency	81
8.3.3	Broadband Scan of Methanol	82
8.3.4	Spectra above 1.5 THz	83
8.4	Conclusion	84

9 Heterodyne Detection Techniques	87
9.1 Principles of Heterodyne Detection	89
9.2 Detection with Superconducting Mixers	91
9.2.1 Receiver Noise Temperature	91
9.2.2 Experimental Setup	92
9.2.3 System Noise Temperature	93
9.2.4 Emission Spectra	96
9.2.5 Sideband Identification	100
9.2.6 Detection of Monochromatic Signals	100
9.2.7 Absorption Spectra	105
9.3 Detection with Superlattice Mixers	106
9.3.1 Experimental Setups	107
9.3.2 Continuum Detector	108
9.3.3 Double Heterodyne Detection	108
9.3.4 Bolometer	110
9.4 Conclusion	111
Conclusion and Outlook	115
III Appendix	117
A Useful Tables	119
Bibliography	123
Acknowledgement	133

List of Tables

3.1	Correlation table between the molecular symmetry group G_{36} and the point group C_{2v}	17
3.2	Symmetry of the nuclear spin wave functions.	18
4.1	Characterization of the different datasets used in the fit. . .	44
4.2	Spectroscopic parameters for DME in the vibrational ground state.	48
4.3	Characterization of the different datasets used in the fit. . .	49
4.4	Spectroscopic parameters for DME in its excited torsional states (10) and (01).	54
4.5	Partition functions for DME.	55
4.6	Dataset used in the potential function least-squares fit for DME.	60
4.7	Kinetic coefficients and potential parameters.	62
8.1	Intensities U of the CO measurements recorded with the low frequency BWO in combination with the SL I multiplier.	81
8.2	Center frequencies of the CO measurements.	81
8.3	Center frequencies of methanol at 1 THz measured with the SL I.	85
9.1	Receiver noise temperature T_{rec}^{DSB} for some selected heterodyne instruments.	92
9.2	Calculated and measured intensities derived from emission spectra.	97
9.3	Experimental frequencies and intensities of methanol.	99

9.4	Calculated and measured intensities derived from absorption spectra.	106
9.5	Calculated and measured intensities.	111
9.6	Sensitivity obtained with InSb Bolometers.	111
A.1	Permutation operations of the molecular symmetry group G_{36} .	120
A.2	Character table of G_{36}	121
A.3	Direct products of $G_{36} \otimes G_{36}$	122

List of Figures

1.1	Electromagnetic spectrum.	3
2.1	Stick spectrum of dimethyl ether.	10
3.1	Structure of dimethyl ether.	14
3.2	Spectrum of the ground state transition $J_{K_a K_c} = 14_{311} - 13_{410}$	19
3.3	Torsional splitting of energy levels with $K_c = J - K_a + 1$ in the vibrational ground state of DME.	30
3.4	Torsional splitting for Q-branch transitions with $K_a = 6 - 5$, and $K_c = J - K_a + 1$ in the vibrational ground state of DME.	31
3.5	Calculated energy levels of the torsional modes of DME as a function of the top-top coupling term F'	32
3.6	Calculated energy levels of the torsional modes of DME below and in the vicinity of the potential barrier to torsion $V_3 \approx 1050 \text{ cm}^{-1}$	33
3.7	Real part of the solutions $\Phi_{\nu\sigma_1\sigma_2}^{(0,0)}$ of the internal Hamiltonian $H_I(0,0)$	34
3.8	Imaginary part of the solutions $\Phi_{\nu\sigma_1\sigma_2}^{(0,0)}$ of the internal Hamiltonian $H_I(0,0)$	34
3.9	Localized functions $\theta_{\nu q_1 q_2}^{(0,0)}$ of the internal Hamiltonian $H_I(0,0)$	35
3.10	Solutions $\Phi_{\nu 00}^{(0,0)}$ of the internal Hamiltonian $H_I(0,0)$ for $\nu = 2, 9, 52$	36
3.11	Solutions $\Phi_{000}^{(K,-K)}$ of the internal Hamiltonian $H_I(K,-K)$ for $K = 20, 30, 50$	36
3.12	Crossing of the energy levels of the substate EE for $K_a = 11$ and $K_a = 12$ due to the torsional splitting.	38

4.1	Rotational transition ($J_{K_a} = 37_{24} - 36_{23}$) in the ground state of DME at 2.06 THz.	46
4.2	Torsional splitting for Q-branch transitions with $K_a = 5 - 4$, and $K_c = J - K_a + 1$ in the torsional excited state (01).	51
4.3	Torsional splitting for perturbed Q-branch transitions with $K_a = 6 - 5$, and $K_c = J - K_a$ in the torsional excited state (01).	52
4.4	Perturbation of the energy levels of the torsional excited state (01).	52
4.5	Tentative detections of the (10)-excited state of dimethyl ether in Orion KL.	57
4.6	Detail of the line survey of G 327.3-06.	58
7.1	Setup of the THz - Spectrometer.	74
7.2	Schematic of the BWO.	76
8.1	I/V-Curve of a SL device.	78
8.2	Setup of the THz-Spectrometer with superlattice multiplier.	79
8.3	Relative intensities of rotational transitions in CO in dependence of the harmonic associated with this measurement.	82
8.4	Spectra of rotational transitions of CO recorded with different harmonics generated in the SL.	83
8.5	Broadband scan of methanol using the 7th harmonic generated by SL.	84
8.6	Spectra of ND ₂ H and D ₂ O recorded with BWO and SL.	86
9.1	Fundamental layout of a heterodyne receiver.	90
9.2	Schematic of the spectrometer setup using the CONDOR heterodyne receiver for detection.	94
9.3	System noise temperature T_{Sys} of CONDOR.	94
9.4	System noise temperature T_{Sys} of the NANTEN 2 test receiver.	95
9.5	Emission spectra of D ₂ O.	96
9.6	Relative rms noise in dependence of the integration time.	98
9.7	Emission spectrum of methanol.	98
9.8	Separation of sidebands.	101
9.9	Schematic of the absorption spectrometer setup using the CONDOR heterodyne receiver for detection.	102

9.10 IF-Signal of 17 th Harmonics generated by the SL.	103
9.11 Signal of the 17 th harmonic generated by the SL multiplier.	104
9.12 Absorption spectrum of D ₂ O recorded with the CONDOR heterodyne system.	106
9.13 Schematic setup of the SL heterodyne spectrometer.	108
9.14 Rotational transition within the vibrational groundstate of DME.	109
9.15 Schematic setup of SL heterodyne spectrometer using a second mixer.	110
9.16 Absorption spectra of DME.	110

1

Introduction

Terahertz (THz) radiation is located in the electromagnetic spectrum between the microwave and the far infrared region at wavelengths between 1 mm and 0.1 mm. Just like other spectral regions, the complementary properties of THz radiation enable a large field of unique applications. A wide variety of non-conducting materials, such as paper, wood, plastic, ceramics and clothing are transparent at THz frequencies. As the photon energy is far below the ionization limit, THz radiation, unlike X-rays, is non-destructive, yet well-suited for imaging as the wavelength is small enough to provide spatial resolutions below 1 mm. These properties make THz frequencies attractive for use in the field of material testing, security applications, medical and biological imaging. In particular, scientific applications are of inestimable value, because this frequency domain is best suited to study a variety of physical processes. Astronomers, chemists as well as earth, planetary and space scientists have been applying THz technology for over 25 years to measure, catalog, and map thermal emission lines for a variety of light-weight molecules. In this part of the spectral region, chemical species provide an exceptional amount of information. The wavelength range corresponds to an equivalent black body temperature between 14-140 K. Thus, the radiated power of cold interstellar dust (<100 K) is largest at these frequencies. Thousands of individual spectral lines can be distinguished and provide deep insights into the composition of dark clouds, which are opaque at higher frequencies.

Despite the great opportunities provided in this field, the THz frequency region is still one of the most unexplored regions in the electromagnetic spectrum. Powerful radiation sources have been practically non-obtainable, and only due to the tremendous efforts during the last years, more and more monochromatic, tunable and compact radiation sources have become available. THz radiation, often also referred to as sub-mm-waves, is at the interface between electronics and photonics. The attempt to apply techniques, known from the bordering frequency regions of the microwave and the infrared, is still accompanied by a drastic drop of output power, which is often called the “THz-gap”. Nevertheless, a number of radiation sources are

now available, which has made a variety of applications feasible and has triggered numerous commercial activities in this field. Besides the limited output power of radiation sources, most applications are hampered by the strong absorption features of water all over the THz range. The transmission is already drastically reduced by air humidity. That is why extremely dry environments are a prerequisite for most applications. Since the beginning of radio-astronomy, enormous efforts have been made to steadily increase the frequency region of telescopes, and nowadays a growing number of telescopes is ready to explore the THz frequency region. Telescopes, such as the Caltech Submillimeter Observatory (CSO), the James Clark Maxwell Telescope (JCMT), the Submillimeter Array (SMA) and satellite based facilities like the Submillimeter-Wave Astronomy Satellite (SWAS) as well as the Infrared Space Observatory (ISO), are operating successfully and have been important milestones on the way to accessing even higher THz frequencies. The enormous activities are also reflected by the number of next generation telescopes. APEX (Atacama Pathfinder Experiment) has recently started its scientific operation. Built as a pathfinder experiment for the large interferometer ALMA (Atacama Large Millimeter Array), it enables measurements in the atmospheric window at around 1.3 THz. Just like ALMA, it is located in the Atacama desert in Chile, in large heights and an extremely dry environment - perfect conditions for THz measurements. With an array of about 66 antennas, ALMA will set new standards in spatial resolution, frequency coverage and sensitivity. To access frequencies, which are not accessible from ground based observations, the observatories SOFIA (Stratospheric Observatory for Infrared Astronomy) and the space observatory Herschel have been developed. The Hifi receiver on board of Herschel, which has recently been successfully launched, covers frequencies up to almost 2 THz. In addition the airborne observatory SOFIA will start its operation within the next years, granting observations at high THz frequencies in heights where atmospheric absorption is largely reduced.

As indicated in Fig. 1.1, rotational transitions and low lying vibrational transitions of molecules are located at THz frequencies. The uniqueness of rotational spectra of molecules plays an essential role in the identification of molecules in interstellar objects. Therefore, rotational spectra are often designated as “fingerprints” of molecules. This frequency region is hence particularly suited to study cold interstellar objects, where usually only rotational levels of molecules are populated. Objects such as dark clouds, prestellar cores and protostars play an important role in the evolution of stars. Studying the interstellar spectra of molecules does not only provide information about the chemical composition of astronomical objects, it also provides important clues about the physical condition and its environment. These analysis require a comprehensive understanding of the spectra of the involved molecules. Accurate rest frequencies and line intensities are essential prerequisites for the detection of molecules and the interpretation of astronomical spectra. An understanding of line profiles provides direct in-

formation about the physical properties of the investigated object, such as molecular abundances, temperatures, and velocity structure.

As rotational transition frequencies scale roughly with the inverse of the moment of inertia, rotational transitions of light hydrides and their deuterated isotopomers are located at high THz frequencies. They are highly abundant in very cold interstellar environments (<20 K) where only the lowest energy levels are populated. Often only few of their transitions are detectable, mainly located in the THz range, as it is the case for molecules, such as HD, H_3^+ , CH_2 . Some individual transition frequencies are of exceptional interest, such as the $J_{K_a K_c} = 1_{01} - 0_{00}$ transition of para- H_2D^+ , which provides important information for understanding deuterium fractionation. Low lying vibrational transitions, which are usually large amplitude motions or bending motions, are also located in the THz region. Important examples are the bending modes of linear molecules, such as those of pure carbon chains (C_3 , C_4 , ...). Due to the lack of a permanent dipole moment, some linear molecules do not have a pure rotational spectrum. In these cases, their unambiguous detection is only feasible via rovibrational transitions. The frequency resolution provided within the THz range allows to obtain their rotationally resolved spectrum. Most molecules show rotational transitions within the whole microwave and THz region. In chemically rich interstellar environments, such as hot core regions, the rotational temperatures of molecules is usually between 100-200 K. At these temperatures, the most intense rotational transitions occur at around 1 THz. In order to study the chemical composition of interstellar objects, astronomers record spectra with very broad frequency ranges. These line surveys often show an immense density of spectral features, and in most cases molecular lines overlap and blend into each other. A large fraction of lines in surveys is caused by just a few molecules, which obey complex spectra.

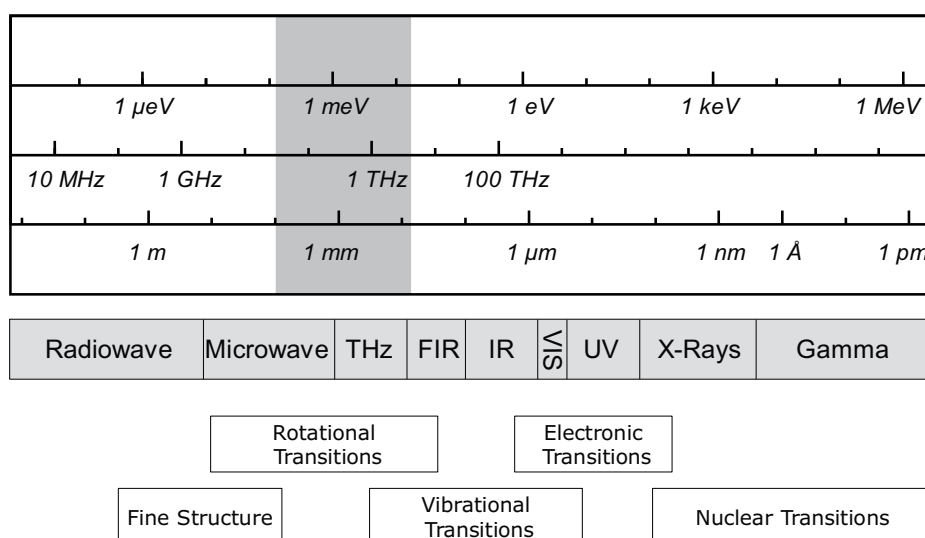


Figure 1.1: The electromagnetic spectrum and the molecular processes related to the different spectral regions.

As mentioned above, the knowledge of accurate rest frequencies is indispensable in order to decode astronomical spectra. This requires a comprehensive understanding of the rotational spectrum of each single molecule. The analysis of rotational spectra also provides important insights in the properties of molecules, such as structures, molecular bonds, inter-molecular forces, and processes. This is what laboratory spectroscopists aim to understand. Usually, quantum chemical models are applied to analyze experimental data and are an important tool to interpolate the experimental data to an extended frequency region. The quality of predicted transition frequencies strongly depends on the quality of the theoretical model and requires accurate experimental measurements. Usually, measurements within the entire frequency domain have to be carried out to access a sufficient number of energy levels to constrain the theoretical parameters to experimental values.

Many molecules, which obey complex spectra, have attracted the scientific interest for many decades, but a comprehensive analysis of their spectra still presents a challenge from the theoretical as well as the experimental point of view. In many of these molecules, atomic assemblies undergo large amplitude motions by which the positions of the atoms vary according to the order of atomic distances. This complicates the quantum mechanical description considerably. In the astronomical context, molecules with complex spectra also pose an enormous challenge. Although many of them are unambiguously identified, the complexity of their spectrum and the spectral density of lines often hamper an accurate interpretation of the spectral features in astronomical spectra. In order to lift this line confusion, it is essential to know accurate rest frequencies over the entire spectral range.

In dimethyl ether (DME), which is the subject of the present thesis, the internal rotation of two methyl groups are large amplitude motions. DME is highly abundant in star forming regions and known to cause a large fraction of the observed lines in astronomical spectra. Although DME is one of the simplest molecules with two internal rotors, it has not yet been possible to accurately describe all spectral features. The analysis of its spectra is therefore well suited to develop new theoretical concepts and verify their quality for the class of molecules with internal rotors.

Laboratory observations in the THz frequency range are still a challenging task as powerful, monochromatic radiation sources are rare. Frequency stability and accuracy of the applied sources are essential for the measurements. Therefore, radiation sources used in the spectrometers are phase-stabilized to a frequency reference signal. More and more radiation sources have been available over the last years, realized by various technical approaches. Most commonly, frequency multiplication techniques are applied, which are well established in the mm-wave region for decades. They maintain the frequency accuracy of the input radiation. As will be discussed in the present thesis, frequencies up to almost 3.1 THz have been accessed. The limited output power of all radiation sources in the THz range requires the application of very sensitive detector systems. The signal to noise level is mainly determined by the interplay of radiation source and detector system.

Outline of the thesis

The present thesis is divided into two parts dealing with major questions which arise in the field of THz spectroscopy. The first part concerns the spectroscopic investigations of dimethyl ether. This molecule plays a key role when it comes to understanding the spectra of complex molecules, in which molecular subgroups perform large amplitude motions. For the reasons outlined above, a comprehensive and accurate description of the rotational spectrum is also of central importance for the interpretation of current and future astronomical spectra in the THz frequency region. Technical developments have been a prerequisite for the underlying comprehensive measurements particularly at highest frequencies. As more extensive and general technical studies of the spectrometer setups have been carried out, they are treated separately in part two.

This thesis aims to present a comprehensive analysis of the pure rotational spectrum in terms of astrophysical relevance. This includes the entire spectral range starting from mm-waves up to above 2 THz. The analysis focuses on the lowest vibrational levels, which are the vibrational ground state and the two lowest excited torsional states of the molecule. Particular attention is paid to the theoretical aspects including the applied model of the effective Hamiltonian, symmetries and the potential function of the torsional motion.

The introduction to the investigation of the torsion-rotational spectra of DME (chapter 2) gives the astrophysical context and motivation of this work, as well as a summary of previous laboratory works. As DME has been studied for many decades and under a variety of aspects, this summary focuses only on the major contributions directly concerning this work. Thereafter, the theoretical approach, which is applied in the analysis of the spectra, is discussed in detail (chapter 3). The effective Hamiltonian and its implementation in the applied fitting routines is described as well as other relevant properties, such as symmetry, spin statistics, and perturbations. The observed spectrum and the analysis of the rotational spectrum within the vibrational ground state and the two lowest excited torsional states are presented in chapter 4. The chapter comprises the description of recorded spectra and assigned transition frequencies. Sets of spectroscopic parameters are derived within the analysis and are used to predict transition frequencies and their line intensities as well as the potential function of the internal rotation. Finally, the huge dataset of transition frequencies has been used to obtain the first clear interstellar detection of DME in its excited torsional states. Part I ends with a conclusion of the obtained results.

The second part presents spectrometer setups which have been developed and realized within this work. The general introduction of spectrometer setups used in the THz frequency range (Chapter 6) is followed by an overview of these spectrometers which are well established in the Cologne laboratories and which have been applied in order to record spectra presented in part I

(Chapter 7). The extension of the spectral range, achieved by the application of a novel frequency multiplier, a so-called superlattice multiplier (SL), is one of the main technical results presented in this thesis (chapter 8). The construction of the SL spectrometers has been the prerequisite for measuring the spectrum of DME at highest frequencies and recording broad band spectra in the Cologne laboratories. Besides the properties of the SL devices, the design of the spectrometer is described in detail. Investigations have been carried out concerning frequency accuracy, tunability, and output power. At the end of part II, the application of heterodyne detection technique in laboratory spectrometer setups is presented (chapter 9). This extremely sensitive detection technique is well known in context with astronomical receiver systems and opens up new perspectives in the field of laboratory spectroscopy. In these preliminary studies, a variety of setups have been realized. The obtained results deliver important information to realize future spectrometers and outline applications of interest. The thesis concludes with a summary of the main results of both parts.

Part I

Spectroscopy of Dimethyl Ether

2

Introduction

2.1 Astronomical Relevance

As with other highly saturated molecules, DME (CH_3OCH_3) is found in high abundance in star-forming regions such as the Orion nebula, at rotational temperatures of around 200 K [1, 2]. Since the first interstellar detection by Snyder *et al.* in 1974 [3] in emission from Orion, more than 200 transitions have been assigned to DME in various interstellar spectra which have led to unambiguous identifications. The formation process of DME still remains unclear up to now. Current gas-grain models assume that the surface reaction $\text{CH}_3 + \text{CH}_3\text{O} \rightarrow \text{CH}_3\text{OCH}_3$ is the most likely formation route in warm dense regions [4]. These models predict strong variations of the abundance during the evolutionary stage of the protostar [5]. Further studies on DME can therefore provide important constraints on the evolutionary cycle of large organic molecules and chemical pathways in these interstellar objects. The rich chemistry in those environments is also reflected in the complexity of astronomical spectra. The analysis of these spectra is mostly limited by line confusion rather than the background noise, and strongly depends on the knowledge of accurate rest frequencies of the major species present in the astronomical source. A significant fraction of the observed transitions belongs to a limited number of often saturated molecules such as methanol, $\text{CH}_3\text{CH}_2\text{CN}$, CH_3CHO , CH_3COOH , CH_3CN , SO_2 , and DME. Transitions of these molecules are distributed over the THz frequency region up to around 2 THz at temperatures of 150 K as shown in the calculated stick spectrum of DME in its vibrational ground state (black) and its lowest excited torsional states $(\nu_{11}, \nu_{15})=(10),(01)$ (red) (Fig. 2.1). The most intense transitions are found at 1 THz. Therefore, a complete understanding of these few species is essential in order to overcome line confusion concerning the first detection of more exotic species. Although the vibrational ground state contributes the most intense transitions, rotational spectra within excited states of these molecules also play an important role since low lying torsional modes in particular are often significantly populated.

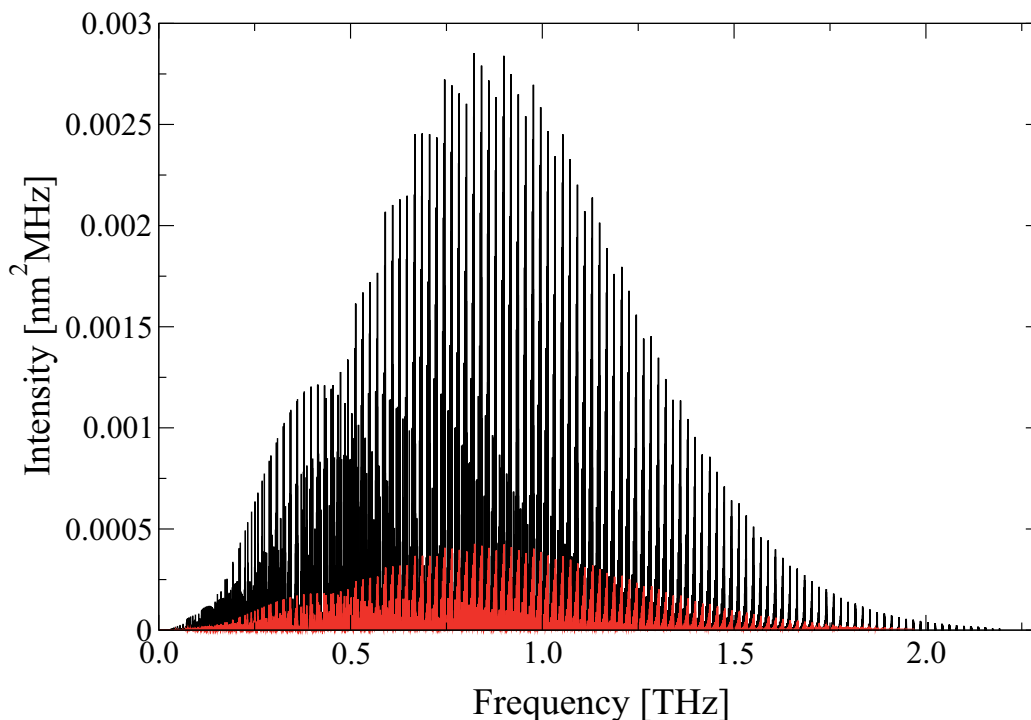


Figure 2.1: Stick spectrum of dimethyl ether in its vibrational groundstate (black) and its torsional excited states (10) and (10) (red). The value of the intensity is calculated for 150 K. The most intense transitions are found at frequencies of around 950 GHz.

New observatories such as ALMA (Atacama Large Millimeter Array) and Herschel will provide access to the THz region with greatly improved sensitivity. Thus, the need for accurate transition frequencies is substantially enhanced, especially in the THz range where the reliable spectroscopic data is still relatively poor. In addition, pure rotational spectra within excited vibrational states must be investigated, as the amount of accurate rest frequencies for these states is in most cases notably limited.

2.2 Previous Laboratory Work

The pure rotation-torsional spectrum of DME in its vibrational ground state has been studied in the laboratory for more than 40 years. Major steps towards its understanding were the derivation of symmetry properties and nuclear spin statistics by Myers *et al.* (1960) [6] and the determination of the structure and dipole moment by Blukis *et al.* (1963) [7]. By measuring a small number of microwave transitions, Durig *et al.* (1976) [8] were able to determine the potential barrier height to internal rotation. First predictions used for astronomical purposes were published by Lovas *et al.* [9] in 1979 in their review of the vibrational ground state transitions. They also included new measurements which were considerably extended by the work of

Neustock *et al.* (1990) [10]. The so far most comprehensive experimental work on the rotational ground state spectra has been published by Groner *et al.* in 1998 [11]. They measured and assigned another 1800 transitions and accessed frequencies up to 550 GHz and J quantum numbers up to 49. Their analysis was based on an effective Hamiltonian proposed by P. Groner [12]. The experimental dataset including all previously published rotational transition frequencies was reproduced within experimental uncertainties, and accurate frequency predictions up to 600 GHz were calculated. P. Groner already used this Hamiltonian to model the very limited dataset of rotational transitions within several excited states [12]. This dataset comprised around 30 transitions for each state published by Durig *et al.* (1976) [8] and Lutz *et al.* (1978) [13], which was by far insufficient to calculate accurate frequency predictions for astronomical purposes. Several of these transitions have been remeasured in 2004 by Niide *et al.* [14] as they investigated the terms in the internal rotation potential of DME.

Despite these extensive efforts, the quality of predicted rotational transition frequencies of DME for the THz region did not satisfy the needs of astronomers to accurately model current astronomical spectra. The objective of the present thesis is to improve the quality of predicted ground state rotational transition frequencies and to extend the experimental dataset to frequencies above 2 THz. In addition, the aim is to obtain frequency and intensity predictions within the first two torsional excited states in the same frequency range. A multitude of additional spectra have been recorded and analyzed from 38 GHz up to 2.1 THz accessing J and K values up to 70 and 30, respectively. The assigned transitions have been modeled using the same effective Hamiltonian model as in reference [12], and frequency predictions up to 2.5 THz have been derived.

3

Theory

3.1 General

Dimethyl ether (DME) is one of the simplest molecules having two methyl groups undergoing large amplitude motions. The internal rotation of both methyl groups combined with a relatively large dipole moment, causes a strong complex spectrum with a high spectral line density all over the THz region. Dimethyl ether is an asymmetric top molecule close to the prolate top limit. The degree of asymmetry is quantified by Ray's asymmetry parameter $\kappa = -0.9218$, which runs from -1 for a prolate top to +1 for an oblate top. The structure of dimethyl ether in its ground state configuration is shown in Fig. 3.1. The dipole moment ($\mu = 1.302$ D determined by Blukis *et al.*[7]) coincides with the axis of symmetry (*b*-axis) and a moderately strong *b*-type spectrum is observed. Both methyl groups perform periodic large amplitude motions, i.e. internal rotations or torsional motions, around the respective *C* – *O* bond axes. This motion causes each rotational level to split into four substates due to the tunneling effect, which complicates the spectra. As the barrier to torsion is relatively high ($V_3^{eff} \approx 915$ cm⁻¹, see Tab. 4.7), the size of this splitting is in the order of several MHz in the vibrational ground state. As the two torsional modes ν_{11} and ν_{15} are large amplitude vibrations, they are low-frequency modes, and their fundamental transitions are found at 200 cm⁻¹ and 240 cm⁻¹, which is considerably below the frequency of the fundamental transition of the COC-bending mode ν_7 (412 cm⁻¹) [15]. In the following sections, the symmetry properties of DME will be discussed and used to derive the spin statistic. Thereafter an effective Hamiltonian will be introduced on which the analysis of the spectra is based on. Properties of the wavefunctions and the influence of the potential on the energy levels will be discussed at the end of this chapter.

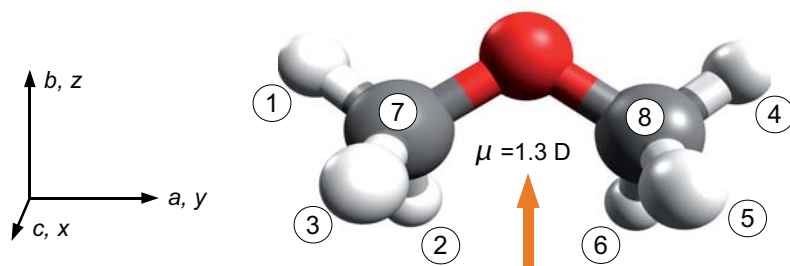


Figure 3.1: Structure of dimethyl ether.

3.2 Molecular Symmetry Group

Dimethyl ether has two methyl groups which perform large amplitude motions. In the limiting case of a rigid frame, the point group, which describes the molecular symmetry, is C_{2v} . Among the identity operation, it contains just the 2-fold rotation around b , and two reflections through the planes ab , and bc . In this and in any other point group, there are no appropriate operators to express the rotations of the internal tops around the C-O bonds making point groups an improper choice for the description of the complete symmetry. In literature, many different approaches can be found how to set up groups having operators reflecting the rotations of the internal tops [6, 16, 17]. The molecular symmetry groups, which are subgroups of the permutation inversion groups, are always a suitable choice since any symmetry can be represented by permutation operators.

The permutation inversion (CNPI) group of dimethyl ether consists of $6! \cdot 2! \cdot 2 = 2880$ operations. All unfeasible operations like operations which interchange only parts of the methyl groups, have to be removed in order to derive the molecular symmetry group. Feasible operations are operations isomorph to the C_{2v} group and operations which rotate the internal tops as well as combinations of both. The molecular symmetry group derived in this manner is G_{36} . The 36 group operations are summarized in Tab. A.1 referring to the labeling scheme of the nuclei indicated in Fig. 3.1. The internal rotation of the tops is best described by introducing the angles τ_1 and τ_2 , which are the angles of rotation of each top in a clockwise manner. The axis of rotation points from the carbon towards the oxygen nuclei. Since both internal rotors are equivalent, it is useful to symmetrize the angles and to introduce $\tau^+ = \frac{1}{2}(\tau_1 + \tau_2)$ and $\tau^- = \frac{1}{2}(\tau_1 - \tau_2)$. One big advantage of the molecular symmetry groups is that the symmetry group can be deduced without the knowledge of the Hamiltonian, whereas other approaches consider symmetry operations on the Hamiltonian to derive them. The molecular symmetry group is isomorphic to the $C_{3v}^- \otimes C_{3v}^+$ group derived in the work of Myers *et al.* [6]. The character table of the molecular symmetry group G_{36} , which is also applicable for acetone, is shown in Tab. A.2. The common labeling

of the substates of dimethyl ether with AA , AE , EA , and EE refers to the $C_{3v}^- \otimes C_{3v}^+$ group, which has the form of a direct product of two simple groups. The characters of this group can easily be derived from the character table of the C_{3v} group, which has the irreducible representations A_1 , A_2 and E . The operators in C_{3v}^- leave τ^+ invariant, whereas τ^- is invariant under the operations of C_{3v}^+ . This notation is commonly used to label the symmetry of the substates in dimethyl ether. The transformation properties of τ^+ and τ^- under the operations of G_{36} is given in Tab. A.2 in order to derive the correlation between the irreducible representations of both groups.

3.3 Correlation Table

Investigating the limiting cases of a rigid molecule, where the barrier to internal rotation is sufficiently high to neglect tunneling, and the limiting case of free rotation of both internal tops gives insight into the nature of energy levels. In the first case the molecule is considered to be rigid, and the symmetry can be described by the point group C_{2v} , because the internal rotation operations are not feasible. In the case of free rotation these operations are obviously feasible and only G_{36} gives the correct description of symmetry. It is useful to set up a correlation table which connects the irreducible representations of both groups. Considering only the characters of the irreducible representations of G_{36} for the operations of C_{2v} the derivation of this correlation table is straightforward. The operation (14)(25)(36)(78) corresponds to the rotation C_2 , (14)(26)(35)(78)* corresponds to σ_{bc} and (23)(56)* to σ_{ab} . If irreducible representations of G_{36} are now expanded as direct products of irreducible representations of C_{2v} , the correlation table, shown in Tab. 3.1, is obtained. Each irreducible representation in C_{2v} consists of the irreducible representations AA , AE , EA , and EE using the conventional labeling described above. If the barrier to internal rotation is sufficiently high but tunneling can not be neglected anymore, the degeneracy is removed and the levels will thus split into four substates AA , AE , EA , and EE . This is the case for the ground state of dimethyl ether. Upon approaching the barrier the splitting will get larger until the separation will be too large in order to describe the torsional levels in terms of C_{2v} symmetries. In general, the Hamiltonian is not separable into the motions of overall rotation, internal rotation and vibrations, because the rotational wavefunctions and vibrational coordinates depend more or less strongly on the coordinates of the large amplitude motions. Only the total wave function can be classified in terms of the irreducible representations of G_{36} . Nevertheless, as long as the barrier is high enough, the separation into the different motions and their separate descriptions in terms of symmetry is nearly good. In the following the rotational part and torsional part is separately investigated in terms of symmetry and selection rules are derived for the pure rotational transitions.

3.4 Selection Rules

The selection rules for the pure rotational transitions can be derived using the direct product table $G_{36} \otimes G_{36}$. The direct product of the states involved in the transitions have to include the electric dipole representation Γ^* , which is A_3 (invariant to all permutations and changed sign under E^*) [17].

$$\Gamma'' \otimes \Gamma' \supset \Gamma^* \quad (3.1)$$

Thus pure rotational transitions can occur only within the substates AA , AE , EA , and EE and between the states $A_1 \leftrightarrow A_2$ and $B_1 \leftrightarrow B_2$ (C_{2v}). In the vibrational ground state (A_1 symmetry) these transitions occur between rotational states

$$\begin{aligned} A_1 &\leftrightarrow A_2 & (ee \leftrightarrow oo) \\ \text{and } B_1 &\leftrightarrow B_2 & (eo \leftrightarrow oe) \end{aligned}$$

The letters denote, if K_a and K_c are even (e) or odd (o).

Similar considerations can be done for the excited torsional states. According to the internal motions expressed in the coordinates τ^+ and τ^- , there are two torsional modes which can be excited. Under the operations of the C_{2v} group τ^+ transforms as A_2 and τ^- as B_1 . In the A_2 torsion the two methyl groups oscillate in the same sense when viewed along the two-fold axis, that is at a given instant both will be turning clockwise or both counterclockwise. As the dipole moment lies along the two-fold axis, neither its magnitude nor its direction is altered by this motion. Therefore, the A_2 fundamental is forbidden in the infrared but Raman active. The B_1 torsion, i.e. when the methyl groups oscillate in the opposite sense, produces a net angular momentum along the a axis and thus a resultant oscillation of the dipole moment about this axis. Consequently, this transition is both infrared and Raman active [18]. In the ground vibrational mode the symmetry of the torsion-rotational wave functions are derived as a direct product of the torsional wave function and the pure rotational wave functions. Thus the selection for the A_2 mode are

$$\begin{aligned} A_1 &\leftrightarrow A_2 & (oo \leftrightarrow ee) \\ \text{and } B_1 &\leftrightarrow B_2 & (oe \leftrightarrow eo) \end{aligned}$$

and for the B_1 mode

$$\begin{aligned} A_1 &\leftrightarrow A_2 & (eo \leftrightarrow oe) \\ \text{and } B_1 &\leftrightarrow B_2 & (ee \leftrightarrow oo) \end{aligned}$$

Therefore the spin statistical weights are equal in the ground state and the A_2 state, but they are interchanged in the B_1 state.

Table 3.1: Correlation table between the molecular symmetry group G_{36} and the point group C_{2v} . The spin statistical weight for the rovibronic wave functions of DME is given in brackets

C_{2v}	G_{36}
A_1	$A_1(6) \oplus E_1(4) \oplus E_3(2) \oplus G(16)$
A_2	$A_3(6) \oplus E_2(4) \oplus E_3(2) \oplus G(16)$
B_1	$A_2(10) \oplus E_1(4) \oplus E_4(6) \oplus G(16)$
B_2	$A_4(10) \oplus E_2(4) \oplus E_4(6) \oplus G(16)$

3.5 Spin Statistic

The carbon and oxygen nuclei have spin 0, whereas the nuclear spin of hydrogen is $\frac{1}{2}$. Thus the total wave functions have to change sign under permutations which interchange an even number of hydrogen nuclei and have to be invariant, if an odd number of hydrogen nuclei or the carbon nuclei are interchanged. Using the transformation properties summarized in the character table (Tab. A.2), it follows that the total wave function has to be of A_2 or A_4 symmetry. In total, there are $2^6 = 64$ different nuclear spin wave functions, which can be symmetrized using the projection operator

$$P_{\Gamma_i} = \frac{1}{h} \sum_R \chi_{\Gamma_i}[R] \times R \quad . \quad (3.2)$$

h is the order of the group and χ_{Γ_i} is the character of the irreducible representation Γ_i of the operator R . The weight of a symmetry representation Γ_i can be calculated by

$$W_{\Gamma_i} = \dim(\Gamma_i)^4 \times \sum_{i_a, i_b, i_c, \dots} \sum_{i_{a'}, i_{b'}, i_{c'}, \dots} |\langle i_{a'}, i_{b'}, i_{c'}, \dots | P_{\Gamma_i}^2 | i_a, i_b, i_c, \dots \rangle|^2 \quad (3.3)$$

where $\langle i_a, i_b, i_c, \dots |$ are the unsymmetrized nuclear spin wave functions. Tab. 3.2 summarizes the symmetry of the nuclear spin wave functions and shows the occurrence of each irreducible representation in the function space spanned by the nuclear spin wave functions. One can easily derive the spin statistical weight of the rovibronic wave functions by calculating the direct product of irreducible representations of the nuclear spin wave function and the rovibronic wave function. The direct products of group G_{36} are tabulated in Tab. A.3. As mentioned above, the symmetry of the total wave function has to be A_2 or A_4 . Thus wave functions of A_1 symmetry can be combined with nuclear spin wave functions of symmetry A_2 and A_4 . Since there are 6 nuclear spin wave functions of symmetry A_4 and none of A_2 symmetry, the spin statistical weight for wave functions of A_1 symmetry is 6. E_1 can be combined with E_1 and E_2 . There are 3+1 nuclear spin wave functions of this symmetry, thus the spin statistical weight is 4. The spin statistical weights are given in brackets in Tab. 3.1 for all symmetries. In Fig. 3.2 the transition $J_{K_a K_c} = 14_{311} - 13_{410}$ is shown exemplarily whose torsional splitting is fully

Table 3.2: Symmetry of the nuclear spin wave functions of DME grouped by the total projection quantum number for the proton spins m_i .

m_i	Symmetry
3	A_1
2	$A_1 \oplus A_4 \oplus G$
1	$A_1 \oplus A_4 \oplus G$ $A_1 \oplus E_1 \oplus E_3 \oplus G$
0	$A_1 \oplus A_4$ $A_1 \oplus A_4 \oplus E_1 \oplus E_2 \oplus E_3 \oplus E_4 \oplus 2G$
-1	$A_1 \oplus A_4 \oplus G$ $A_1 \oplus E_1 \oplus E_3 \oplus G$
-2	$A_1 \oplus A_4 \oplus G$
-3	A_1
\rightarrow	$10 A_1 \oplus 6 A_4 \oplus 3 E_1 \oplus E_2 \oplus 3 E_3 \oplus E_4 \oplus 8G$

resolved. The line intensities reproduce nicely the derived spin statistical weight, which is denoted beneath the peaks. The consistency of the calculated spin statistical weight with the measured line intensities confirm the C_{2v} symmetry of dimethyl ether. This affirms especially the mirrored orientation of the methyl groups to each other. Rotation of one methyl group by an angle of 180° would destroy the C_{2v} symmetry.

3.6 Effective Rotational Hamiltonian

In this section an effective Hamiltonian for a molecule with two large amplitude motions in the rigid frame of a C_{2v} top is derived, following the approach of P. Groner, which is described in more detail in his work [12]. The approach is based on his earlier work dealing with molecules with large amplitude motions of a single internal rotor [19].

In the first step the Hamiltonian is separated into three parts containing the overall rotation H_R , the internal rotation H_I and the interaction terms of overall and internal rotation H_{RI} . In this first step the matrix elements are set up in the basis of symmetric rotor eigenfunctions combined with normalized free rotor functions in their exponential form. In the second step the solutions of H_I are derived starting from basis functions which are projections onto the ρ -axes of the internal rotors. The kinetic energy and the potential functions are expanded into Fourier series of free rotor functions. By the use of another Fourier expansion the eigenvalues and eigenfunctions of H_I can be calculated as a function of Fourier constants and so called localized functions and the K dependence can be calculated explicitly. In the final step all matrix elements are calculated in a new basis, which is a subset of all eigenfunctions of H_I . This basis only depends on the quantum numbers

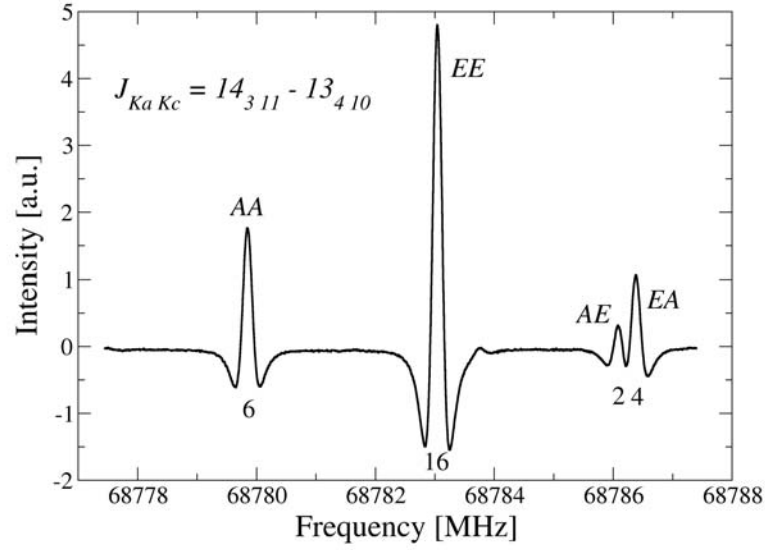


Figure 3.2: Experimental spectrum of the ground state transition $J_{K_a K_c} = 14_{311} - 13_{410}$. The tunneling splitting is fully resolved in this measurement. The spin statistical weight of each component is denoted beneath each peak.

J , K , M , ν , and the symmetry numbers σ_1 and σ_2 , which distinguish between the different substates. An effective Hamiltonian for DME is finally derived by calculating all symmetry adopted matrix elements.

3.6.1 Separation of the Hamiltonian

In an arbitrary molecule-fixed center-of-mass axis system the kinetic energy term T for overall rotation and internal motions has the form

$$T = \frac{1}{2} \begin{pmatrix} \tilde{\omega} & \tilde{\tau} \end{pmatrix} \begin{pmatrix} \mathbf{I}_\omega & \mathbf{I}_{\omega\tau} \\ \mathbf{I}_{\omega\tau} & \mathbf{I}_\tau \end{pmatrix} \begin{pmatrix} \omega \\ \tau \end{pmatrix} \quad (3.4)$$

where ω , τ are the column vectors of the components of the overall angular velocities, and the internal rotations, respectively. \mathbf{I}_ω , \mathbf{I}_τ , and $\mathbf{I}_{\omega\tau}$ are the moment of inertia tensors for the indicated motions. Expressed in terms of conjugate momenta, one obtains

$$T = \begin{pmatrix} \tilde{\mathbf{P}} & \tilde{\mathbf{p}} \end{pmatrix} \begin{pmatrix} \mathbf{A} + \rho \mathbf{F} \tilde{\rho} & -\rho \mathbf{F} \\ -\mathbf{F} \tilde{\rho} & \mathbf{F} \end{pmatrix} \begin{pmatrix} \mathbf{P} \\ \mathbf{p} \end{pmatrix} \quad (3.5)$$

with

$$\begin{aligned} \mathbf{A} &= (\hbar^2/8\pi^2) (\mathbf{I}_\omega)^{-1} \\ \rho &= (\mathbf{I}_\omega)^{-1} \mathbf{I}_{\omega\tau} \\ \mathbf{F} &= (\hbar^2/8\pi^2) (\mathbf{I}_\tau - \tilde{\rho} \mathbf{I}_\omega \rho)^{-1} \end{aligned} \quad (3.6)$$

\mathbf{A} , \mathbf{F} , ρ as well as \mathbf{I}_ω , $\mathbf{I}_{\omega\tau}$ and \mathbf{I}_τ are functions of the variables τ_1 and τ_2 . If ρ is replaced by

$$\rho = \rho^0 + \Delta\rho \quad (3.7)$$

where ρ^0 contains the constant terms and $\Delta\rho$ the variable dependent contributions, the Hamiltonian can be split into three parts as follows:

$$\begin{aligned} H &= T + V = H_R + H_I + H_{RI} \\ H_R &= \tilde{\mathbf{P}} \left(\mathbf{A} + \Delta\rho \mathbf{F} \Delta\tilde{\rho} + \Delta\rho \mathbf{F} \tilde{\rho}^0 + \rho^0 \mathbf{F} \Delta\tilde{\rho} \right) \mathbf{P} \\ H_I &= (\tilde{\mathbf{p}} - \tilde{\mathbf{P}}\rho^0) \mathbf{F} (\mathbf{p} - \tilde{\rho}^0 \mathbf{P}) + V \\ H_{RI} &= - [\tilde{\mathbf{P}} \Delta\rho \mathbf{F} \mathbf{p} + \tilde{\mathbf{p}} \mathbf{F} \Delta\tilde{\rho} \mathbf{P}] \end{aligned} \quad (3.8)$$

Basis Functions and Matrix Elements

The basis functions are set up as products of the symmetric rotor eigenfunctions, whose variables are the Eulerian angles of the molecule-fixed reference axis system and the internal basis functions for the internal rotors. The latter are normalized free rotor functions in exponential form. The symmetry numbers σ_1 and σ_2 are introduced. They are used to label the substates, because the off-diagonal matrix elements in these symmetry numbers vanish as shown in Sec. 3.4. The variable n_k labels the periodicity of the internal rotor k (in case of DME: $n_1 = n_2 = 3$).

$$|JKM j_1 \sigma_1 j_2 \sigma_2\rangle = |JKM\rangle |j_1 \sigma_1\rangle |j_2 \sigma_2\rangle \quad (3.9)$$

with

$$|j_k \sigma_k\rangle = (2\pi)^{\frac{1}{2}} e^{i(n_k j_k + \sigma_k) \tau_k} \quad (3.10)$$

The Rotational Hamiltonian H_R

The rotational Hamiltonian can be rewritten as

$$H_R = \sum_l R_l T_l \quad . \quad (3.11)$$

R_l is a symmetrized rotational operator of even order in the components of the overall angular momentum and T_l is a function of the internal variables τ_1 and τ_2 . The matrix elements in the above given basis are then:

$$\begin{aligned} \langle JK'M j'_1 \sigma'_1 j'_2 \sigma'_2 | H_R | JK M j_1 \sigma_1 j_2 \sigma_2 \rangle \\ = \sum_l \langle JK'M | R_l | JK M \rangle \langle j'_1 \sigma'_1 j'_2 \sigma'_2 | T_l | j_1 \sigma_1 j_2 \sigma_2 \rangle \end{aligned} \quad (3.12)$$

The Torsional Hamiltonian H_I

The matrix elements of H_I are more complicated, because they do not only contain the operators of the internal angular momentum \mathbf{p}_k , but also, in general, all components of the overall angular momentum operator \mathbf{P} :

$$H_I = \sum_{k=1}^2 \sum_{l=1}^2 (\mathbf{p}_k - \sum_{\alpha} \rho_{\alpha k} \mathbf{P}_{\alpha}) F^{(kl)} (\mathbf{p}_l - \sum_{\beta} \rho_{\beta l} \mathbf{P}_{\beta}) + V \quad (3.13)$$

As there are two internal rotors, whose axis of internal rotation generally do not coincide, it is not possible to find an orthonormal axis system which has two axes oriented along the internal axes of rotation. In case of a single internal rotor, such axis systems which are oriented along the internal axis (IAS = internal axis system) or along the ρ -axis (RAS = Rho axis system) are preferably chosen, because they simplify the Hamiltonian considerably. Many approaches can be found in the literature, which therefore separate H_I into three different terms containing either the pure contributions from \mathbf{p}_k or \mathbf{P} , or contributions from both \mathbf{p}_k and \mathbf{P} . Nevertheless alternate forms of the basis functions can be defined, which allow to express each internal rotation in its RAS by projecting the basis functions defined in the principal axis system onto the axes of internal rotation:

$$|JKM j_1 \sigma_1 j_2 \sigma_2\rangle = \sum_{K_k} |JK_k M\rangle \langle JK_k M | JKM\rangle |j_1 \sigma_1 j_2 \sigma_2\rangle \quad (3.14)$$

The functions $|JK_k M\rangle$ and their variables refer to an axis system whose z_k is parallel to the vector $\rho_k^0 = (\rho_{xk} \rho_{yk} \rho_{zk})$ of the k th internal rotor. In this axis systems the operator

$$\mathbf{p}_k - \sum_{\alpha} \rho_{\alpha k} \mathbf{P}_{\alpha} \quad (3.15)$$

transforms to

$$\mathbf{p}_k - \rho_k \mathbf{P}_{z_k} \quad (3.16)$$

with $\rho_k = (\rho_{xk}^2 + \rho_{yk}^2 + \rho_{zk}^2)$ and H_I can be written as

$$\begin{aligned} & \langle JK' M j'_1 \sigma'_1 j'_2 \sigma'_2 | H_I | JK M j_1 \sigma_1 j_2 \sigma_2 \rangle \\ &= \sum_{K_1} \sum_{K_2} Y_{K'K}(K_1, K_2) \times \langle j'_1 \sigma'_1 j'_2 \sigma'_2 | H_I(K_1, K_2) | j_1 \sigma_1 j_2 \sigma_2 \rangle \end{aligned} \quad (3.17)$$

with

$$H_I(K_1, K_2) = \sum_{k=1}^2 \sum_{l=1}^2 (\mathbf{p}_k - \rho_k \mathbf{P}_{z_k}) F^{(kl)} (\mathbf{p}_l - \rho_l \mathbf{P}_{z_l}) + V \quad (3.18)$$

$$\begin{aligned} Y_{K'K}(K_1, K_2) &= \frac{1}{2} [\langle JK' M | JK_1 M \rangle \langle JK_1 M | JK_2 M \rangle \langle JK_2 M | JKM \rangle \\ &+ \langle JK' M | JK_2 M \rangle \langle JK_2 M | JK_1 M \rangle \langle JK_1 M | JKM \rangle] \end{aligned} \quad (3.19)$$

The transformation coefficients $\langle JK_k M | JKM \rangle$ depend only on the direction cosines of the vector ρ_k^0 with respect to the molecule fixed axis system. Thus, $Y_{K'K}(K_1, K_2)$ depends only on the polar angles β_k and the azimuthal angles α_k of the vectors ρ_k with respect to the reference axes. In the case of DME $\beta_2 = \pi - \beta_1$ and $\alpha_k = 0$ due to symmetry constraints. As the projection terms $Y_{K'K}(K_1, K_2)$ can be calculated explicitly, the problem simplifies to finding the eigenvalues and eigenfunctions of $H_I(K_1, K_2)$, which will be derived in the following subsection.

3.6.2 Solutions of $H_I(K_1, K_2)$

Obviously the potential $V(\tau_1, \tau_2)$ and the functions $F^{(kl)}(\tau_1, \tau_2)$ are periodic functions in the torsional angles τ_1 and τ_2 . Thus they can be expanded into Fourier series

$$F^{(kl)}(\tau_1, \tau_2) = \sum_{j_1} \sum_{j_2} F_{j_1 j_2}^{(kl)} e^{in_1 j_1 \tau_1} e^{in_2 j_2 \tau_2} \quad (3.20)$$

$$V(\tau_1, \tau_2) = \sum_{j_1} \sum_{j_2} V_{j_1 j_2} e^{in_1 j_1 \tau_1} e^{in_2 j_2 \tau_2} \quad (3.21)$$

In order to compare the approach suggested by P. Groner to other commonly applied approaches a short insertion follows at this point. By calculating the Fourier terms explicitly up to the first order terms using the identities $V_{10} = V_{01} = V_{-10} = V_{0-1}$, $V_{11} = V_{-1-1}$, and $V_{-11} = V_{1-1}$, which are valid for molecules with C_{2v} symmetry and two equivalent internal rotors, $V(\tau_1, \tau_2)$ can be rewritten in the form:

$$\begin{aligned} V(\tau_1, \tau_2) &= \sum_{j_1} \sum_{j_2} V_{j_1 j_2} e^{in_1 j_1 \tau_1} e^{in_2 j_2 \tau_2} \\ &= V_{00} + 2V_{10}(\cos(n_1 \tau_1) + \cos(n_2 \tau_2)) \\ &\quad + 2V_{11}(\cos(n_1 \tau_1) \cos(n_2 \tau_2) - \sin(n_1 \tau_1) \sin(n_2 \tau_2)) \\ &\quad + 2V_{1-1}(\cos(n_1 \tau_1) \cos(n_2 \tau_2) + \sin(n_1 \tau_1) \sin(n_2 \tau_2)) + \dots \end{aligned} \quad (3.22)$$

Using the common definitions $V_0 = V_{00} + 4V_{10}$, $V_3 = -4V_{10}$, $V_{33} = 2(V_{11} + V_{1-1})$ and $V'_{33} = 2(V_{1-1} - V_{11})$, one obtains

$$\begin{aligned} V(\tau_1, \tau_2) &= V_0 \\ &\quad + \frac{V_3}{2}(2 - \cos(n_1 \tau_1) - \cos(n_2 \tau_2)) \\ &\quad + V_{33} \cos(n_1 \tau_1) \cos(n_2 \tau_2) \\ &\quad + V'_{33} \sin(n_1 \tau_1) \sin(n_2 \tau_2) + \dots \end{aligned} \quad (3.23)$$

V_3 is the hindering potential whereas V_{33} and V'_{33} are top-top coupling parameters. Neglecting all but the zeroth order contribution of $F^{(kl)}$ one obtains by

defining $F = F_{11} = F_{22}$ and $F' = F_{12} = F_{21}$, which holds for equivalent internal rotors:

$$\begin{aligned}
H_I(K_1, K_2) &= F((\mathbf{p}_1 - \rho_1 K_1)^2 + (\mathbf{p}_2 - \rho_2 K_2)^2) & (3.24) \\
&+ F'((\mathbf{p}_1 - \rho_1 K_1)(\mathbf{p}_2 - \rho_2 K_2) + (\mathbf{p}_2 - \rho_2 K_2)(\mathbf{p}_1 - \rho_1 K_1)) \\
&+ V_0 + \frac{V_3}{2} (2 - \cos(n_1 \tau_1) - \cos(n_2 \tau_2)) \\
&+ V_{33} \cos(n_1 \tau_1) \cos(n_2 \tau_2) \\
&+ V'_{33} \sin(n_1 \tau_1) \sin(n_2 \tau_2) + \dots
\end{aligned}$$

It should be mentioned that in most approaches the matrix elements of the torsional Hamiltonian are not calculated in the internal axis system. Thus the projection terms $Y_{K'K}(K_1, K_2)$ which are separated in P. Groners approach, do not occur, but direction cosines as well as all components of the overall angular momentum have to be considered in the matrix elements of H_I . Often the contributions due to H_{RI} are small and are treated by perturbation theory or are simply negligible. If the small contributions from the internal rotation to H_R are neglected all matrix elements of the total Hamiltonian are already obtained at this stage and the eigenvalues can be obtained by diagonalization. Nevertheless accurate fitting of experimental data is hampered by the extremely large computational time required to adjust all parameters in this Hamiltonian accurately. In the literature a variety of approaches is found to overcome this problem. Usually assumptions or calculated values were used to fix some of the parameters. P. Groners approach makes use of the periodicity of the eigenvalues and eigenfunctions of H_I in σ_1 and σ_2 . Both can be expressed in terms of so-called localized functions by applying another Fourier expansion, which rapidly converges if the barrier to torsion is moderately high. Following this approach one obtains the eigenvalues and eigenfunctions of $H_I(K_1, K_2)$ explicitly as a function of a small set of constants and constant functions which are in particular independent of K_k and σ_k , which drastically reduces computational time, because $H_I(K_1, K_2)$ is directly obtained in diagonalized form. In the following a more detailed description is given, of how these functions are derived.

As can be seen in Eq. 3.20 the basis of the Fourier expansion coincides with the basis of the free rotor functions $|j_1 \sigma_1 j_2 \sigma_2\rangle$, which makes it suitable to choose them as a basis of $H_I(K_1, K_2)$, because all Fourier terms but one vanish in the matrix of the Hamiltonian:

$$\begin{aligned}
&\langle j'_1 \sigma_1 j'_2 \sigma_2 | H_I(K_1, K_2) | j_1 \sigma_1 j_2 \sigma_2 \rangle \\
&= \sum_{k=1}^2 \sum_{l=1}^2 (n_k j'_k + \sigma_k - \rho_k K_k) F_{j'_1 - j_1, j'_2 - j_2}^{(kl)} (n_l j_l + \sigma_l - \rho_l K_l) + V_{j'_1 - j_1, j'_2 - j_2} \quad (3.25)
\end{aligned}$$

The eigenfunctions of the Hamiltonian expressed in this basis are given by

$$|v \sigma_1(K_1) \sigma_2(K_2)\rangle = \Phi_{v \sigma_1 \sigma_2}^{(K_1, K_2)}(\tau_1, \tau_2) = \sum_{j_1} \sum_{j_2} U_{j_1 j_2 v \sigma_1 \sigma_2}^{(K_1, K_2)} |j_1 \sigma_1 j_2 \sigma_2\rangle \quad (3.26)$$

As all matrix elements involving unequal σ_1 's or σ_2 's vanish, the following equation holds for any choice of j'_1, j'_2, K_1 and K_2 .

$$\begin{aligned} & \sum_{j_1} \sum_{j_2} \langle j'_1 \sigma_1 j'_2 \sigma_2 | H_I(K_1, K_2) | j_1 \sigma_1 j_2 \sigma_2 \rangle U_{j_1 j_2 \nu \sigma_1 \sigma_2}^{(K_1, K_2)} \quad (3.27) \\ &= \sum_{j_1} \sum_{j_2} \langle j'_1 \sigma_1 j'_2 \sigma_2 | j_1 \sigma_1 j_2 \sigma_2 \rangle U_{j_1 j_2 \nu \sigma_1 \sigma_2}^{(K_1, K_2)} E_{\nu \sigma_1 \sigma_2}^{(K_1, K_2)} \\ &= U_{j'_1 j'_2 \nu \sigma_1 \sigma_2}^{(K_1, K_2)} E_{\nu \sigma_1 \sigma_2}^{(K_1, K_2)} \end{aligned}$$

Now it appears that $E_{\nu \sigma_1 \sigma_2}^{(K_1, K_2)}$ and $\Phi_{\nu \sigma_1 \sigma_2}^{(K_1, K_2)}(\tau_1, \tau_2)$ are periodic functions in σ_1 and σ_2 with periodicity n_1, n_2 . This can be proven by substituting j'_k by $j'_k - \lambda_k$, j_k by $j_k - \lambda_k$, and σ_k by $\sigma_k + \lambda_k n_k$ in Eq. 3.27 and subsequently inserting Eq. 3.25. The values of λ_k ($k = 1, 2$) can be any arbitrary integers. Thus the eigenfunctions and eigenvalues can be expanded into Fourier series in σ_1 and σ_2 .

$$E_{\nu \sigma_1 \sigma_2}^{(K_1, K_2)} = \sum_{q_1=0}^{N_1-1} \sum_{q_2=0}^{N_2-1} e^{i2\pi(q_1 \sigma_1/n_1 + q_2 \sigma_2/n_2)} \epsilon_{\nu q_1 q_2}^{(K_1, K_2)}, \quad (3.28)$$

$$\begin{aligned} \Phi_{\nu \sigma_1 \sigma_2}^{(K_1, K_2)}(\tau_1, \tau_2) &= \phi_{\sigma_1, \sigma_2}(N_1 N_2)^{-\frac{1}{2}} \quad (3.29) \\ &\times \sum_{q_1=0}^{N_1-1} \sum_{q_2=0}^{N_2-1} e^{i2\pi(q_1 \sigma_1/n_1 + q_2 \sigma_2/n_2)} \theta_{\nu q_1 q_2}^{(K_1, K_2)}(\tau_1, \tau_2) \end{aligned}$$

$\phi_{\sigma_1, \sigma_2}(N_1 N_2)^{-\frac{1}{2}}$ is a complex phase factor of magnitude 1. At this point it is important to note, that the expansion can be terminated after $N_k = n - 1$ summations, if σ_k is an arbitrary integer, because the complex e -function has a 2π periodicity.

Several important properties can be derived by inserting Eq. 3.25 into Eq. 3.27, of which only the most essential are carried out in the following. If σ_k is substituted by $\sigma_k - \rho_k K_k$ ($k = 1, 2$) and K_1 as well as K_2 is set to zero one essential set of relations is obtained, which allow to explicitly derive the K dependence of the eigenvalues and eigenfunctions:

$$E_{\nu \sigma_1 \sigma_2}^{(K_1, K_2)} = E_{\nu \sigma_1 - \rho_1 K_1, \sigma_2 - \rho_2 K_2}^{(0,0)} \quad (3.30)$$

$$U_{j_1 j_2 \nu \sigma_1 \sigma_2}^{(K_1, K_2)} = U_{j_1 j_2 \nu \sigma_1 - \rho_1 K_1, \sigma_2 - \rho_2 K_2}^{(0,0)} \quad (3.31)$$

$$\Phi_{\nu \sigma_1 \sigma_2}^{(K_1, K_2)}(\tau_1, \tau_2) = \Phi_{\nu \sigma_1 - \rho_1 K_1, \sigma_2 - \rho_2 K_2}^{(0,0)}(\tau_1, \tau_2) e^{i(\rho_1 K_1 \tau_1 + \rho_2 K_2 \tau_2)} \quad (3.32)$$

$$\theta_{\nu q_1 q_2}^{(K_1, K_2)}(\tau_1, \tau_2) = \theta_{\nu q_1 q_2}^{(0,0)}(\tau_1, \tau_2) e^{i(\rho_1 K_1 (\tau_1 - 2\pi q_1/n_1) + \rho_2 K_2 (\tau_2 - 2\pi q_2/n_2))} \quad (3.33)$$

In order to take advantage of the Fourier expansions 3.28 the summation index N_k has to be expanded to $N_k = m_k n_k$, because σ_k may not longer be an integer due to the substitution. The expansion factor m_k for the domain τ_k has to be chosen in a manner that $m_k \rho_k$ is an integer as well as m_k itself.

Using the relation

$$|j_1 \sigma_1 j_2 \sigma_2\rangle = (2\pi)^{-1} e^{i(n_1 j_1 + \sigma_1)\tau_1} e^{i(n_2 j_2 + \sigma_2)\tau_2} \quad (3.34)$$

$$= (2\pi)^{-1} e^{i(n_1 j_1 + \sigma_1)(\tau_1 + 2\pi\lambda/n_1)} e^{i(n_2 j_2 + \sigma_2)(\tau_2 + 2\pi\lambda/n_2)} \quad (3.35)$$

$$\times e^{-i2\pi(\sigma_1\lambda_1/n_1 + \sigma_2\lambda_2/n_2)}$$

with arbitrary integers λ_1 and λ_2 results in

$$\Phi_{\nu\sigma_1\sigma_2}^{(K_1, K_2)}(\tau_1, \tau_2) = \Phi_{\nu\sigma_1\sigma_2}^{(K_1, K_2)}(\tau_1 + 2\pi\lambda_1/n_1, \tau_2 + 2\pi\lambda_2/n_2) \quad (3.36)$$

$$\times e^{-i2\pi(\sigma_1\lambda_1/n_1 + \sigma_2\lambda_2/n_2)}$$

$$\theta_{\nu q_1 q_2}^{(K_1, K_2)}(\tau_1, \tau_2) = \theta_{\nu, q_1 + \lambda_1, q_2 + \lambda_2}^{(K_1, K_2)}(\tau_1 + 2\pi\lambda_1/n_1, \tau_2 + 2\pi\lambda_2/n_2) \quad (3.37)$$

Finally the following equations are obtained

$$E_{\nu\sigma_1\sigma_2}^{(K_1, K_2)} = \sum_{q_1=0}^{N_1-1} \sum_{q_2=0}^{N_2-1} e^{i2\pi(q_1(\sigma_1 - \rho_1 K_1)/n_1 + q_2(\sigma_2 - \rho_2 K_2)/n_2)} \varepsilon_{\nu q_1 q_2} \quad (3.38)$$

$$\theta_{\nu q_1 q_2}^{(K_1, K_2)}(\tau_1, \tau_2) = \theta_{\nu 0 0}^{(0,0)}(\tau_1 - 2\pi q_1/n_1, \tau_2 - 2\pi q_2/n_2) \quad (3.39)$$

$$\times e^{i(\rho_1 K_1(\tau_1 - 2\pi q_1/n_1) + \rho_2 K_2(\tau_2 - 2\pi q_2/n_2))}$$

It is important to note that by this presented approach, expressions for $E_{\nu\sigma_1\sigma_2}^{(K_1, K_2)}$, $\theta_{\nu q_1 q_2}^{(K_1, K_2)}(\tau_1, \tau_2)$ and $\Phi_{\nu q_1 q_2}^{(K_1, K_2)}(\tau_1, \tau_2)$ have been derived using Fourier coefficients which are independent of K_1 , K_2 . Only these small set of Fourier constants $\varepsilon_{\nu q_1 q_2}$ and localized functions $\theta_{\nu 0 0}^{(0,0)}(\tau_1, \tau_2)$ is required to explicitly give the eigenfunctions $\Phi_{\nu\sigma_1\sigma_2}^{(K_1, K_2)}(\tau_1, \tau_2)$ and eigenvalues $E_{\nu\sigma_1\sigma_2}^{(K_1, K_2)}$ of the Hamiltonian $H_I(K_1, K_2)$.

Properties which are not derived here in detail are the 2π periodicity of $\Phi_{\nu q_1 q_2}^{(K_1, K_2)}(\tau_1, \tau_2)$ in τ_1 and τ_2 and the periodicity of $\theta_{\nu q_1 q_2}^{(K_1, K_2)}(\tau_1, \tau_2)$ in $2\pi m_k$ in τ_1 and τ_2 , as well as the orthogonality of both basis sets θ and Φ .

3.6.3 Basis Transformation

Now all eigenfunctions $|\nu\sigma_1(K_1)\sigma_2(K_2)\rangle$ of $H_I(K_1, K_2)$ can be calculated, but due to the dependency on K_1 and K_2 they would provide inappropriate basis functions for the total Hamiltonian. Therefore all matrix elements are transformed to a new basis defined as

$$|JKM\nu\sigma_1\sigma_2\rangle = |JKM\rangle |\nu\sigma_1(K)\sigma_2(sK)\rangle \quad (3.40)$$

where $s = +1$ or $s = -1$ depending on whether the product $\rho_{z_1}\rho_{z_2}$ is positive or negative (for DME $s = -1$). The functions $|\nu\sigma_1(K)\sigma_2(sK)\rangle$ are only solutions of $H_I(K, sK)$ and thus only a subset of all solutions of $H_I(K_1, K_2)$.

In this basis set all matrix elements are now calculated. For the rotational Hamiltonian H_R the matrix elements are then given by

$$\langle JK'M\nu'\sigma_1\sigma_2 | H_R | JKM\nu\sigma_1\sigma_2 \rangle =$$

$$\sum_l \langle JK'M | R_l | JKM \rangle \times \langle \nu'\sigma_1(K')\sigma_2(sK') | T_l | \nu\sigma_1(K)\sigma_2(sK) \rangle \quad (3.41)$$

The matrix elements of H_I have to be expanded using appropriate projection operators:

$$\begin{aligned}
& \langle \mathbf{v}' \sigma_1(K') \sigma_2(sK') | H_I(K_1, K_2) | \mathbf{v} \sigma_1(K) \sigma_2(sK) \rangle \\
&= \sum_{\mathbf{v}'''} \sum_{\mathbf{v}''} \langle \mathbf{v}' \sigma_1(K') \sigma_2(sK') | \mathbf{v}''' \sigma_1(K_1'') \sigma_2(K_2'') \rangle \\
&\quad \times \langle \mathbf{v}''' \sigma_1(K_1'') \sigma_2(K_2'') | H_I(K_1, K_2) | \mathbf{v}'' \sigma_1(K_1') \sigma_2(K_2') \rangle \\
&\quad \times \langle \mathbf{v}'' \sigma_1(K_1') \sigma_2(K_2') | \mathbf{v} \sigma_1(K) \sigma_2(sK) \rangle
\end{aligned} \tag{3.42}$$

As K_1' , K_1'' , K_2' , and K_2'' are just arbitrary but fixed constants, they can be chosen as $K_1'' = K_1' = K_1$ and $K_2'' = K_2' = K_2$. The matrix elements of H_I reduce subsequently as follows:

$$\begin{aligned}
& \langle JK'M \mathbf{v}' \sigma_1 \sigma_2 | H_I | JKM \mathbf{v} \sigma_1 \sigma_2 \rangle \\
&= \sum_{K_1} \sum_{K_2} Y_{K'K}(K_1, K_2) \times \langle \mathbf{v}' \sigma_1(K') \sigma_2(sK') | H_I(K_1, K_2) | \mathbf{v} \sigma_1(K) \sigma_2(sK) \rangle \\
&= \sum_{K_1} \sum_{K_2} Y_{K'K}(K_1, K_2) \sum_{\mathbf{v}''} \langle \mathbf{v}' \sigma_1(K') \sigma_2(sK') | \mathbf{v}'' \sigma_1(K_1) \sigma_2(K_2) \rangle \\
&\quad \times E_{\mathbf{v}'' \sigma_1 \sigma_2}(K_1, K_2) \langle \mathbf{v}'' \sigma_1(K_1) \sigma_2(K_2) | \mathbf{v} \sigma_1(K) \sigma_2(sK) \rangle
\end{aligned} \tag{3.43}$$

3.6.4 Calculation of the Matrix Elements

Now all matrix elements can be calculated in the basis $|\mathbf{v} \sigma_1(K_1) \sigma_2(K_2)\rangle$ expressed as integrals involving the localized functions $\theta_{\mathbf{v}q_1q_2}^{(K_1, K_2)}(\tau_1, \tau_2)$, which have been derived in Sec. 3.6.2.

The Rotational Hamiltonian H_R

Matrix elements whose operator has the form $t(\tau_1, \tau_2)$ and does not contain the differential operators p_1 or p_2 become

$$\begin{aligned}
& \langle \mathbf{v}' \sigma_1(K_1') \sigma_2(K_2') | t(\tau_1, \tau_2) | \mathbf{v} \sigma_1(K_1) \sigma_2(K_2) \rangle = \\
& \sum_{q_1=0}^{N_1-1} \sum_{q_2=0}^{N_2-1} e^{i\pi(q_1(2\sigma_1-\rho_1(K_1+K_1'))/n_1+q_2(2\sigma_2-\rho_2(K_2+K_2'))/n_2)} T_{\mathbf{v}'\mathbf{v}q_1q_2}^{(K_1-K_1', K_2-K_2')}
\end{aligned}$$

with the integrals

$$\begin{aligned}
T_{\mathbf{v}'\mathbf{v}q_1q_2}^{K_1, K_2} &= e^{-i\pi(q_1\rho_1\kappa_1/n_1+q_2\rho_2\kappa_2/n_2)} (m_1 m_2)^{-1} \\
& \int_{-m_1\pi}^{m_1\pi} \int_{-m_2\pi}^{m_2\pi} e^{i(\rho_1\kappa_1\tau_1+\rho_2\kappa_2\tau_2)} \theta_{\mathbf{v}'00}(\tau_1, \tau_2) t(\tau_1, \tau_2) \theta_{\mathbf{v}q_1q_2}(\tau_1, \tau_2) d\tau_1 d\tau_2
\end{aligned}$$

which are called tunneling parameters because they involve integrals between localized functions centered in different potential wells. κ is defined by $\kappa = K - K'$.

Thus the matrix elements of H_R become

$$\begin{aligned}
& \langle JK'Mv'\sigma_1\sigma_2 | H_R | JKMv\sigma_1\sigma_2 \rangle \\
&= \sum_l \langle JK'M | R_l | JKM \rangle \\
&\quad \times \sum_{q_1=0}^{N_1-1} \sum_{q_2=0}^{N_2-1} e^{i\pi(q_1(2\sigma_1-\rho_1(K+K'))/n_1+q_2(2\sigma_2-s\rho_2(K+K'))/n_2)} T_l^{(\kappa,s\kappa)}{}_{v'vq_1q_2}
\end{aligned} \tag{3.44}$$

The Torsional Hamiltonian H_I

The equivalent to the tunneling parameters

$T_{v'vq_1q_2}^{(\kappa,s\kappa)}$ calculated for $t(\tau_1, \tau_2) = 1$ are defined as $I_{v'vq_1q_2}^{(\kappa,s\kappa)}$ with

$$I_{v'vq_1q_2}^{(\kappa,s\kappa)} = e^{i\pi(q_1\rho_1\kappa_1/n_1+q_2\rho_2\kappa_2/n_2)} I_{v'vq_1q_2}^{(\kappa,s\kappa)} \tag{3.45}$$

the integrals in the matrix elements of H_I can be calculated. Using the approximation for nonzero κ_1, κ_2

$$I_{v'vq_1q_2}^{(\kappa,s\kappa)} \approx \delta_{v'v} \delta_{0q_1} \delta_{0q_2} \tag{3.46}$$

the matrix elements of H_I can be derived as

$$\begin{aligned}
& \langle JK'Mv'\sigma_1\sigma_2 | H_I | JKMv\sigma_1\sigma_2 \rangle \\
&\approx \delta_{v'v} \sum_{K_1} \sum_{K_2} Y_{K'K}(K_1, K_2) \sum_{q_1=0}^{N_1-1} \sum_{q_2=0}^{N_2-1} e^{i2\pi(q_1(\sigma_1-\rho_1K_1)/n_1+q_2(\sigma_2-\rho_2K_2)/n_2)} \epsilon_{vq_1q_2}
\end{aligned} \tag{3.47}$$

The Torsion-Rotational Hamiltonian H_{RI}

The matrix elements for H_{RI} are finally obtained by rewriting

$$H_{RI} = - \sum_{\alpha} \mathbf{P}_{\alpha} \sum_k [t_{\alpha k}(\tau_1, \tau_2) \mathbf{p}_k + \mathbf{p}_k t_{\alpha k}(\tau_1, \tau_2)] = - \sum_{\alpha} \mathbf{P}_{\alpha} T_{\alpha} \tag{3.48}$$

A similar treatment to the one described above leads to

$$\begin{aligned}
& \langle JK'Mv'\sigma_1\sigma_2 | H_{RI} | JKMv\sigma_1\sigma_2 \rangle \\
&= \sum_{q_1=0}^{N_1-1} \sum_{q_2=0}^{N_2-1} e^{i\pi(q_1(2\sigma_1-\rho_1(K+K'))/n_1+q_2(2\sigma_2-s\rho_2(K+K'))/n_2)} \\
&\quad \times \sum_{\alpha} \left[- \langle JK'M | \mathbf{P}_{\alpha} | JKM \rangle \bar{T}_{\alpha}^{(\kappa,s\kappa)}{}_{v'vq_1q_2} \right. \\
&\quad \left. + \langle JK'M | \mathbf{P}_z \mathbf{P}_{\alpha} + \mathbf{P}_{\alpha} \mathbf{P}_z | JKM \rangle T_{\alpha}^{(\kappa,s\kappa)}{}_{v'vq_1q_2} \right]
\end{aligned} \tag{3.49}$$

$T_{\alpha}^{(\kappa_1, \kappa_2)}_{\mathbf{v}'\mathbf{v}q_1q_2}$ can be derived by substituting $t(\tau_1, \tau_2)$ by

$\sum_k (\delta_{k1} + s\delta_{k2}) \rho_k t_{\alpha k}(\tau_1, \tau_2)$ and $\bar{T}_{\alpha}^{(\kappa_1, \kappa_2)}_{\mathbf{v}'\mathbf{v}q_1q_2}$ is

$$\begin{aligned} T_{\alpha}^{(\kappa_1, \kappa_2)}_{\mathbf{v}'\mathbf{v}q_1q_2} &= e^{-i\rho(q_1\rho_1\kappa_1/n_1+q_2\rho_2\kappa_2/n_2)} (m_1m_2)^{-1} \quad (3.50) \\ &\int_{-m_1\pi}^{m_1\pi} \int_{-m_2\pi}^{m_2\pi} e^{i(\rho_1\kappa_1\tau_1+\rho_2\kappa_2\tau_2)} \sum_k t_{\alpha k}(\tau_1, \tau_2) \\ &\times \left[(p_k \theta_{\mathbf{v}'00}(\tau_1, \tau_2)) \theta_{\mathbf{v}q_1q_2}(\tau_1, \tau_2) \right. \\ &\left. - \theta_{\mathbf{v}'00}(\tau_1, \tau_2) (p_k \theta_{\mathbf{v}q_1q_2}(\tau_1, \tau_2)) \right] d\tau_1 d\tau_2 \end{aligned}$$

Only the first part of Eq. 3.49 contributes something new, which are matrix elements involving a rotational operator of order one combined with tunneling parameters.

The Total Hamiltonian H

The matrix elements of the complete Hamiltonian are thus

$$\begin{aligned} &\langle JK'M\mathbf{v}'\sigma_1\sigma_2 | H | JKM\mathbf{v}\sigma_1\sigma_2 \rangle \\ &= \sum_l \langle JK'M | R_l | JKM \rangle \quad (3.51) \\ &\sum_{q_1=0}^{N_1-1} \sum_{q_2=0}^{N_2-1} e^{i\pi(q_1(2\sigma_1-\rho_1(K+K'))/n_1+q_2(2\sigma_2-s\rho_2(K+K'))/n_2)} T_l^{(\kappa, s\kappa)}_{\mathbf{v}'\mathbf{v}q_1q_2} \\ &+ \delta_{\mathbf{v}'\mathbf{v}} \sum_{K_1} \sum_{K_2} Y_{K'K}(K_1, K_2) \sum_{q_1=0}^{N_1-1} \sum_{q_2=0}^{N_2-1} e^{i2\pi(q_1(\sigma_1-\rho_1K_1)/n_1+q_2(\sigma_2-\rho_2K_2)/n_2)} \epsilon_{\mathbf{v}q_1q_2} \end{aligned}$$

3.6.5 Effective Hamiltonian for Dimethyl Ether

An effective Hamiltonian can be derived for a specific state characterized by a set of vibrational or internal motion labels \mathbf{v} by assuming that all terms in Eq. 3.51 with $\mathbf{v} \neq \mathbf{v}'$ are negligible. If the exponential functions are replaced by cosine- and sine-functions and the Fourier double sums are rewritten changing the lower and upper limit of q_k to $-L_k$ and L_k , respectively. $L_k = (N_k - 1)/2$ for odd values of N_k whereas $L_k = N_k/2 - 1$ for even values. Although $q_k = N_k/2$ should also be included in the latter case, it is neglected because usually N_k is large and the Fourier series are expected to converge rapidly, which is supported by the analysis given in the experimental section. Finally, the symmetry properties of the operators obtained for molecules with G_{36} -symmetry, are taken into account. The matrix elements of the Hamiltonian can now be expressed as

$$\begin{aligned} &\langle JK'M\mathbf{v}\sigma_1\sigma_2 | H | JKM\mathbf{v}\sigma_1\sigma_2 \rangle \\ &= \sum_{K_1} \sum_{K_2} Y_{K'K}(K_1, K_2) \Sigma_0 + \sum_l \langle JKM | R_l | JKM \rangle \Sigma_l \quad (3.52) \end{aligned}$$

with the transformed prefactors Σ_0 and Σ_l

$$\Sigma_0 = \varepsilon_{00} + 2 \sum_{q>0} \left[C'_{qq} \varepsilon_{qq} + C'_{q-q} \varepsilon_{q-q} \sum_{q'=-q+1}^{q-1} (C'_{qq'} + C'_{q'q}) \varepsilon_{qq'} \right] \quad (3.53)$$

and

$$\Sigma_l = T_l^{(\kappa)}{}_{00} + 2 \sum_{q>0} \left[C_{qq} T_l^{(\kappa)}{}_{qq} + C_{q-q} T_l^{(\kappa)}{}_{q-q} \right. \\ \left. \times \sum_{q'=-q+1}^{q-1} (C_{qq'} + C_{q'q}) T_l^{(\kappa)}{}_{qq'} \right] \quad (3.54)$$

$C_{qq'}$ and $C'_{qq'}$ are cosine-functions defined as

$$C'_{qq'} = \cos(2\pi (q(\sigma_1 - \rho K_1) + q'(\sigma_2 - \rho K_2)) / n) \\ C_{qq'} = \cos(\pi (q(2\sigma_1 - \rho(K + K')) + q'(2\sigma_2 + \rho(K + K')))) / n) \quad (3.55)$$

A more detailed description is given in [12], in which a more general form is derived. For simplicity the subscripts $\mathbf{v}\mathbf{v}'$ and \mathbf{v} are omitted, $(\kappa, s\kappa)$ is replaced by κ and the summation indices q_1, q_2 by q, q' . The coefficients $\varepsilon_{qq'}$ and $T_l^{(\kappa)}{}_{qq'}$ in these series are actually the matrix elements of the torsional energy and of functions depending on both coordinates of internal rotation, respectively, in a basis of localized functions which can be obtained from the eigenfunctions of the torsional Hamiltonian. These coefficients are the spectroscopic parameters together with the internal rotation parameter ρ and the polar angle β . Fourier coefficients with $q = q' = 0$ are equivalent to the rigid-rotor rotational parameters and only Fourier coefficients with $q > 0$ or $q' > 0$, so-called tunneling parameters, arise from the interaction between internal and overall rotation. As has been shown before for the vibrational ground state of DME, the first order tunneling term of each series ($q = 1, q' = 0$) is usually sufficient for a quick convergence of the fit.

Results of this model approach will be discussed in Sec. 4.2. To illustrate the effect of the tunneling on the energy diagram and the corresponding transition frequencies, one example is given in Figs. 3.3 and 3.4. Fig. 3.3 shows the splitting of energy levels with quantum numbers $K_a = 6$ (left) and $K_a = 5$ (right), and $K_c = J - K_a + 1$ in the vibrational ground state of DME. In Fig. 3.4 Q -branch frequencies connecting lower states described in Fig. 3.3 (right panel) and upper states (left panel) are plotted together with experimentally determined values. This favorable comparison is a result of a rather limited set of tunneling parameters, which will be discussed in detail in the analysis section (Sec. 4.2).

3.6.6 Discussion of the Hamiltonian

Potential

In the following the effect of the potential and the kinetic terms on the solutions and eigenvalues of the internal Hamiltonian will be discussed. The

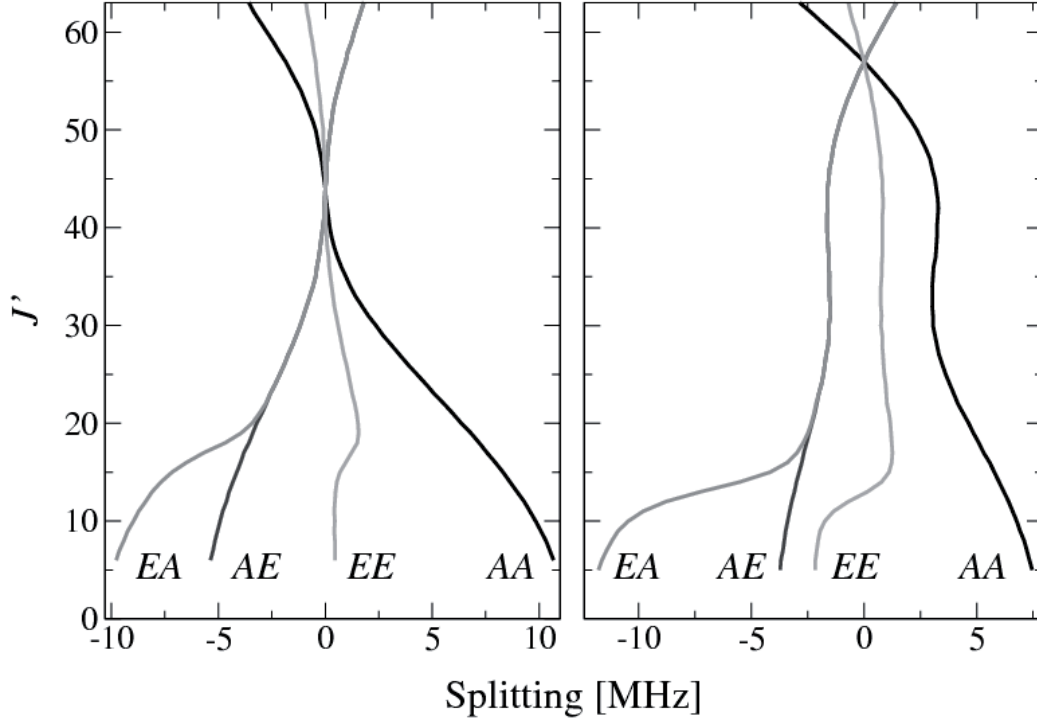


Figure 3.3: Torsional splitting of energy levels with $K_c = J - K_a + 1$ in the vibrational ground state of DME. Levels having quantum numbers $K_a = 6$ are shown on the left, whereas levels with $K_a = 5$ are shown on the right. The energy has been calculated neglecting all tunneling parameters. The splitting depicted in this figure is obtained by subtracting this value from the energy derived if all fitted parameters are included.

considerations are focused on the most significant Fourier terms and contributions from Fourier constants other than F , F' , and V_3 are neglected. As the barrier to torsion V_3 is relatively high in the DME molecule, the closer inspection of the two limiting cases of free rotation ($V_3 = 0$) and the high barrier limit ($V_3 \rightarrow \infty$) gives valuable insights on the character of the solutions and the eigenvalues of internal rotation.

In the free rotor limit ($V_3 = 0$), the Hamiltonian $H_I(0,0)$ reduces to

$$H_I(0,0) = F(\mathbf{p}_1^2 + \mathbf{p}_2^2) + F'(\mathbf{p}_1\mathbf{p}_2 + \mathbf{p}_2\mathbf{p}_1) \quad (3.56)$$

and the matrix in the free rotor basis

$$\Phi_{m_1, m_2}(\tau_1, \tau_2) = e^{im_1\tau_1} e^{im_2\tau_2} \quad (m_k = 3j_k + \sigma_k) \quad (3.57)$$

is already in diagonal form. The Eigenvalues are given by

$$E_{m_1, m_2} = F(m_1^2 + m_2^2) + 2F'm_1m_2 \quad (3.58)$$

and labeled by the quantum numbers $m_1, m_2 \in \mathbb{Z}$. The symmetry of these eigenfunctions in the $C_{3v}^+ \otimes C_{3v}^-$ is easily obtained by rewriting

$$\Phi_{m_1, m_2}(\tau_1, \tau_2) = e^{im'_1\tau_+} e^{im'_2\tau_-} \quad (3.59)$$

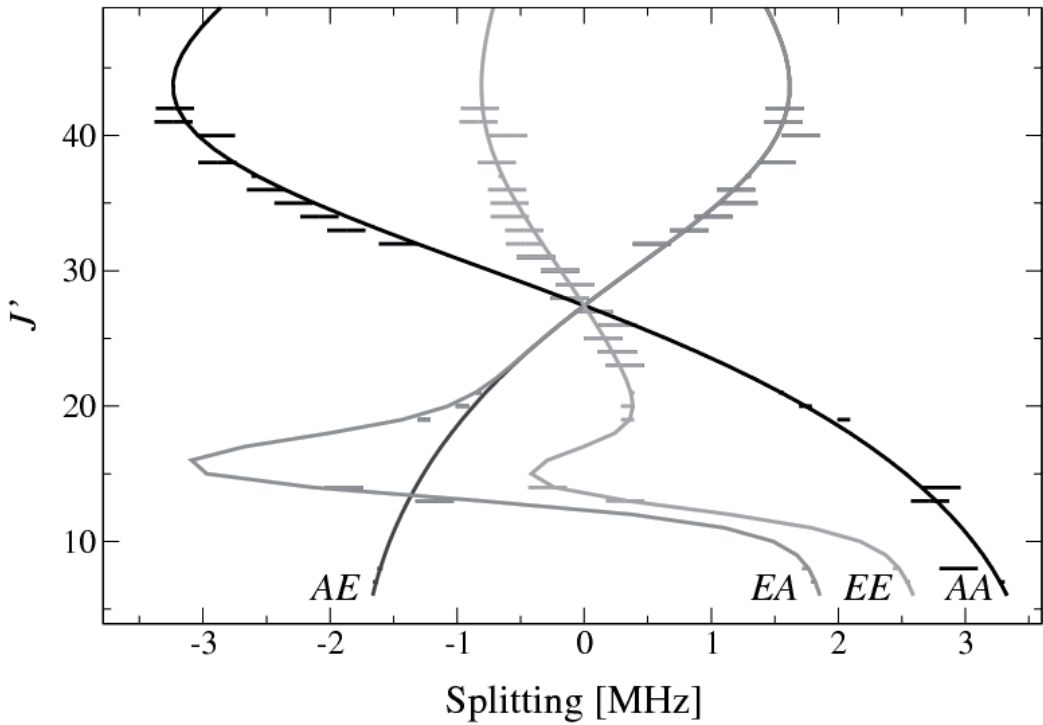


Figure 3.4: Torsional splitting for Q-branch transitions with $K_a = 6 - 5$, and $K_c = J - K_a + 1$ in the vibrational ground state of DME. The splitting is calculated by subtracting the predicted transition frequency which neglects all tunneling parameters from the transition frequencies. The solid lines connect calculated frequencies belonging to one of the four substates. Experimental data is shown as errorbars.

with

$$\begin{aligned} m'_1 &= \frac{1}{2}(m_1 + m_2) & m'_2 &= \frac{1}{2}(m_1 - m_2) \\ \tau_+ &= \tau_1 + \tau_2 & \tau_- &= \tau_1 - \tau_2 \end{aligned} \quad (3.60)$$

Levels with $\text{Mod}(m'_1, 3) = 0$ result in A , whereas levels with $\text{Mod}(m'_1, 3) = 1, 2$ give E symmetry in C_{3v}^+ subgroup and accordingly $\text{Mod}(m'_2, 3) = 0$ and $\text{Mod}(m'_2, 3) = 1, 2$ result in A and E symmetry in the subgroup C_{3v}^- . In the drawing shown in Fig. 3.5(a) the Eigenvalues are plotted in dependence of F' . As can be seen in the plot, the appearance of F' partly removes the degeneracy present at $F' = 0$. In particular the four-fold degeneracy of states having $AE \oplus EA$ symmetry is removed giving two two-fold degenerate states obeying AE and EA symmetry.

In the opposite case, the high barrier limit, the solutions approximate the solutions of a harmonic oscillator. If V_3 is large, the angles τ_1 and τ_2 are

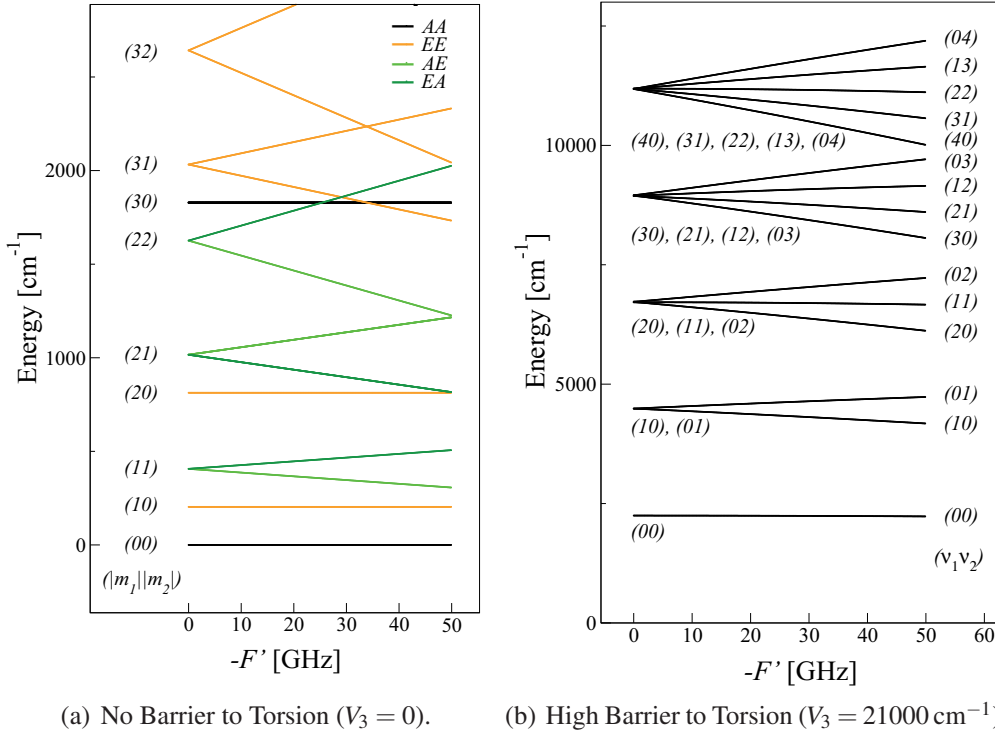


Figure 3.5: Calculated energy levels of the torsional modes of DME as a function of the top-top coupling term F' for the limiting cases of free internal rotation and a high barrier to torsion.

small and $\cos(3\tau_k)$ can be approximated by $1 - \frac{9}{2}\tau_k^2$. Thus

$$\begin{aligned}
 H_I(0,0) &= F(\mathbf{p}_1^2 + \mathbf{p}_2^2) + F'(\mathbf{p}_1\mathbf{p}_2 + \mathbf{p}_2\mathbf{p}_1) + \frac{1}{2}V_3(2 - \cos(3\tau_1) - \cos(3\tau_2)) \\
 &= F(\mathbf{p}_1^2 + \mathbf{p}_2^2) + F'(\mathbf{p}_1\mathbf{p}_2 + \mathbf{p}_2\mathbf{p}_1) + \frac{9}{4}V_3(\tau_1^2 + \tau_2^2)
 \end{aligned}
 \tag{3.61}$$

and if F' is neglected, the solutions are harmonic oscillator wave functions with eigenvalues

$$E = 3(FV_3)^{\frac{1}{2}}(v_1 + v_2 + 1)
 \tag{3.62}$$

In this limit the point symmetry group is C_{2v} and each state is $(v_1 + v_2 + 1)$ -fold degenerate, aside from the degeneracy concerning the substates AA , EE , AE , and EA . This $(v_1 + v_2 + 1)$ -fold degeneracy is removed by F' as can be seen in Fig. 3.5(b). The eigenvalues in both figures are obtained by diagonalizing the matrix elements of $H_I(0,0)$ in the free rotor basis $|j_1 \sigma_1\rangle |j_2 \sigma_2\rangle$ as given in Eq. 3.24. As V_3 increases the eigenvalues approximate the equidistantly separated eigenvalues of the harmonic oscillator.

In case of DME the barrier height is $V_3 \approx 1050 \text{ cm}^{-1}$ (see Tab. 4.7). Energy levels below the barrier are already arranged in a manner close to the high barrier limit as can be seen in Fig. 3.6(a). The levels can be classified by the two torsional modes. Each torsional state is split into four substates AA ,

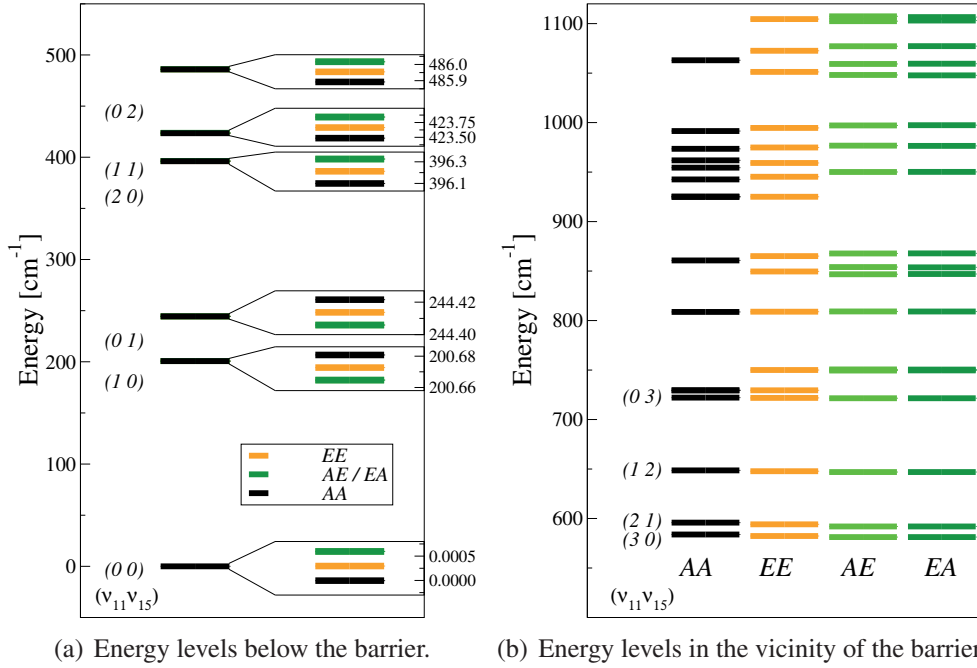


Figure 3.6: Calculated energy levels of the torsional modes of DME below and in the vicinity of the potential barrier to torsion $V_3 \approx 1050 \text{ cm}^{-1}$.

EE , AE , and EA . The size of the splitting increases as the torsional states approach the barrier to torsion. In the vicinity of the barrier the four substates are already largely shifted with respect to each other and the classification into the two torsional modes becomes ambiguous and less meaningful, as can be seen in Fig. 3.6(b) for torsional states above $(v_{11}v_{15})=(0\ 3)$.

Eigenfunctions of $H_I(K, -K)$ and Localized Functions

Besides the eigenvalues of $H_I(0,0)$ the eigenfunctions are obtained by diagonalization. Using an appropriate phase choice one obtains the functions whose contour plots are shown in Figs. 3.7 (real part) and 3.8 (imaginary part) for the torsional ground state $v=0$. The ground state is spanned by nine basis functions which are distributed to the four substates AA (1), EE (4), EA (2) and AE (2) as discussed above. The localized functions $\theta_{vq_1q_2}^{(0,0)}(\tau_1, \tau_2)$ are now obtained by rearranging Eq. 3.29:

$$\theta_{vq_1q_2}^{(0,0)}(\tau_1, \tau_2) = \sum_{\sigma_1=0}^2 \sum_{\sigma_2=0}^2 e^{i2\pi(q_1\sigma_1/n_1+q_2\sigma_2/n_2)} \Phi_{v\sigma_1\sigma_2}^{(0,0)}(\tau_1, \tau_2) \quad (3.63)$$

A complex phase choice can be found to remove the imaginary part of these functions. In Fig. 3.9 contour plots of all nine localized functions are shown. Their spatial probability distribution is located in one of the nine minima of the potential, which is why they are called localized functions. In the same manner, eigenfunctions of $H_I(K, -K)$ can be obtained for higher torsional states or values of $K \neq 0$, which are shown in Figs. 3.10 and 3.11 for

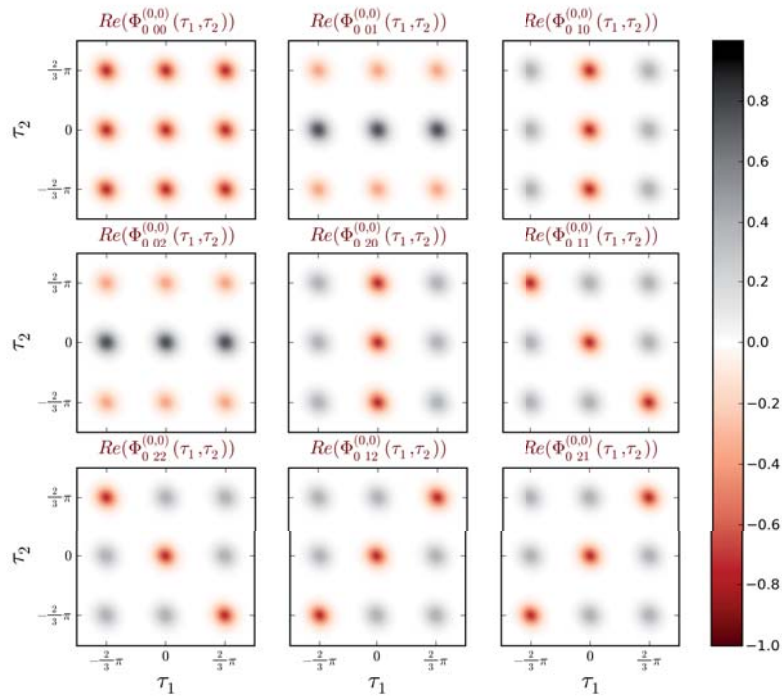


Figure 3.7: Real part of the solutions $\Phi_{v\sigma_1\sigma_2}^{(0,0)}$ of the internal Hamiltonian $H_I(0,0)$.

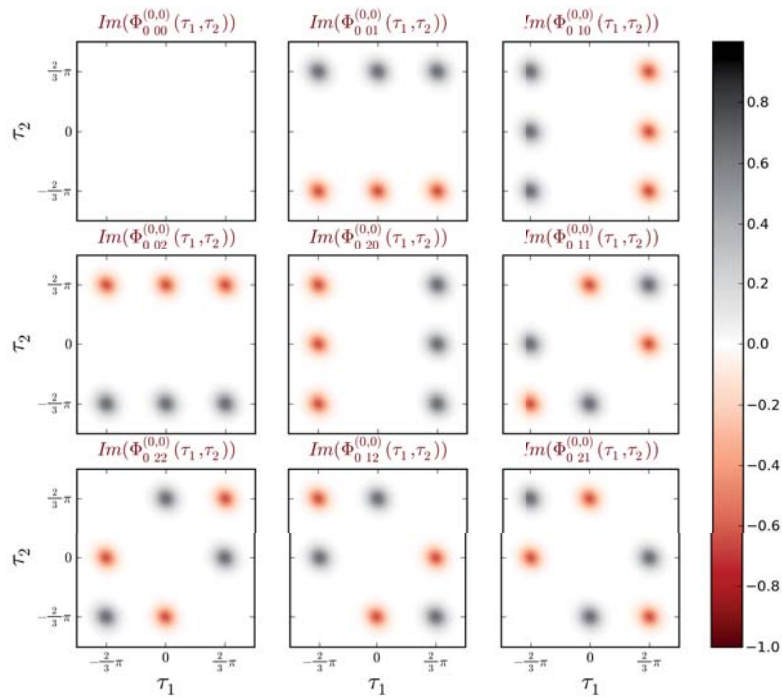


Figure 3.8: Imaginary part of the solutions $\Phi_{v\sigma_1\sigma_2}^{(0,0)}$ of the internal Hamiltonian $H_I(0,0)$.

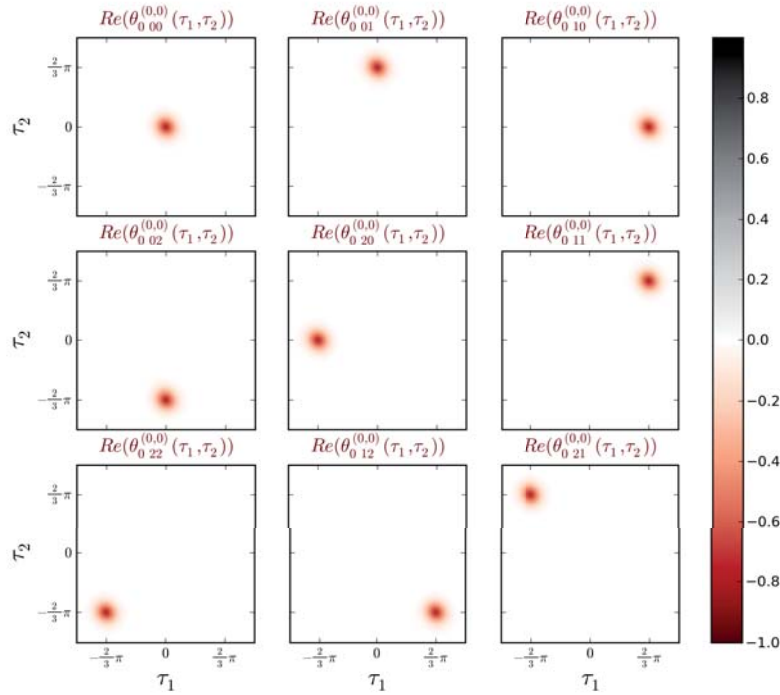


Figure 3.9: Localized functions $\theta_{vq_1q_2}^{(0,0)}$ of the internal Hamiltonian $H_I(0,0)$.

some exemplary values of ν and K with $\sigma_1 = 0$, $\sigma_2 = 0$. As can be seen in Fig. 3.10, the solutions build up harmonic oscillator wave functions within the potential minima. The quantum number ν is used to label the eigenfunctions as the sorted eigenvalues occur. Thus $\nu = 2$ identifies the (01)-state. As ν increases the probability density, which is centered in the potential minima for $\nu = 0$ is extended towards the barrier until the probability density overlaps in between the minima and significant probabilities are found at the potential wells between adjoining minima (see $\nu = 52$) if the energy of the state is beyond the barrier height. In the latter case the properties of the eigenfunctions have the character of free rotor functions.

In Fig. 3.11 the effect of increasing values of K can be seen for the torsional groundstate with $\sigma_1 = 0$, $\sigma_2 = 0$. The density probability is not notably affected if K changes. The eigenfunctions differ only in the phase function $\phi(\tau_1, \tau_2)$ depending on the torsional angles τ_1 and τ_2 which thus varies with K . In these calculations it has been assumed that F , which contains the reduced moments of inertia of the two internal tops, is constant, and centrifugal distortion of the tops is neglected.

3.6.7 Determination of the Potential Function $V(\tau_1, \tau_2)$

If the internal motion tunneling parameters $\epsilon_{q_1q_2}$ are known from fitting to the spectral lines, information about the two-dimensional potential function $V(\tau_1, \tau_2)$ can be obtained by a separate calculation. This calculation has the

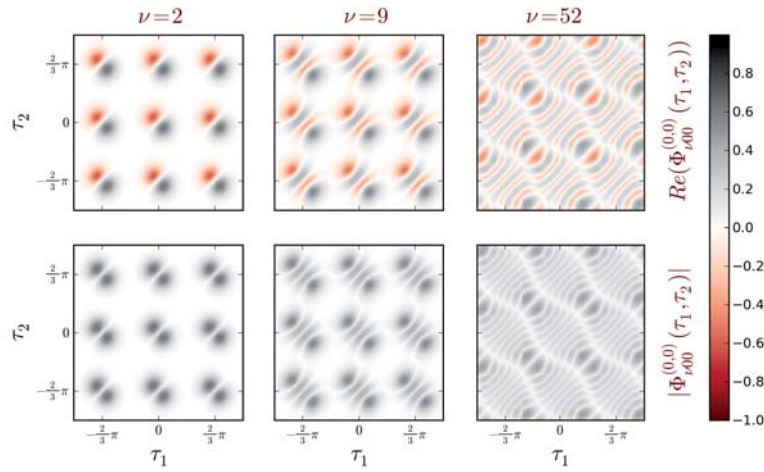


Figure 3.10: Solutions $\Phi_{\nu 00}^{(0,0)}$ of the internal Hamiltonian $H_I(0,0)$ for $\nu = 2, 9, 52$. The real part of the solutions are shown in the upper row, whereas the plot of its absolute values is shown in the lower row.

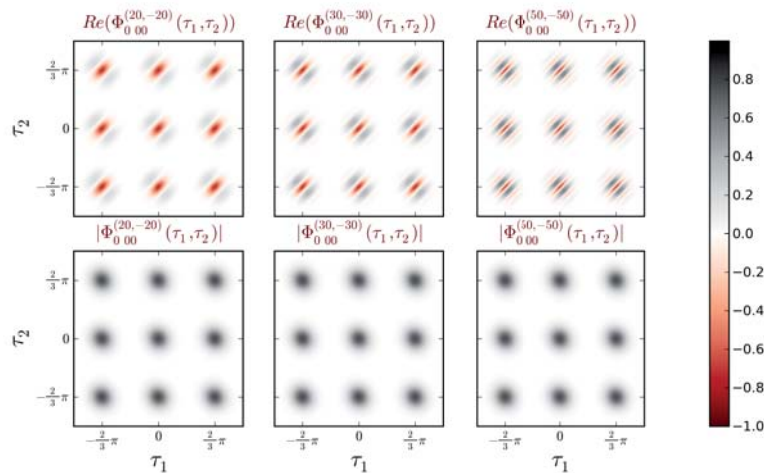


Figure 3.11: Solutions $\Phi_{000}^{(K,-K)}$ of the internal Hamiltonian $H_I(K,-K)$ for $K = 20, 30, 50$. The real part of the solutions are shown in the upper row, whereas the plot of its absolute values is shown in the lower row.

advantage that tunneling parameters of all analyzed states can be included as well as available frequencies from Raman and far-infrared spectra without being burdened by rotational spectra. The Fourier coefficients of $V(\tau_1, \tau_2)$ and $F^{(kl)}(\tau_1, \tau_2)$ can be fitted by diagonalizing the matrix of $H_I(0,0)$ and fitting the Fourier coefficients to the eigenvalues E which can be calculated using the tunneling parameters ε by Eq. 3.28. This approach is described in Chp. 4.5, where the potential function for DME is explicitly determined.

3.7 Perturbations in Excited Torsional States

Energy levels of torsional excited states are usually found at low energies, and their fundamental transition frequencies lie considerably below the bending modes. In molecules with two or more internal rotors, there are numerous torsional states at low energies, and the possibility of interactions between these states drastically increases. In DME, the two lowest torsional states are separated by $\approx 40 \text{ cm}^{-1}$ (see Tab. 4.6) and numerous rotational levels interact. In the rotational spectra of these states a large number of transitions is perturbed by second order Coriolis interactions. As will be outlined in Sec. 4.5, it is likely that Fermi resonances occur between combination energy levels of the coupled torsional modes and the bending mode, but they do not affect the states (10) and (01). In the analysis of rotational spectrum of the torsional excited states, this interaction is taken into account by adding matrix elements of the operators \mathbf{P}_c and $\mathbf{P}_a\mathbf{P}_b + \mathbf{P}_b\mathbf{P}_a$ including tunneling parameters.

3.8 Level Crossings

The main source of confusion in the line assignment was created through level crossings. This complicated the line assignments as the usual labeling scheme - based on the pseudo-quantum numbers K_a, K_c - can provoke a change of the quantum numbers of levels in the vicinity of the level crossing as soon as parameters slightly change. The asymmetry components are shifted differently by the internal rotation which can lead to level crossings (Fig. 3.12), as has been discussed in [11]. Both asymmetry components of the EA and the EE states have the same symmetry in the G_{36} group. As a consequence, asymmetry levels mix if the size of the asymmetry splitting decreases. The mixing predominantly affects transitions obeying b - and c -type selection rules of an ordinary asymmetric top molecule. On the other hand, the asymmetry components cannot be distinguished by the symmetry and the usual labeling by the pseudo-quantum numbers may fail and lead to c -type instead of b -type selection rules.

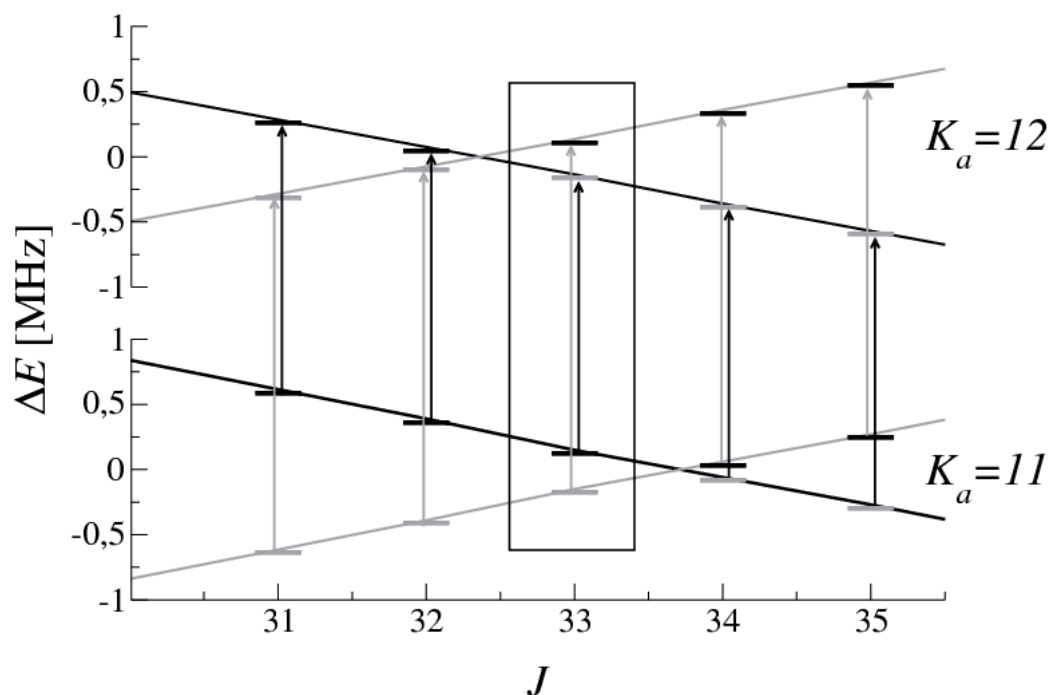


Figure 3.12: Crossing of the energy levels of the substate EE for $K_a = 11$ and $K_a = 12$ due to the torsional splitting. The gray and black colored bars indicate energy levels with $K_c = J - K_a + 1$ and $K_c = J - K_a$, respectively. ΔE is the energy difference between the energy of the corresponding asymmetry component and the averaged energy of both components. The arrows denote Q -branch transitions. The solid lines connect energy levels which belong to the same asymmetry component in dependence of J . Due to the crossing and the usual labeling scheme, the quantum numbers of the asymmetry components are interchanged (for $J = 35$ the black bars are located on the gray line and vice versa). The crossing is situated at different J values if K_a changes. Thus, c -type selection rules are obtained in the vicinity of the level crossings. In this example such a case, emphasized by the surrounding box, occurs at $J = 33$.

3.9 Fitting Spectra and Calculating Transition Frequencies

The computer programs ERHAM[12] and SPFIT [20] have been applied to analyze the spectra described in this work. Both programs were previously used to model the rotational spectrum of propane investigated by Drouin *et al.* [21]. Their work contains a detailed comparison of both routines, focussing on their applicability to the propane molecule, which belongs to the same symmetry class as DME. Experimental frequencies and parameters, which describe the individual terms of the Hamiltonian, are given via input files to the routines. Parameters are adjusted using a least squares analysis in order to model the experimental transition frequencies by calculating appropriate energy expressions. Transition frequencies and their intensities can then be predicted based on the derived parameter set. Both programs use effective Hamiltonians for asymmetric top molecules in either Watson's *A*- or *S*-reduction. These are common standard forms of the rotational Hamiltonian introduced by Watson [22, 23] in order to reduce the number of centrifugal distortion parameters and to overcome indeterminacies in the parameters. As a detailed description can also be found in a variety of textbooks such as [24], these reductions are not treated in further detail here. For the analysis of the rotational spectra of DME, the *A*-reduction has been used, which is

$$H^{(A)} = H_{rr} + H_d^{(4)} + H_d^{(6)} + \text{higher order terms} \quad (3.64)$$

with

$$\begin{aligned} H_{rr} &= B_x \mathbf{P}_x^2 + B_y \mathbf{P}_y^2 + B_z \mathbf{P}_z^2 \\ &= \frac{B_x + B_y}{2} \mathbf{P}^2 + \left(B_z - \frac{B_x + B_y}{2} \right) \mathbf{P}_z^2 + \frac{B_x - B_y}{2} (\mathbf{P}_x^2 - \mathbf{P}_y^2) \\ H_d^{(4)} &= \Delta_J \mathbf{P}^4 - \Delta_{JK} \mathbf{P}^2 \mathbf{P}_z^2 - \Delta_K \mathbf{P}_z^4 - 2\delta_J \mathbf{P}^2 (\mathbf{P}_x^2 - \mathbf{P}_y^2) - \delta_K \{ \mathbf{P}_z^2, (\mathbf{P}_x^2 - \mathbf{P}_y^2) \} \\ H_d^{(6)} &= \Phi_J \mathbf{P}^6 + \Phi_{JK} \mathbf{P}^4 \mathbf{P}_z^2 + \Phi_{KJ} \mathbf{P}^2 \mathbf{P}_z^4 + \Phi_K \mathbf{P}_z^6 \\ &\quad + 2\phi_J \mathbf{P}^4 (\mathbf{P}_x^2 - \mathbf{P}_y^2) + \phi_{JK} \mathbf{P}^2 \{ \mathbf{P}_z^2, (\mathbf{P}_x^2 - \mathbf{P}_y^2) \} + \phi_K \{ \mathbf{P}_z^4, (\mathbf{P}_x^2 - \mathbf{P}_y^2) \} \end{aligned} \quad (3.65)$$

In contrast to SPFIT, the program ERHAM is specially designed to model the rotational spectra of molecules with up to two periodic large-amplitude motions and uses the effective Hamiltonian as derived in Sec. 3.6.5. Currently, ERHAM does not account for terms connecting two different vibrational states. Thus, perturbations connecting different vibrational states, as they occur in the case of the excited torsional states of DME, cannot be accounted for.

SPFIT is designed as a general fitting routine to analyze the spectra of a variety of different molecular species. Amongst others, it is able to treat several vibrational states simultaneously by adding a vibrational energy term $E = G(\mathbf{v}') - G(\mathbf{v}'')$ to the energy expression, as well as terms describing effects of perturbation, if necessary. However, the description of the tunneling

splitting is less accurate in SPFIT, as no input coding is provided for the projection operator $Y_{K'K}(K_1, K_2)$, which is described in Eq. 3.52. Thus, the internal rotation terms, calculated in the ρ -axis systems of the individual tops, cannot be transformed to the principal axis system. As an alternative, H. Pickett proposed a rotated internal axis system (RIAS) [25], in which the internal rotation terms can be derived and implemented in SPFIT.

3.10 The RIAS Approach

The SPFIT routine does not provide an implementation of the $Y_{K'K}(K_1, K_2)$ -terms, which occur in Eq. 3.52, and in the fits of DME, these terms are thus neglected. This approach is motivated by the use of a rotated internal axis system (RIAS). The torsional Hamiltonian H_I is transformed into the RIAS, which is aligned to the a -axis of the molecule:

$$\begin{aligned}
 H_I &= \sum_{k=1}^2 \sum_{l=1}^2 (\mathbf{p}_k - \rho_k \mathbf{P}) F^{(kl)}(\mathbf{p}_l - \rho_l \mathbf{P}) + V \\
 &= \sum_{k=1}^2 \sum_{l=1}^2 (\mathbf{p}_k - \rho_{a,k} \mathbf{P}_a - \rho_{b,k} \mathbf{P}_b) F^{(kl)}(\mathbf{p}_l - \rho_{a,l} \mathbf{P}_a - \rho_{b,l} \mathbf{P}_b) + V \\
 &= \sum_{k=1}^2 \sum_{l=1}^2 (\mathbf{p}_k - \rho_{a,k} \mathbf{P}_a) F^{(kl)}(\mathbf{p}_l - \rho_{a,l} \mathbf{P}_a) - \rho_{b,k} \rho_{b,l} F^{(kl)} \mathbf{P}_b^2 + V \\
 &\quad - \rho_{b,k} \mathbf{P}_b F^{(kl)}(\mathbf{p}_l - \rho_{a,l} \mathbf{P}_a) - (\mathbf{p}_k - \rho_{a,k} \mathbf{P}_a) F^{(kl)} \rho_{b,l} \mathbf{P}_b
 \end{aligned} \tag{3.66}$$

As $\rho_{b,k} \rho_{b,l} F^{(kl)}$ are constants and thus do not have a periodic K -dependence, it is assumed that the terms $\rho_{b,k} \rho_{b,l} F^{(kl)} \mathbf{P}_b^2$ are absorbed into the rotational part of the Hamiltonian and result in small offsets of the rotational parameters. The first order cross terms with $\rho_{b,k} \mathbf{P}_b$

$$H'_I = \sum_{k=1}^2 \sum_{l=1}^2 -\rho_{b,k} \mathbf{P}_b F^{(kl)}(\mathbf{p}_l - \rho_{a,l} \mathbf{P}_a) - (\mathbf{p}_k - \rho_{a,k} \mathbf{P}_a) F^{(kl)} \rho_{b,l} \mathbf{P}_b \tag{3.67}$$

are expected to be small. In the current version of SPFIT, Fourier-terms for \mathbf{P}_b cannot be included due to the requirement of the phase choice that allows the Hamiltonian to be completely real. Thus, they have to be neglected in the analysis of the rotational spectrum of dimethyl ether. As H'_I increases with J , its neglect becomes more noticeable for high values of J , as can be seen especially by comparing the splitting calculated with ERHAM and SPFIT shown in Fig.4.3. The internal Hamiltonian used in the SPFIT approach therefore reduces to

$$H_I = \sum_{k=1}^2 \sum_{l=1}^2 (\mathbf{p}_k - \rho_{a,k} \mathbf{P}_a) F^{(kl)}(\mathbf{p}_l - \rho_{a,l} \mathbf{P}_a) + V \tag{3.68}$$

and slightly modified $C'_{qq'}$ -functions (Eq. 3.55) in the effective Hamiltonian are obtained:

$$C'_{qq'} = \cos(2\pi(q(\sigma_1 - \rho_a K) + q'(\sigma_2 - s\rho_a K))/n) \quad (3.69)$$

In this approach K_1, K_2 are replaced by K, sK as well as ρ which is replaced by $\rho_a = \rho \cos(\beta)$.

4

Observed Spectrum and Analysis

4.1 Experimental Details

Torsion-rotational spectra of DME were recorded in Cologne and at the Jet Propulsion Laboratory (JPL)¹ in the millimeter and submillimeter wave regions. Several broad scans were performed, which cover several frequency regions completely. In Cologne, the complete frequency range from 38–56 GHz and from 550–610 GHz was recorded. Furthermore, numerous spectra of single transitions have been measured up to almost 2.1 THz. Below 60 GHz a commercial synthesizer was used as radiation source and the signal was detected after a 6 m long absorption cell by a Schottky diode. Higher frequencies were accessed with several phase locked Backward Wave Oscillators (BWO) (see [26] for details). The high output power of the BWOs gave access to weaker transitions up to 900 GHz with good signal to noise ratios. The line survey from 550–610 GHz and transition frequencies above 900 GHz were carried out with BWOs in combination with superlattice frequency multipliers as radiation sources. A detailed description of the experimental setups is given in part II. Both setups used InSb hot electron bolometers for detection and an absorption cell of 3 m length. The BWOs were phase locked to a rubidium reference to assure a frequency stability of $\Delta f/f = 10^{-11}$. In Cologne spectra were recorded with $2f$ -frequency modulation technique for better signal to noise ratios. At the JPL, frequency stabilized multiplier chains have been applied to record broad band spectra from 766 to 930 GHz, 983 to 1158 GHz, and from 1.58 to 1.67 THz. The radiation was detected by a Si-composite bolometer after doubly passing the 2.5 m absorption cell. Tone burst modulation was used for detection. The JPL setup is locked to one part in 10^{12} , so that the achievable transition frequency accuracy depends only on the quality of the spectrum. A detailed description of this setup is given in [27]. All measurements were carried out at room temperature and the pressure in the absorption cell was typically in the order of 1 Pa, but pressures up to 10 Pa have been used to measure weaker lines.

¹The spectra recorded at the JPL have been measured by B. J. Drouin

Table 4.1: Characterization of the different datasets used in the fit. The first four rows summarize transitions measured within this work. The number of assigned transitions is given followed by the number of different frequencies in parenthesis. The last column shows the unitless weighted standard deviation of the dataset in the fit.

Source	# of Transitions	Max. J	Max K_a	Frequency [GHz]		σ
				Min.	Max.	
Synthesizer (Cologne)	344 (259)	54	19	39	56	1.02
BWO (Cologne)	586 (273)	70	27	69	897	0.90
BWO + SL (Cologne)	1663 (635)	63	27	263	2099	0.95
Multiplier chain (JPL)	2234 (435)	67	30	780	1665	1.08
Niide [28]	16 (13)	7	2	12	25	1.77
Durig [8]	20 (15)	4	1	29	36	0.50
Lovas [9]	191 (157)	22	6	9	112	0.74
Neustock [10]	79 (66)	24	5	63	222	0.96
Groner (Klystron) [11]	962 (702)	25	6	94	544	1.08
Groner (FASSST) [11]	735 (386)	49	10	263	340	0.85

Lines were not included in the analysis if the line profile was not sufficiently well reproduced by Gaussian fits to the experimental spectrum due to very complicated structure or due to unknown blends, because the uncertainty for those lines is easily underestimated. A significant number of line assignments were verified by calculating closed loops of transitions. The quality of predicted line position and the usually characteristic intensity patterns helped assigning the transitions.

4.2 Ground State Spectrum

1602 new lines were measured in total and assigned to 4827 transitions. Energy levels including $J = 70$ and $K_a = 30$ were accessed. A summary of the experimental lines is given in Tab. 4.1. The line accuracies were estimated for each single line individually with regard of the line profile fit and are listed in Tab. B.1 of the appendix²; typical accuracies were 100 kHz. For isolated, unblended lines accuracies of 20 kHz were achieved. Frequently, lines overlapped due to an unresolved splitting or by other nearby lines and the line profile was distorted. Although the blend of lines was considered in the line profile fit, it generally caused the most significant contribution to the uncertainty of the experimental line frequencies. In the frequency range from 39–56 GHz 344 transitions were recorded accessing energy levels with $J = 54$ and $K = 19$. The line widths are small enough at these frequencies to resolve the torsional splitting into the four substates AA , EE , AE , and EA completely for a large number of transitions and at most blending of the substates AE and EA was observed. An example of a transition with completely resolved torsional splitting has already been shown in Fig. 3.2.

²The appendix B can only be obtained in electronic form via http://www.cuvillier-verlag.de/assets/mime/-UTQ3ZXHNcHnxcUdsDGJkfZ8gBeY7++wRdCJJoPYE8gvo8rw3/Appendix_B.pdf

The fundamental spin statistical weights are well represented in this spectral recording. These transitions provide valuable information, in particular for the accurate determination of the torsional splitting in energy levels with higher J and K values, because at high frequencies the transitions involving these energy levels are usually blended due to the increased Doppler width. The signal-to-noise ratio allowed the observation of even very weak lines and a reasonable number of P -branch as well as $\Delta K = 3$ transitions were recorded. The already huge dataset in the mm-wavelength region reported in the literature was supplemented by several weaker lines and some of the reported frequencies were remeasured if they deviated largely from their predicted frequencies. The majority of recorded transitions were assigned at frequencies between 500 and 1000 GHz. In particular, Q -branch transitions including energy levels with high J quantum numbers up to 70 and fairly high K_a values up to 16 have been added. Broad scans have been performed in order to cover large frequency regions. Weaker transitions, in particular at high J values up to $J = 70$, have been recorded by the use of the BWO THz spectrometer. The density of spectral lines complicates the detection and the unambiguous assignment of a variety of weaker transitions including higher J quantum numbers, which hampered even more extensive assignments. Mainly relatively strong R -branch transitions were accessed at frequencies above 1 THz involving energy levels with higher K_a values up to $K_a = 27$ at around 2 THz. The splitting was usually too small to be even partly resolved in the Doppler limited measurements in this frequency domain. Fig. 4.1 shows a typical transition above 2 THz.

The line assignments were relatively straightforward because of the quite large dataset. Using predictions based on this dataset, transitions in the spectra could be assigned step by step by improving frequency predictions iteratively, including higher J and K values to the fit. The main source of confusion occurred due to level crossings which complicated the line assignments as already described in Sec. 3.8

All lines were included in the analysis, including all previously reported ones. No blended lines were excluded, in contrast to the work of Groner *et al.* [11], provided that the line profile could be sufficiently well reproduced. An overview of the lines used in the fit is given in Tab. 4.1. In cases where the same transition was reported in different papers, the frequency which fitted best was used in the fit. All other previously reported transitions were treated with their reported uncertainties and weighted accordingly in the fit, except transitions recorded with the *FASSST* spectrometer. Based on the analysis, the accuracy of this dataset is supposed to be slightly worse than 100 kHz on average. An accuracy of 150 kHz was used in the analysis instead. The dataset contains a large number of blended lines. In the least-squares fit, the intensity weighted frequency averages of the components of these blended transitions were used. The intensities were taken from predictions. Although systematic fitting problems associated with improper intensity predictions cannot be excluded and could lead to an incorrect description of the splitting, the matching of simulated and measured spectra shows no obvious problems.

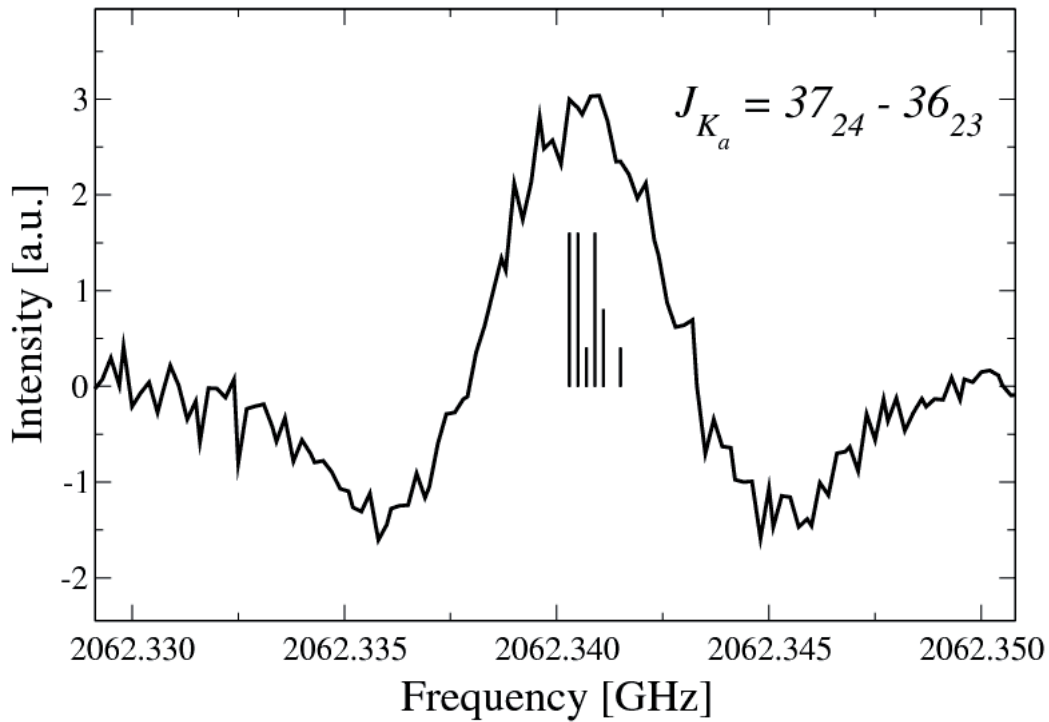


Figure 4.1: Rotational transition ($J_{K_a} = 37_{24} - 36_{23}$) in the ground state of DME at 2.06 THz. The spectrum recorded by the use of the 9th harmonic generated by a superlattice frequency multiplier [29] shows a typical line at frequencies around 2 THz. At these frequencies the torsional splitting remains usually unresolved due to the Doppler width.

In particular, the measurements at low frequencies confirm the agreement, because most of the transitions are fully resolved at high accuracies for a wide range of J and K values up to 54 and 19. The agreement between both, the experimental and calculated splitting is exemplary, as shown in Fig. 3.4 for Q -branch transitions with $K_a = 6 - 5$ and $K_c = J - K_a + 1$. The solid lines connect calculated frequencies belonging to one of the four substates AA , EE , AE , and EA . The experimental values fit nicely within the given errors.

The analysis was performed using the computer programs ERHAM [12] and SPFIT [20], which have been described in Sec. 3.9. In the present fit an asymmetric rotor Hamiltonian in Watson's A reduction has been used. The molecular axes are labeled according to the I' representation (prolate rotor), which is $x = b$, $z = a$, and $y = c$. In total, 6830 transitions have been fitted using 34 spectroscopic parameters. 21 parameters correspond to rotational and centrifugal distortion constants up to the eighth order. In addition to the internal rotation parameters ρ and β , one energy tunneling parameter, ϵ_{10} , and ten tunneling parameters associated with the rotational constants were determined. The values of all parameters including their uncertainties are given in Tab. 4.2. The experimental dataset could be fit with ERHAM to experimental precision and a reduced standard deviation of $\sigma_{red} = 0.99$ was obtained. 30 frequencies deviated more than 3σ , but no

line more than 4.3σ . The reduced standard deviation is reported for each dataset used in the fit in Tab. 4.1. The fit with SPFIT is slightly worse and the same experimental dataset could only be fitted to $\sigma_{red} = 1.5$ with a comparable number of parameters. The σ_{red} can be further reduced to 1.1 by the extensive use of tunneling parameters. However the parameters are so strongly correlated in that case that the result of the fit and generated predictions become questionable.

Table 4.2: Spectroscopic parameters for DME in the vibrational ground state. The non-tunneling parameters $T_l^{(k)}{}_{00}$ are labeled using the common notation for rotational constants. For tunneling parameters the notation $[]_{qq'}$ has been used with the commonly used notation of corresponding non-tunneling parameter enclosed in brackets.

Parameter	This work	Groner <i>et al.</i> [11]
ρ	0.217131(37)	0.21709(21)
β (deg)	9.117(17)	8.631(13)
A (MHz)	38788.18325(28)	38788.17932(71)
B (MHz)	10056.482389(77)	10056.48166(18)
C (MHz)	8886.829843(75)	8886.82907(19)
Δ_J (kHz)	9.085900(59)	9.08387(36)
Δ_{JK} (kHz)	-26.86387(64)	-26.8656(39)
Δ_K (kHz)	341.9520(17)	341.721(41)
δ_J (kHz)	1.775148(25)	1.775099(53)
δ_K (kHz)	-13.8034(12)	-13.7825(44)
Φ_J (Hz)	0.007798(12)	0.00703(19)
Φ_{JK} (Hz)	0.1122(28)	0.1121(67)
Φ_{KJ} (Hz)	-4.0865(90)	-3.847(88)
Φ_K (Hz)	13.7300(72)	8.38(107)
ϕ_J (Hz)	0.003796(16)	0.003745(43)
ϕ_{JK} (Hz)	0.31571(57)	0.3341(57)
ϕ_K (Hz)	1.010(91)	1.50(22)
L_{JKK} (mHz)	0.00687(95)	
L_{JK} (mHz)	0.3079(35)	
L_{JKK} (mHz)	-0.7941(54)	
l_J (mHz)	0.0000260(30)	
l_{JKK} (mHz)	0.290(31)	
l_K (mHz)	6.671(37)	
Tunneling parameters		
ϵ_{10} (MHz)	-3.0445(11)	-3.0435(41)
ϵ_{20} (MHz)		0.0053(16)
$[A - (B + C)/2]_{10}$ (kHz)	2.149(36)	1.64(21)
$[(B + C)/2]_{10}$ (kHz)	-0.416(11)	-0.0364(63)
$[(B - C)/4]_{10}$ (kHz)	-0.0908(92)	0.1116(37)
$[\Delta_J]_{10}$ (Hz)	0.2209(48)	
$[\Delta_{JK}]_{10}$ (Hz)	-1.797(36)	
$[\Delta_K]_{10}$ (Hz)	1.74(16)	
$[\delta_J]_{10}$ (Hz)	0.1579(82)	
$[\delta_K]_{10}$ (Hz)	1.099(64)	
$[\phi_J]_{10}$ (mHz)	-0.0432(16)	
$[\phi_K]_{10}$ (mHz)	-2.29(22)	

Table 4.3: Characterization of the different datasets used in the fit. Transitions measured with the FASSST spectrometer have been assigned within the scope of this work.

Source	# of Transitions	Max. J	Max K_a	Frequency [GHz]	
				Min.	Max.
Synthesizer ^a	404	47	15	38	56
Synthesizer+Tripler ^a	238	21	6	75	120
BWO ^a	36	43	8	760	790
BWO (+ SL) ^a	638	37	10	500	750
Multiplier chain ^b	2908	59	21	760	1670
FASSST [12]	5259	49	13	120	500
Literature [13],[8], [28]	52	5	2	8	36

^a Cologne.

^b JPL.

4.3 Excited Torsional States

The limited dataset of 52 transition frequencies in the excited torsional states (10) and (01) of DME reported in the literature so far, has been greatly extended from 52 to 9535 transitions, which have been assigned to 7613 frequencies. 4908 transitions belong to the (10)-state and 4601 to the (01)-state. Energy levels up to quantum numbers of $J = 59$ for the (10)-state and $J = 57$ for the (01)-state and $K_a = 21$ for both states have been accessed. The experimental lines are summarized in Tab. 4.3. The line accuracies were estimated for each line individually based on the line profile fit. As already mentioned in the previous section, the most significant contribution to the uncertainty was the blend with nearby lines, although this has been considered in the line profile fit. A frequency list of peak intensities derived from spectra recorded with the FASSST spectrometer, has been provided by Groner and Herbst *et al.* [30]. These spectra have been recorded within their work on the vibrational ground state [11]. An estimated error of 200 kHz has been generally assigned to these transitions.

Transitions in the spectra have been assigned step by step, using iteratively improved frequency predictions. The assignment was hampered by the density of spectral lines. In some parts of the spectra, the blend of lines prevented unambiguous line assignments. This is especially true for those regions where Q -branch transitions are observed. Generally, the assignments have been proved by closed loops of transitions. This way, 4477 assignments have been checked using only closed loops of experimentally recorded transitions. These transitions are indicated in the line list given in Tab. B.2 of the appendix³. However, mainly transitions involving low and medium quantum numbers in J and K_a have been accessed by this method. The inspection of the torsional splitting also revealed valuable information. Diagrams, for

³The appendix B can only be obtained in electronic form via http://www.cuvillier-verlag.de/assets/mime/-UTQ3ZXHNcHnxcUdsDGJkfZ8gBeY7++wRdCJJoPYE8gvo8rw3/Appendix_B.pdf

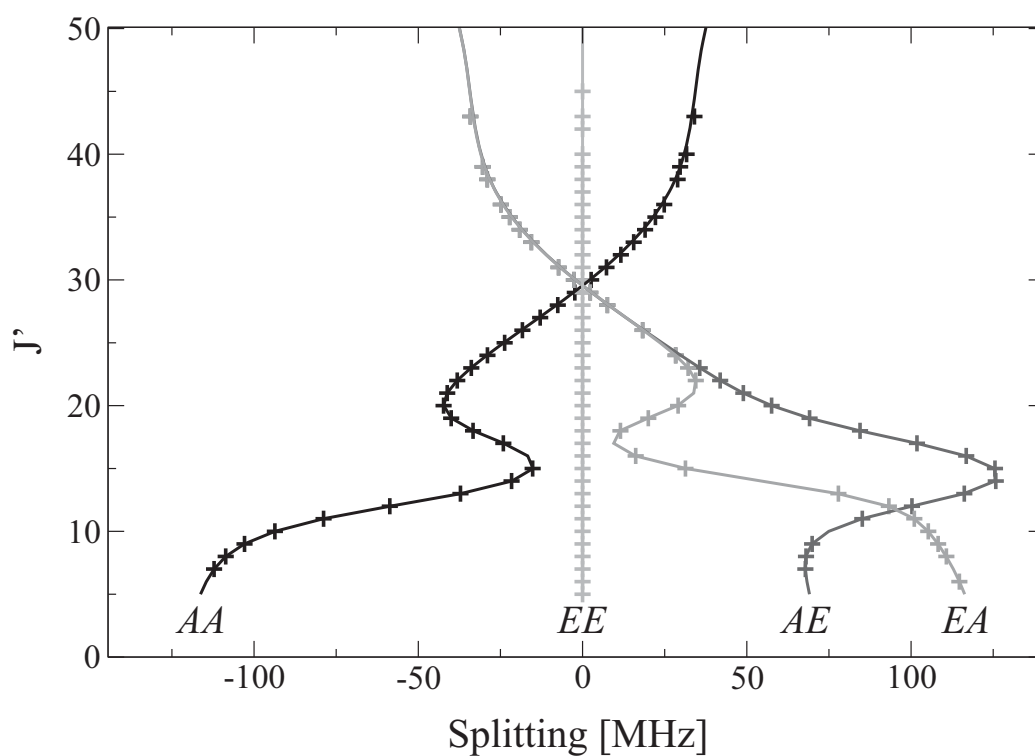
example as in Fig. 4.2, where the torsional splitting is plotted against the angular momentum J , provide other useful tools supporting the line assignment. As discussed below, the quality of predictions is not always satisfactory for transitions obeying severe interactions or for transitions with high J or K_a quantum numbers, in which the predicted shift due to the splitting is not always accurately predicted.

Second order Coriolis perturbations between both states have been observed for various rotational levels obeying the selection rules $\Delta J = 0$, $\Delta K_a = \pm 3, \pm 5, \dots$ and $\Delta K_c = \pm 2, 4$ ($oo \leftrightarrow eo$, $ee \leftrightarrow oe$, $oe \leftrightarrow ee$, $eo \leftrightarrow oo$). An exemplary interaction, which stretches across a long range of J values, is the interaction between the energy levels $J_{6,J-6}$ and $J_{9,J-9}$ of the (01) and the (10)-state, respectively. As shown in Fig. 4.4, the interaction ranges from J -values of 25 up to 45, and reaches its maximum at $J = 33$.

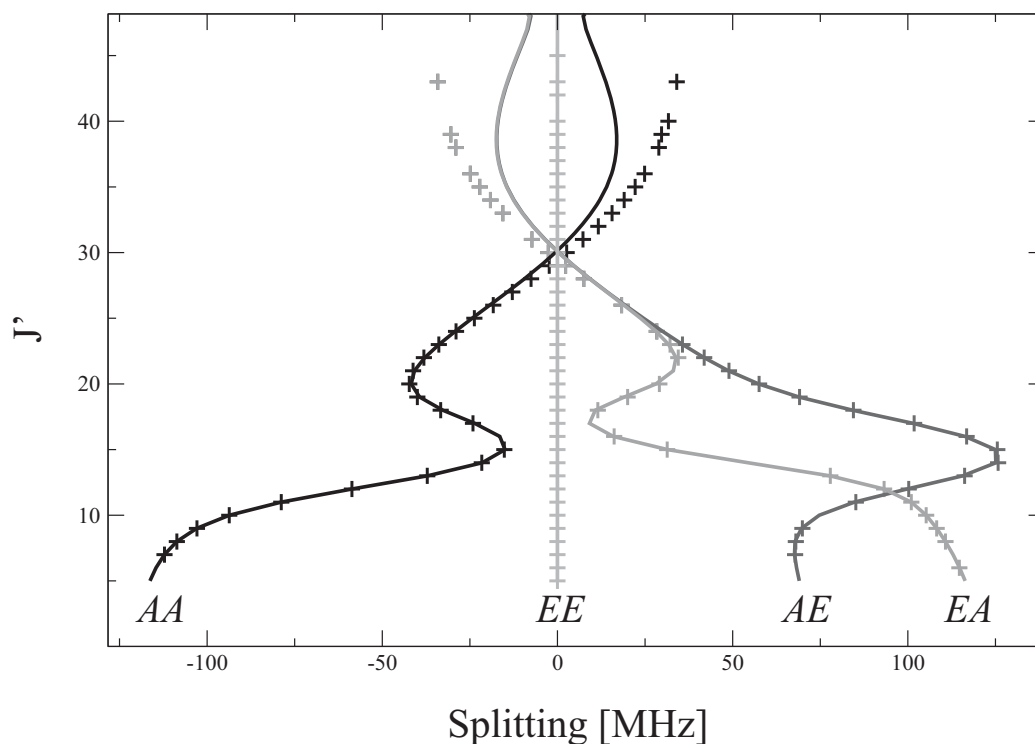
In total, several 100 perturbed transitions have been assigned. As wavefunctions of perturbed energy levels mix, 26 transitions between both torsional excited states have been observed and assigned. Their intensity is usually weak and the assignment somewhat ambiguous. However, it has been possible to prove the consistency in numerous cases by closed loops of transitions. Nevertheless, these transitions have been included in the fit, because they contain valuable information about the energy difference between both excited torsional states, and have been reproduced well within the fit. Generally, the torsional splitting into the four substates AA , EE , AE , and EA was resolved in most cases, due to the enlarged size of the splitting compared to the ground state. Only the splittings between the substates AE and EA are blended in numerous cases.

Analogous to the ground state analysis, the two fitting routines ERHAM and SPFIT have been used to interpolate the spectroscopic data to an asymmetric rotor Hamiltonian in Watson's A reduction. Both the ERHAM ([12]) and the SPFIT ([20]) approach have significant drawbacks, as has been discussed in Sec. 3.9. An overview of the obtained spectroscopic parameters is given in Tab. 4.4.

As ERHAM currently does not account for the interaction, only unperturbed transitions can be included in the fit. Therefore, both states have been fitted separately in the ERHAM treatment and the treatment differs only in the number of parameters from the ground state fit described in the previous section. Distorted transitions have been excluded from the fits. Numerous transitions are only slightly distorted and it is not always obvious whether lines are distorted or just badly reproduced by the fits. A significant contribution to the standard deviation of the fits is believed to originate from those slightly distorted lines. On the other hand, a number of transitions - in particular in the frequency range 38-58 GHz - deviate in the order of a few 100 kHz, which probably pinpoints the limits of this model. In the (10)-state, 18 rotational constants and 9 tunneling parameters have been determined and result in a reduced standard deviation of 8.8 for the 4329 assigned transitions. In the fit of the (01)-state, the 3363 included transitions



(a) Predictions calculated with ERHAM.



(b) Predictions calculated with SPFIT.

Figure 4.2: Torsional splitting for Q-branch transitions with $K_a = 5 - 4$, and $K_c = J - K_a + 1$ in the torsional excited state (01). The splitting is calculated by subtracting the predicted transition frequency of the EE state from the transition frequencies. The solid lines connect calculated frequencies belonging to one of the four substates. Experimental data is shown as dots. The experimental error is not shown, because it is too small. The predictions shown in the figures are either based on calculation done with ERHAM or SPFIT for comparison.

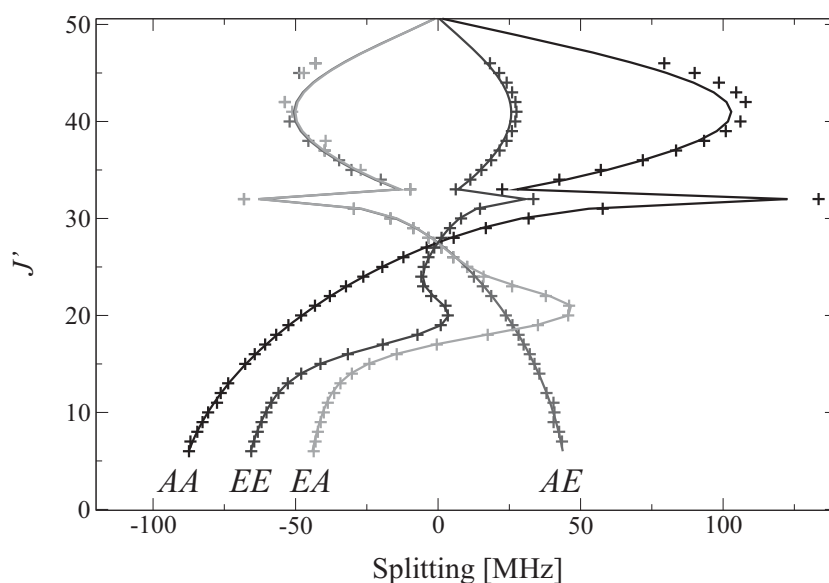


Figure 4.3: Torsional splitting for perturbed Q-branch transitions with $K_a = 6 - 5$, and $K_c = J - K_a$ in the torsional excited state (01). The Coriolis perturbation reaches its maximum at $J' = 33$ and causes a significant effect on the size of the splitting. The splitting is calculated by subtracting the predicted transition frequency, which neglects all tunneling parameters from the transition frequencies. The solid lines connect calculated frequencies belonging to one of the four sub-states. Experimental data is shown as dots. The experimental error is not shown, because it is too small.

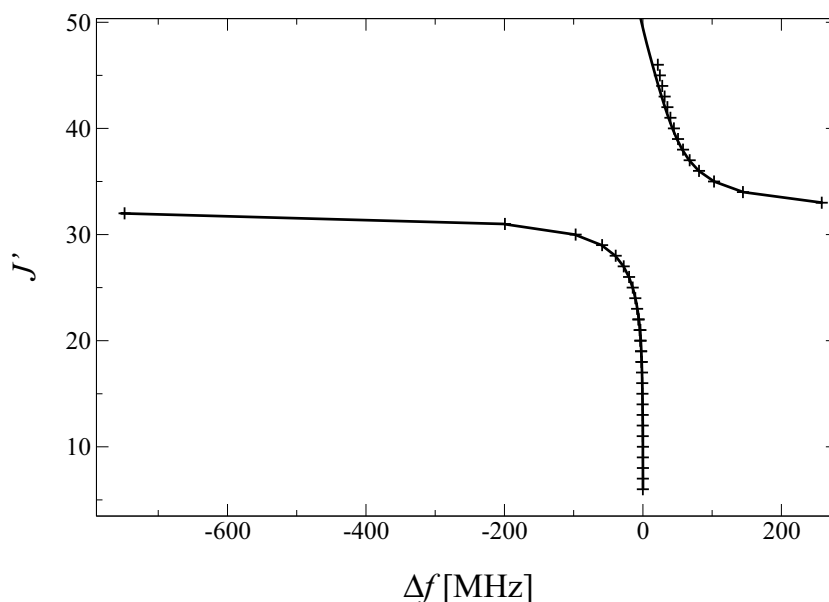


Figure 4.4: Perturbation of the energy levels within the excited torsional state (01) for the substate EE . The quantum number J is plotted against the frequency difference, which is the calculated difference between predicted transition frequencies accounting for and neglecting the interaction. In the figure the transitions $J_{K_a, K_c} = J_{6, J-6} - J_{5, J-5}$ are shown. The solid lines connect calculated frequencies and experimental data is shown as dots.

are slightly better reproduced, and a standard deviation of 5.05 has been achieved by the use of 18 rotational constants and 9 tunneling parameters.

In the SPFIT treatment, all 9535 assigned transitions of the excited torsional states have been adjusted within one global fit. The perturbation is described by the additional matrix elements

$$\langle JKM\nu\sigma_1\sigma_2|\mathbf{P}_c\Sigma_{P_c} + (\mathbf{P}_a\mathbf{P}_b + \mathbf{P}_b\mathbf{P}_a)\Sigma_{P_aP_b+P_bP_a}|JKM\nu'\sigma_1\sigma_2\rangle \quad . \quad (4.1)$$

The torsional splitting is largely affected by the perturbation, and the avoided crossing as shown in Fig. 4.4. This leads to a similar discontinuity, if the J dependence of the torsional splitting is depicted as in Fig. 4.3. Tunneling parameters for the operators \mathbf{P}_c and $\mathbf{P}_a\mathbf{P}_b + \mathbf{P}_b\mathbf{P}_a$ are necessary for an accurate treatment. In the fit, 16 ($\nu_{11} = 1$) and 17 ($\nu_{15} = 1$) rotational as well as 20 tunneling parameters have been included individually for both states. The states are connected in the fit via the parameters G_c , F_{ab} and their tunneling parameters $[G_c]_{10}$ and $[F_{ab}]_{10}$, as well as the energy difference $E = E_{01} - E_{10}$ of both states. As already mentioned, the less accurate description of the tunneling splitting in SPFIT hampers a more accurate interpolation, and only a weighted standard deviation of $\sigma = 15.9$ could be achieved. While the interaction is generally well reproduced, the splitting matches more poorly than in the ERHAM-Fit, as can be seen by comparing Fig. 4.2(a) and 4.2(b) for the reasons discussed in Sec. 3.10. The standard deviation can be further reduced by a more extensive use of tunneling parameters, but due to the strong correlation between these parameters it is desisted from doing so.

The matrix elements $Y_{K'K}(K_1, K_2)$ cannot be included in SPFIT, and the spectroscopic parameters refer to the RIAS. Thus, only the projection of ρ onto the a -axis is obtained, which is related by $\rho_a = \rho \cos \beta$ to the spectroscopic parameters obtained by ERHAM. In SPFIT, ρ_a is not deduced by the least-squares fit and has been optimized manually. Its values agree with the related values from the ERHAM treatment for both states. The applied Hamiltonian is analogous to the Hamiltonian applied in ERHAM, if $\beta = \beta_1 = \pi - \beta_2$ is fixed to zero. In this case, the ρ -axis coincides with the a -axis of the reference system. For DME, the angle between ρ - and a -axis is $\beta \approx 9^\circ$. Thus, $\rho_b \approx 0.035$ and the neglect of the first order cross terms with $\rho_{b,k}\mathbf{P}_b$,

$$H'_I = \sum_{k=1}^2 \sum_{l=1}^2 -\rho_{b,k}\mathbf{P}_b F^{(kl)}(\mathbf{p}_l - \rho_{a,l}\mathbf{P}_a) - (\mathbf{p}_k - \rho_{a,k}\mathbf{P}_a) F^{(kl)}\rho_{b,l}\mathbf{P}_b \quad (4.2)$$

results in a reasonable approximation. But at large values of J , and in particular in combination with low values of K_a , the neglected terms grow increasingly important and deviations become noticeable, as shown in Fig. 4.2(b). In the fit, tunneling parameters connected to rotational operators can compensate this deviation up to some degree, which reduces the standard deviation of the fit, but an excessive use of these parameters may decrease the accuracy of inter- and extrapolated frequency predictions.

Table 4.4: Spectroscopic parameters for DME in its excited torsional states (10) and (01). The non-tunneling parameters $T_l^{(\kappa)}_{00}$ are labeled using the common notation for rotational constants. For tunneling parameters the notation $[]_{qq}$ has been used with the commonly used notation of corresponding non-tunneling parameter enclosed by the brackets.

Parameter	ERHAM (separate fits)		SPFIT (global fit)	
	(10)-state	(01)-state	(10)-state	(01)-state
ΔE [cm^{-1}]				43744.3491(35)
ρ	0.2180047(210)	0.2145584(146)		
ρ_a			0.21522(0)	0.21210(0)
β [deg]	9.1489(159)	8.8239(172)		
A [MHz]	38829.77662(679)	38801.34076(437)	38829.75630(940)	38801.42670(912)
B [MHz]	10025.79333(144)	9993.86471(105)	10025.79820(919)	9993.86270(926)
C [MHz]	8867.55446(133)	8870.355322(913)	8876.87260(919)	8861.05710(926)
Δ_J [kHz]	9.06798(130)	8.85039(102)	9.044329(149)	8.857445(163)
Δ_{JK} [kHz]	-22.4693(188)	-24.6939(148)	-24.39340(112)	-21.98161(150)
Δ_K [kHz]	344.9361(740)	319.4537(465)	345.39770(580)	319.42230(819)
δ_J [kHz]	1.746990(401)	1.744413(400)	1.7525550(620)	1.7310800(730)
δ_K [kHz]	-21.5555(324)	-22.7267(348)	-21.66980(509)	-24.92760(589)
Φ_J [Hz]	0.011881(402)	0.015017(359)	0.0066440(380)	0.0076700(490)
Φ_{JK} [Hz]	-0.2201(365)	-0.2526(395)	-0.08680(380)	-0.23170(390)
Φ_{KJ} [Hz]	-11.277(217)	-4.414(128)	-3.7541(126)	-4.2860(151)
Φ_K [Hz]	41.157(229)	-8.730(164)	16.0490(296)	11.6830(400)
ϕ_J [Hz]	0.005587(170)	0.006044(187)	0.0040331(177)	0.0046143(234)
ϕ_{JK} [Hz]	1.0996(216)	0.5179(211)	0.11165(215)	0.06231(261)
ϕ_K [Hz]	-10.07(129)	-15.62(124)	-6.557(126)	-7.667(136)
L_{JK} [mHz]		0.31084(934)		
L_{JK} [mHz]	29.891(304)			
L_{JKK} [mHz]	-87.747(430)	41.097(176)		2.3602(262)
L_K [mHz]			-4.5050(380)	-4.4020(550)
l_{JKK} [mHz]		9.870(355)		
l_K [mHz]	573.50(541)			
Tunneling parameters				
ϵ_{10} [MHz]	79.9806(175)	78.3845(131)	79.93240(237)	78.24235(317)
$[A - ((C+B)/2)]_{10}$ [kHz]	-58.248(657)	-50.449(592)	67.005(130)	21.630(152)
$[(B+C)/2]_{10}$ [kHz]	14.882(312)	6.608(322)	-107.9303(270)	-65.4958(310)
$[(B-C)/4]_{10}$ [kHz]	2.695(174)	0.609(182)	-37.8552(157)	-54.1360(185)
$[\Delta_J]_{10}$ [Hz]	-7.659(160)	-2.550(168)	-27.9807(260)	-25.1143(317)
$[\Delta_{JK}]_{10}$ [Hz]	43.051(774)	13.352(837)	62.588(270)	115.325(232)
$[\Delta_K]_{10}$ [Hz]		44.55(281)	-110.1(10)	-292.9(14)
$[\delta_J]_{10}$ [Hz]	-2.512(120)	-1.783(123)	-17.8035(217)	-17.1305(235)
$[\delta_K]_{10}$ [Hz]	-167.73(146)	17.042(734)	133.700(332)	-96.547(345)
$[\Phi_J]_{10}$ [mHz]			-2.6030(127)	-2.2685(115)
$[\Phi_{JK}]_{10}$ [mHz]			-31.935(160)	
$[\Phi_{KJ}]_{10}$ [mHz]			374.275(825)	124.6(11)
$[\Phi_K]_{10}$ [mHz]			-515.0(22)	-691.3(43)
$[\phi_J]_{10}$ [mHz]			-3.12275(925)	-2.92000(849)
$[\phi_{JK}]_{10}$ [mHz]	68.236(806)		81.462(165)	-55.515(169)
$[(B-C)/4]_{20}$ [kHz]			-1.0790(46)	-0.4174(59)
$[\Delta_J]_{20}$ [mHz]			2.2273(46)	2.5192(60)
$[\Delta_{JK}]_{20}$ [mHz]			-14.912(36)	-23.108(70)
$[\Delta_K]_{20}$ [mHz]				31.72(24)
$[\delta_J]_{20}$ [mHz]			-0.7794(41)	-1.4436(49)
$[\delta_K]_{20}$ [mHz]			17.437(36)	20.332(41)
Interaction parameters				
G_c [MHz]			3493.10(246)	
F_{ab} [MHz]			38.587(51)	
$[G_c]_{10}$ [MHz]			-28.5936(263)	
$[F_{ab}]_{10}$ [MHz]			-1.05474(100)	

Table 4.5: Partition functions for DME calculated for selected temperatures based on SPFIT. In the last column the partition function including all vibrational states with $E_{vib} < 500 \text{ cm}^{-1}$ is tabulated. Partition functions for states, which are not explicitly listed, are interpolated from the ground state analysis.

Temperature	Q			
	(00)	(10) & (01)	$(qq')^a$ & (COC)	Sum ^b
300.000	477361.6315	334115.8717	248676.0070	1060153.5100
225.000	309935.7393	153089.9117	82230.8604	545256.5114
150.000	168667.8172	41640.5006	11681.8816	221990.1994
75.000	59655.9782	1890.0689	76.6595	61604.1674
37.500	21125.0901	12.2345	0.0105	21137.3351
18.750	7495.6992	0.0018	0.0000	7495.7010
9.375	2669.7988	0.0000	0.0000	2669.7988

^a $q + q' = 2$

^bAll vibrational states with $E_{vib} < 500 \text{ cm}^{-1}$ are considered.

4.4 Astronomical Identifications

Based on the derived parameter sets, frequency predictions have been calculated and used to tentatively assign a number of lines with unknown carrier in astronomical line surveys of the hot core star forming regions Orion KL, Sagittarius B2, and G327.3-06. The analysis of the astronomical spectra is based on a local thermal equilibrium approximation (LTE). The partition functions used in the model are tabulated in Tab. 4.5, and were derived from the analysis based on SPFIT. They have been calculated for selected temperatures chosen by the astrophysical needs. At temperatures exceeding 150 K, even energetically higher vibrational states are populated. Therefore, contributions from vibrational states such as the COC-bending mode as well as higher torsional states, are taken into account. Their partition functions have been obtained by interpolation using the spectroscopic parameters of the vibrational ground state, and the vibrational energy difference.

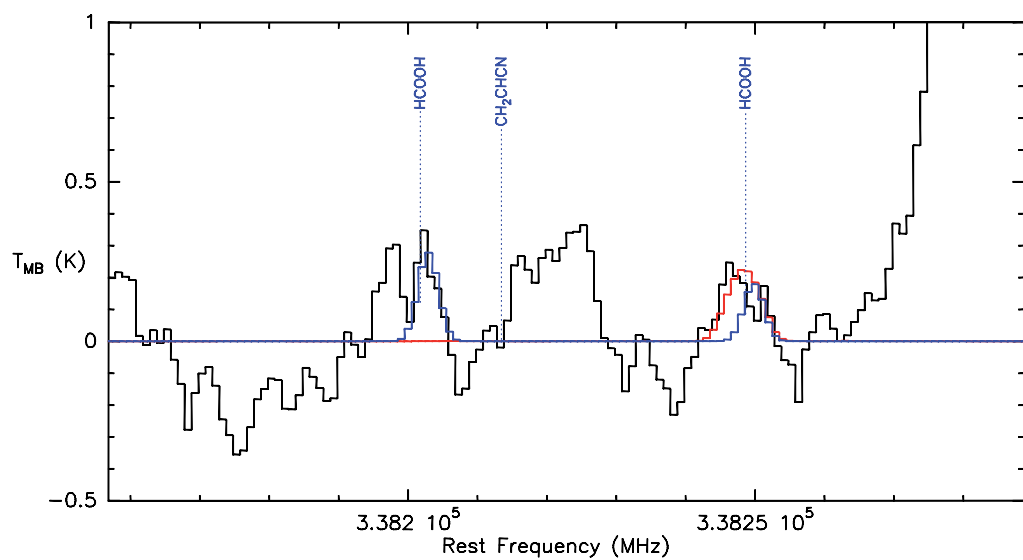
No obvious discrepancies have been detected in these astronomical surveys. The Orion KL observation was carried out by Schilke *et al.* at the Caltech Submillimeter Observatory (CSO) [1]. In their work, they assigned 25 spectral features to 82 ground state transitions of DME and determined a column density of $N = (1.8 \pm 0.2) \cdot 10^{16} \text{ cm}^{-2}$, and a temperature of $89 \pm 5 \text{ K}$. Higher temperatures and densities are obtained for the excited torsional states in this spectrum [31]. Two of the assignments are shown exemplary in Fig. 4.5. In the line survey of Sagittarius *B2(N)* recorded by A. Belloche at 3 mm wavelength with the IRAM 30 m telescope [32], several spectral features can be explained by rotational transitions within the excited states of DME. In the analysis, which is currently carried out by A. Belloche, transitions within the ground state are unambiguously assigned and pinpoint to a rotational temperature of 130 K, which has been used to model the rota-

tional transitions within the excited states [33]. As most of the transitions are blended, and the line intensities are just slightly above the detection limit unambiguous identification is currently not granted and requires a complete modeling, which is currently still being worked out. Nevertheless, the number of spectral features strongly indicate the presence of these transitions in the spectra and no transitions are missing. Despite the weakness of these transitions in this survey, the analysis of these transitions may provide useful insights into the infrared radiation field within the observed object and might help to understand part of the line confusion at the detection limit. S. Jørgensen-Bisschop recorded a line survey of the hot-core position in the southern molecular cloud G 327.3-06 with the APEX telescope [34], which is a high-mass star forming region at a distance of 2.9 kpc [35]. Spectra of the hot core region, which has about 500 solar masses, have been observed within the frequency bands 213 – 267 GHz, 270 – 315 GHz, and 335 – 362 GHz. Due to its velocity structure, the molecular lines are quite narrow (10 MHz) compared to the other sources, and thus, spectral features are better resolved. In the whole line survey more than 50 transitions within the excited states (10) and (01) have been clearly detected. Two examples are shown in Fig. 4.6. In total, approximately 300 transitions appear in the survey, of which most are blended with other molecular lines. The rotational temperature, which has been determined in the model for transitions within the excited states, is 150 K and exceeds the temperature determined for the ground state transitions (100 K). A complete analysis of the survey is currently worked out by S. Jørgensen-Bisschop.

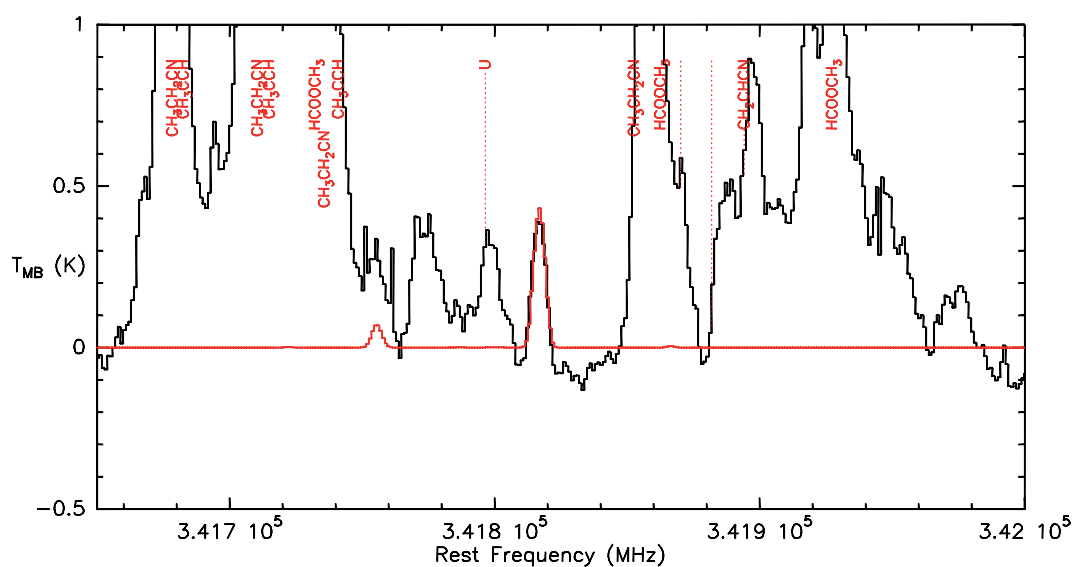
4.5 Torsional Potential Function

The use of the effective Hamiltonian, discussed in Chp. 3, provides the possibility to derive the two-dimensional torsional potential function for the methyl internal rotors in DME. By determining the internal motion tunneling parameters $\epsilon_{q_1q_2}$, as done in Chps 4.2 and 4.3, the torsional potential function can be calculated separately, including the experimentally achieved IR and Raman data of the torsional modes. The calculation, which will be discussed in the following, has the advantage that tunneling parameters, derived from the analysis of the pure rotational spectra, can be included as well as available frequencies from Raman and far-infrared spectra without being burdened by the complex rotational spectra. In the absence of angular momentum the Hamiltonian of the coupled internal rotations H_I (Eq. 3.24) reduces to

$$H_I(J=0) = \mathbf{p}_1 F \mathbf{p}_1 + \mathbf{p}_2 F \mathbf{p}_2 + \mathbf{p}_1 F' \mathbf{p}_2 + \mathbf{p}_2 F' \mathbf{p}_1 + V(\tau_1, \tau_2) \quad (4.3)$$

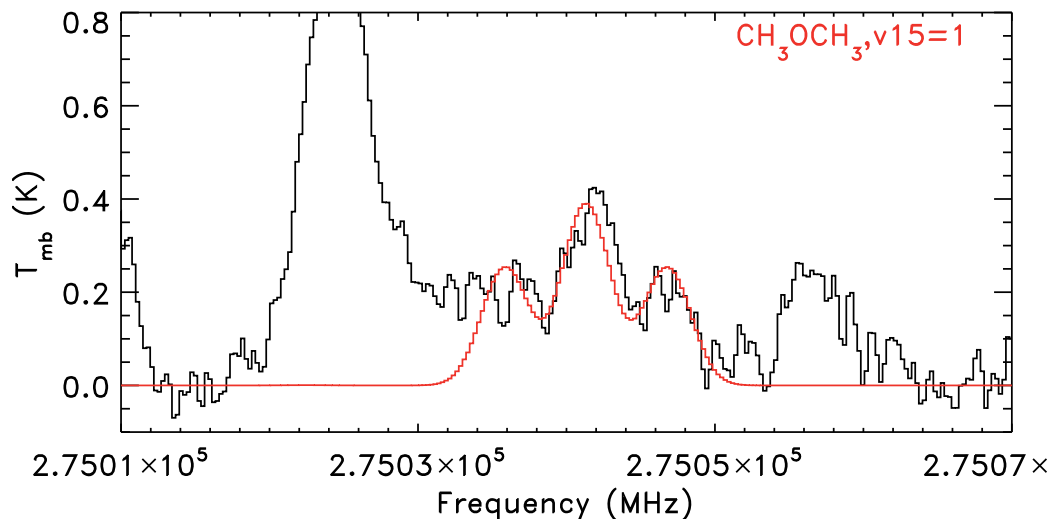


(a) Tentative detection of the $J_{K_a, K_c} = 19_{1,18} - 18_{2,17}$.

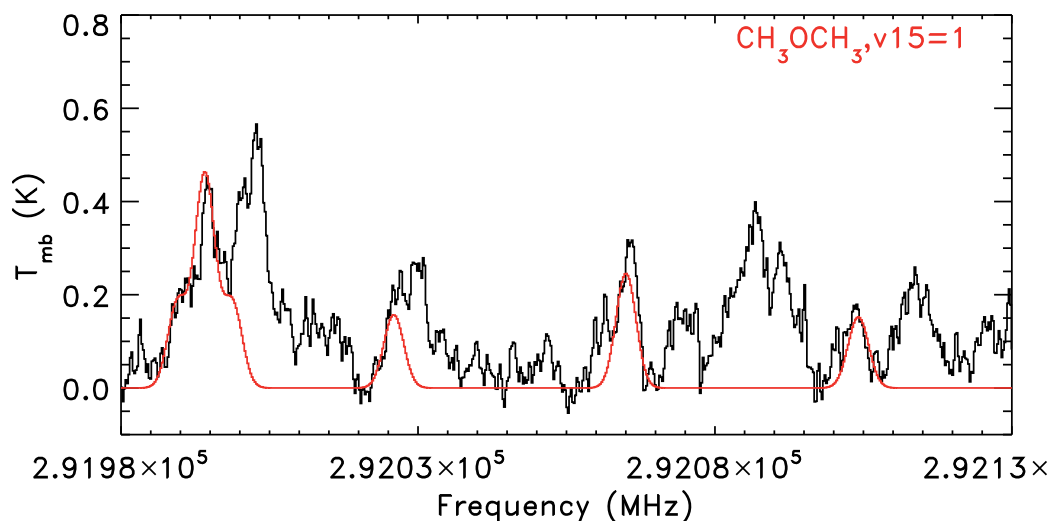


(b) Tentative detection of the $J_{K_a, K_c} = 19_{0,19} - 18_{1,18}$.

Figure 4.5: Tentative detections of transitions within the (10)-excited state of dimethyl ether in Orion KL plotted in red color. The transition $J_{K_a, K_c} = 19_{1,18} - 18_{2,17}$ is strongly blend by a HCOOH transition plotted in blue color.



(a) Detection of the transition $J_{K_a, K_c} = 15_{1,15} - 14_{0,14}$.



(b) Detection of the transitions $J_{K_a, K_c} = 16_{1,16} - 15_{0,15}$ and $J_{K_a, K_c} = 13_{2,12} - 12_{1,11}$.

Figure 4.6: Detail of the line survey of G 327.3-06 carried out with the APEX telescope. The observed spectrum is shown in black color, whereas the modeled spectrum of DME in its torsional state (01) is shown in red.

with

$$\begin{aligned}
V(\tau_1, \tau_2) &= V_0 + \frac{1}{2} [V_3(2 - \cos 3\tau_1 - \cos 3\tau_2) \\
&\quad + V_6(2 - \cos 6\tau_1 - \cos 6\tau_2) \\
&\quad + V_{33}(\cos 3\tau_1 \cos 3\tau_2 - 1) \\
&\quad + V'_{33}(\sin 3\tau_1 \sin 3\tau_2)] \\
&= V_0 + \frac{1}{2} [V_3^{eff}(2 - \cos 3\tau_1 - \cos 3\tau_2) \\
&\quad + V_6(2 - \cos 6\tau_1 - \cos 6\tau_2) \\
&\quad + V_{33}(1 - \cos 3\tau_1)(1 - \cos 3\tau_2) \\
&\quad + V'_{33}(\sin 3\tau_1 \sin 3\tau_2)]
\end{aligned} \tag{4.4}$$

The first form is rewritten in order to obtain the effective barrier height $V_3^{eff} = V_3 - V_{33}$.

A computer program has been developed in the course of this work to model the experimental data. The matrix elements are set up in the basis of free rotor functions, according to Eq. 3.25. The dimension of the matrix is 1849, and all basis functions with $|j_n| < 22$, $n = 1, 2$ are included. The energies of the torsional modes are obtained by diagonalization. The calculation is based on a least-squares fit, which has adjusted the parameters F , F' , V_3 , V_6 , V_{33} , and V'_{33} to fit the IR and Raman transition frequencies $E_{v'\sigma_1\sigma_2} - E_{v\sigma_1\sigma_2}$ as well as the energy differences between the torsional substates $\Delta_{v\sigma_1\sigma_2} = E_{v\sigma_1\sigma_2} - E_{v00}$. The latter are obtained from the internal motion tunneling parameters $\epsilon_{q_1q_2}$ using Eq. 3.53:

$$\begin{aligned}
\Delta_{v01} &= E_{v01} - E_{v00} = -3(\epsilon_{v10} + \epsilon_{v20}) - 3\epsilon_{v11} - 3\epsilon_{v1-1} \\
\Delta_{v11} &= E_{v11} - E_{v00} = -6(\epsilon_{v10} + \epsilon_{v20}) - 3\epsilon_{v11} \\
\Delta_{v12} &= E_{v12} - E_{v00} = -6(\epsilon_{v10} + \epsilon_{v20}) - 3\epsilon_{v1-1}
\end{aligned} \tag{4.5}$$

All experimental frequencies and energy differences are weighted by $1/\sigma^2$ where σ is the experimental error.

The experimental dataset used in the fit is shown in Tab. 4.6. The values Δ_{00} , Δ_{10} , Δ_{01} , and $E_{01} - E_{10}$ have been taken from the experimental part of this thesis. The remaining differences between torsional substates have been calculated based on the data derived by Groner *et al.* [12], whereas all infrared and Raman transitions are taken from an earlier work of Groner *et al.* [15].

As Fermi resonances are observed between the torsional states (02), (20) and the ($v_7 = 1$)-state (COC bend), located at 412 cm^{-1} , two distinct fits have been performed. In the calculation denoted as Fit No.1, all infrared and Raman transitions except $E_{01} - E_{00}$, $E_{01} - E_{00}$, and $E_{11} - E_{10}$ are excluded, because they are probably affected by Fermi resonances with the COC bending mode and its overtones. Fit No.2 includes all experimental data which is listed in Tab. 4.6.

Table 4.6: Dataset used in the potential function least-squares fit for DME. Observed and calculated energy differences Δ_v (in MHz) together with observed and calculated wavenumbers ΔE (in cm^{-1}) are shown with their estimated errors and residuals.

	$\sigma\sigma'$	Observed	Est. error	Calculated	Obs.-Calc.	Calculated	Obs.-Calc.
Δ_{00}	(01)	9.1330	0.0032	9.1326	0.0004	9.1357	-0.0026
Δ_{00}	(11)	18.2660	0.0065	18.2650	0.0010	18.2711	-0.0051
Δ_{00}	(12)	18.2660	0.0065	18.2652	0.0009	18.2713	-0.0052
Δ_{10}	(01)	-240.243	0.048	-240.290	0.047	-240.252	-0.008
Δ_{10}	(11)	-480.487	0.097	-480.492	0.006	-480.414	-0.072
Δ_{10}	(12)	-480.487	0.097	-480.488	0.001	-480.410	-0.076
Δ_{01}	(01)	-234.718	0.054	-234.673	-0.045	-234.660	-0.058
Δ_{01}	(11)	-469.435	0.108	-469.411	-0.024	-469.390	-0.045
Δ_{01}	(12)	-469.435	0.108	-469.436	-0.001	-469.412	-0.024
Δ_{20}	(01)	3317.3	6.5	3314.5	2.7	3341.1	-23.8
Δ_{20}	(11)	6676.4	12.6	6665.0	11.3	6720.0	-43.6
Δ_{20}	(12)	6688.5	12.4	6665.2	23.3	6720.1	-31.6
Δ_{11}	(01)	5412.2	45.2	5405.7	6.4	5385.9	26.3
Δ_{11}	(11)	10821.3	85.8	10782.0	39.3	10740.1	81.2
Δ_{11}	(12)	10835.9	84.3	10781.4	54.5	10739.6	96.3
Δ_{02}	(01)	1822.1	8.7	1852.3	-30.2	1852.7	-30.6
Δ_{02}	(11)	3619.7	17.1	3696.6	-76.9	3698.3	-78.5
Δ_{02}	(12)	3620.4	17.1	3699.0	-78.6	3700.2	-79.8
$E_{01} - E_{00}$	(01)	241.0	0.5	242.85	-1.85	245.38	-4.38
$E_{02} - E_{01}^a$	(01)	240.2	0.5*	237.43	2.77	241.02	-0.82
$E_{03} - E_{02}^a$	(01)	238.9	0.5*	229.88	9.02	234.25	4.65
$E_{12} - E_{11}^a$	(01)	224.8	0.5*	219.84	4.96	223.42	1.38
$E_{11} - E_{10}$	(01)	223.1	0.5	222.43	0.67	224.40	-1.30
$E_{21} - E_{20}^a$	(01)	200.7	0.5*	198.24	2.46	199.65	1.05
$E_{01} - E_{10}$	(01)	43.744	0.017	43.734	0.010	43.742	0.002
$E_{02} - E_{00}^a$	(01)	481.2	1.0*	480.28	0.92	486.40	-5.20
$E_{03} - E_{01}^a$	(01)	479.1	1.0*	467.30	11.80	475.27	3.83
$E_{20} - E_{00}^a$	(01)	395.5	1.0*	391.95	3.55	397.44	-1.94
$E_{30} - E_{10}^a$	(01)	385.0	1.0*	375.98	9.02	381.92	3.08

^a transition excluded in Fit No.1

Both fits describe the experimental dataset reasonably accurate. Especially the data derived in Chps 4.2 and 4.3, agree within their estimated uncertainties. Energy differences within the states (20), (11), and (02) are in a slightly lesser agreement, but the number of experimental transitions included in the analysis of their rotational states is quite limited (30 transitions) and thus, the systematic error due to the truncation of the model might be underestimated. As expected, infrared and Raman transitions show larger deviations from their calculated values. Terms which describe interactions with the COC bending mode are not included in the Hamiltonian and, thus, may explain these deviations. Also wrong assignments in the infrared and Raman spectra cannot be completely excluded. In the observed spectra recorded within the work of Groner *et al.* [15], a number of additional transitions have been observed which still remain unassigned. Indeed, the analysis revealed that probably the Raman transitions $E_{20} - E_{00}$ as well as $E_{30} - E_{10}$ might also be assigned to the observed transitions at 385.0 cm^{-1} and 363.0 cm^{-1} , respectively. The energy level of the COC bending mode is located between the torsional modes (20) and (02). As all three levels have the symmetry A_1 , (20) is expected to be shifted towards lower energies whereas (02) is expected to be shifted towards higher energies due to the Fermi resonance. Comparing the calculated frequencies for the transitions $E_{20} - E_{00}$ and $E_{30} - E_{10}$ obtained in both fits, the observed frequencies indeed seem to be shifted towards higher frequencies. But the calculated energy differences $E_{02} - E_{00}$ and $E_{03} - E_{01}$ are also found below their observed and assigned frequencies, in contrast to the expectation. This fact supports the assignment suggested above. As already discussed in [15], the combination energy levels of the coupled torsional modes and the bending mode is always located in between two energy levels of torsional modes having the same symmetry, except for the torsional modes (01), (10), and (11). Therefore, it can be assumed that these levels might also be perturbed. Such interactions may also affect the energy differences between different substates within one excited state and might contribute to the less accurate description of Δ_{20} , Δ_{11} , and Δ_{02} .

An overview of the derived parameter set is given in Tab. 4.7. The parameters derived by Groner *et al.* [15] and Niide *et al.* [14] are included for reasons of comparison. Both parameter sets are based either on the infrared and Raman transitions (Groner) or on the microwave data (Niide). The parameter set derived within this work slightly deviates from previously published ones. Most significant is the lower effective barrier height determined within this work and the notably larger value of F obtained by Fit No.2, whereas the value obtained in Fit No.1 closely correlates with the value obtained by Niide *et al.* Although the values of V_3 and V_{33} differ notably between both fits, the calculated effective barrier height remains within the errorbars. A similar behavior was obtained in the work of Groner[36] for acetone. By an analogous calculation, they determined an effective barrier height, which is also below the values determined by the use of either the infrared or the microwave data only. Although the observed data is in rela-

Table 4.7: Kinetic coefficients and potential parameters.

Parameter	Groner <i>et al.</i> [15]	Niide <i>et al.</i> [14]	Fit No.1	Fit No.2
F [GHz]	203.325391	204.93	205.640(290)	207.953(145)
F' [GHz]	-41.0427867	-41.25	-42.355(75)	-42.729(63)
V_3 [cm ⁻¹]	1215.28(1658)	925.59(350)	1053.01(490)	1095.97(356)
V_{33} [cm ⁻¹]	272.68(1823)		147.18(530)	181.85(433)
V'_{33} [cm ⁻¹]	21.64(463)	-43.5(18)	15.55(53)	18.63(43)
V_6 [cm ⁻¹]	-20.75(428)		0.067(23)	0.248(20)
V_3^{eff} [cm ⁻¹]	942.6(246)	925.59(350)	905.83(722)	914.12(560)

tively good agreement with the calculated one, the results demonstrate that a complete and accurate description of the experimental data can only be obtained if the Hamiltonian also includes terms describing the COC bending mode. Such a Hamiltonian has currently not yet been worked out, but may quantitatively describe the Fermi resonance and resolve the remaining residuals. Despite the discrepancies the applied procedure demonstrates that the inclusion of results obtained by rotational spectroscopy provides important insights and constraints to support the analysis of vibrational spectra of the torsional modes.

5

Conclusion

Spectral recordings have been carried out in the scope of this thesis, which cover a huge part of the pure rotational spectrum of DME and frequencies from 38 GHz up to almost 2.1 THz. In total, almost 15000 transitions have been assigned and added to the existing datasets. Although the dataset of rotational transitions within the vibrational ground state was already quite extensive, it has turned out that the additional measurements and assignments have been necessary to provide accurate frequency predictions for the whole THz range. The new dataset, which contains transitions involving energy levels up to $J = 70$ and $K = 30$, has been analyzed and fitted to an effective Hamiltonian to experimental uncertainty.

The present analysis provides accurate and considerably improved predictions for the ground state spectrum of DME up to 2.5 THz. Frequencies of strong transitions in the THz frequency region with K values larger than 10 are typically improved on the order of several MHz. For example, the transition $J_{Ka} = 14_{13} - 13_{12}$ at 995625 MHz is shifted by around 6 MHz compared to predictions based on [12]. The most intense transitions are found at 1 THz for rotational temperatures of 200 K, which is a typical temperature for molecules in hot cores. Rotational temperatures of 89 K [1] and 360 K [2] have been reported for the vibrational ground state of DME in Orion KL.

For all transitions involving energy levels with $E \leq 1500 \text{ cm}^{-1}$ and quantum numbers up to $J = 65$, $K = 30$, the accuracy is expected to be better than 1 MHz. For astronomical applications for which 1 MHz accuracy is usually sufficient, these predictions provide a reliable basis even for future observations with the new generation of telescopes. In particular, the quality of predictions suffices to eliminate ground state transitions of DME as a source of line confusion. Above 1 THz, the data fulfills the requirements needed in order to analyze future spectra recorded with the Herschel Space Observatory. The HIFI receiver aboard Herschel will give access to frequencies up to 1.91 THz with a spectral resolution better than 1.1 MHz. Also the demand for precise frequency predictions of weaker transitions - due to the improvement in sensitivity and spatial resolution granted by the Atacama

Large Millimeter/submillimeter Array (ALMA) - should be satisfied by the data of the present work.

For the first time, reliable frequency predictions for the rotational spectra within excited torsional states have been calculated. Almost 10000 experimental transition frequencies have been assigned and constitute the foundation on which these predictions are based on. Although the limits of the applied theoretical models become apparent in the analysis of the excited states and the dataset could not be reproduced within experimental uncertainty, the derived frequency predictions are sufficient for most astronomical purposes. Especially transitions with quantum numbers $J \leq 30$ and $K \leq 10$ should be predicted within 1 – 2 MHz.

The analysis of the torsional excited states has pointed out the applicability and limits of the currently available fitting routines for molecules with several internal rotors. Whereas the tunneling splitting within the ground vibrational state has been modeled without mentionable difficulty, deviations become obvious within the excited states, where the size of the splitting is around 30 times larger compared to the ground state. The simplified model used in the SPFIT routine runs into difficulties in particular for higher values of J . The description is still reasonable in the ERHAM routine, although small inaccuracies occur as well.

Furthermore, the torsional states and their overtones are found at low energies ($E_{10} \approx 200 \text{ cm}^{-1}$ and $E_{01} \approx 240 \text{ cm}^{-1}$), which increases the probability of interactions with other torsional states or low lying bending modes. Thus, second order Coriolis interaction between rotational levels of the torsional states (10) and (01) in combination with the internal tunneling splitting complicate the spectrum considerably and still present a challenge for the line assignment and the computer models. The SPFIT routine has shown to treat the interactions discussed in the present thesis sufficiently well, and has allowed to accurately determine the energy difference of both states. Nevertheless, these perturbations as well as the splitting could be qualitatively and quantitatively well described by the model although some minor problems persist.

As both applied fitting routines have significant drawbacks, the experimental dataset for the excited states could not be fitted to experimental uncertainty. Both routines complement each other, ERHAM provides a more accurate treatment of the tunneling splitting, whereas SPFIT allows to include the perturbation. As both routines are currently extended in order to overcome these drawbacks, it can be expected that the precision of the analysis can be significantly improved in the near future. Anyhow, in most cases the derived accuracy of predicted frequencies is sufficient for the analysis of astronomical observations, which has been demonstrated by the detection of transitions within the excited states in the three astronomical line surveys. The analysis of these spectra usually requires accuracies in the order of 1 MHz. Transitions which are intense enough to be observable in star-forming regions, satisfy this criteria with very few exceptions.

Tables of measured frequencies are given in Tabs. B.1 and B.2 of the appendix of this work¹. They will also be made available through the Cologne Database for Molecular Spectroscopy (CDMS: <http://www.cdms.de>) [37, 38] as well as through the JPL database (<http://spec.jpl.nasa.gov>) [39] along with the predicted frequencies. The parameter files for both fitting routines (ERHAM and SPFIT) can be found in the example section of these databases.

¹The appendix B can only be obtained in electronic form via http://www.cuvillier-verlag.de/assets/mime/-UTQ3ZXHNcHnxcUdsDGJkfZ8gBeY7++wRdCJJoPYE8gvo8rw3/Appendix_B.pdf

Part II

High Resolution THz Spectrometers: Techniques and Perspectives

6

Introduction

The terahertz domain of the electromagnetic spectrum with frequencies between 0.5 and 5 THz is of great interest to astronomers and spectroscopists. Light hydrides possess their strongest absorption lines and larger molecules exhibit low lying bending vibrations in this frequency regime. Today, several efficient technical approaches are well established for high resolution spectroscopy in the THz region. Backward wave oscillators (i) are tunable and powerful monochromatic radiation sources, which have been phase locked for frequencies up to 1.26 THz [40]. With sideband techniques, even higher frequencies are attainable [41, 42] (ii), which are not easy to handle and laborious in most cases. Alternatively, tunable far IR laser systems [43, 44] (iii) achieve excellent spectra. However, the paucity of laser lines prevents the complete coverage of larger spectral ranges. Very promising THz sources are quantum cascade lasers for the THz regime (iv), whose development has made substantial progresses in the recent years. First devices have been successfully phase locked at frequencies around 1.5 THz [45] and, undoubtedly, they will play a dominant role as future powerful radiation sources. Currently their spectral coverage is still quite limited because their internal cavity allows only a narrow tuning range in the vicinity of the cavity modes. Beside the development of these high resolution sources, Fourier transform spectrometers (v) are also used to cover the complete THz spectral range, albeit with low resolution and limited sensitivity. Furthermore, the absolute accuracy of far-IR lasers and Fourier transform spectrometers strongly depends on the accuracy and the availability of calibration lines.

The most compact THz radiation sources are THz-frequency multipliers, based on harmonics generation due to the non-linearity of the current-voltage or capacitance voltage characteristic of a fast electronic device. One well known frequency multiplier is the Schottky barrier diode (vi), which many groups successfully apply in spectroscopy and astronomy. For references see, e.g., [46, 47]. In most cases, the input frequency is supplied by a powerful cw Gunn-Oscillator or a solid state FET amplifier. These devices are mainly operated as frequency doublers and triplers. Higher order harmonics are available, too, however, only with considerably lower power. As a

consequence Schottky diodes require relatively high input frequencies with considerable input powers in the range of Milliwatts to reach the THz-range. Therefore it is necessary to cascade several multipliers. Good examples for such devices are multiplier chains especially designed for the 1.5 THz regime [48] and 1.9 THz regime [49]. However, their employment in the field of spectroscopy is limited since they are optimized for a certain restricted frequency window.

The advent of molecular beam epitaxy has enabled the development of a new type of multiplier, the superlattice (SL) multiplier [50]. A SL-multiplier consists of a periodic arrangement of thin epitaxial layers. Due to the periodicity of the structure, the electron energy is restricted to minibands with a specific miniband gap. The transport of miniband electrons leads to a negative differential resistance. Above a threshold value, the current-voltage characteristic of SL devices is highly non-linear and antisymmetric, making it suitable for high-frequency multiplication. This behavior has first been proposed by Esaki and Tsu theoretically [51], and later on demonstrated by several groups [52, 53]. Enhanced characteristics due to intense theoretical and experimental studies [51, 54, 55, 56, 57, 58] make the SL an attractive alternative to Schottky diodes.

Spectrometers based on commercial synthesizers, BWOs, Schottky diodes and also sideband techniques are well established in the Cologne laboratories and have been applied to investigate the spectra of a variety of molecules in the frequency range up to almost 2 THz. As the SL devices with the above described properties promised to be a perfect complement to the available spectrometers, one objective of the present thesis was the investigation and application of these devices to the established spectrometer setups. In this technical part of the thesis, this first successful application of SL devices to high resolution THz spectroscopy will be presented and discussed in detail. This part begins with an overview of the well established spectrometer setups restricted to those which were involved in the measurements presented in part I. Chp. 8 will show that the SL spectrometer setups provide almost full access and full coverage of the frequency region up to 3 THz. The SLs serve as reasonably intense, widely tunable, high-resolution THz sources, which can be operated at moderate input frequencies and with high frequency multiplication factors.

The end of this technical part addresses the question of detection techniques. Commonly, liquid helium hot electron bolometers are applied as sensitive detectors in conventional absorption spectrometers. They provide sensitivity over a broad spectral frequency range and satisfy most needs, even if monochromatic radiation sources with low output powers are applied. Nevertheless, heterodyne detection techniques, which are known to be extremely sensitive and which have been applied in astronomical receivers for decades, might provide several new features if also applied in laboratory spectroscopy. In this field, it already became a key technique in Fourier Transform Microwave Spectrometers [59, 60, 61, 62, 63, 64], which have been invented by Balle *et al.* in 1981 [65]. These extremely sensitive spectrometers are

nowadays widespread in the low frequency domain. Although frequencies up to 140 GHz have already been achieved [66], most of them are operated at frequencies below 40 GHz.

The second objective therefore concerns the exploration of heterodyne detectors for laboratory THz spectroscopy. The aim of these feasibility studies, discussed in Chp. 9, is to explore the opportunities provided by this extremely sensitive and extremely fast detection method for laboratory spectroscopy, not only but also regarding the application of SL devices. Analogous to their application in astronomy, it has been possible to record emission spectra of D₂O and methanol using heterodyne detectors built in Cologne for their application at different telescope sites. In combination with IF spectrometers, spectra with more than 1 GHz bandwidth are resolved in different frequency channels and recorded simultaneously. On the other hand, extremely narrow, but tunable detection bandwidths have been realized using heterodyne detection based on SL as mixer devices. These very compact setups provide reasonable sensitivity even at room temperature and might be an interesting alternative - especially concerning the study of fast processes.

7

Cologne Spectrometers

In Cologne, the frequency coverage is achieved by several spectrometer setups. The low frequency region (<70 GHz) is nowadays covered by commercially available microwave synthesizers based on field-effect transistors. Their frequency range can be extended by the use of frequency multiplier devices up to at least 125 GHz, or more, if multiplier chains are applied. Since more than a decade, frequencies up to at least 1000 GHz are obtained by the application of several powerful backward wave oscillators. Even higher frequencies up to 3.1 THz can be accessed with the new superlattice spectrometer, which has been assembled in the scope of this work, and which is described in detail in Chp.8.

7.1 Synthesizer and Multiplier Chains

The solid state spectrometers are conventional long-path absorption spectrometers designed for millimeter wavelengths [67]. The radiation is generated by a commercial synthesizer (50 GHz Agilent HP83650 or 70 GHz Agilent HP8257D) locked to a rubidium reference standard and is emitted via a horn antenna. Two Teflon lenses guide the beam through the 5 m long absorption cell and into another horn antenna connected to a standard Schottky diode, which acts as a continuum detector by rectifying the incoming radiation. The current response of the frequency modulated signal is detected by a lock-in amplifier. The spectrometer is fully operated via computer, which allows to record broad band spectra of stable molecules over long timescales under stable conditions. The frequency range of this setup can be extended by the use of frequency multipliers or frequency multiplier chains. To access frequencies between 80 and 125 GHz, the radiation is amplified by a Centellax TA2U50HA device, which finally drives a Virginia Diodes Inc. type WR9.3x3 frequency tripler. Its successful operation was recently demonstrated by recordings of the HSSOH spectrum in the work of M. Koerber *et al.* [68]. Both configurations, with and without tripler have

been applied to record parts of the DME spectrum described in Part I. If multiplier chains are applied, the synthesizer is operated at frequencies below 20 GHz. Subsequently, the radiation is amplified and doubled (or tripled) in frequency by an active amplifier device, before it is fed into a passive high frequency multiplier or a cascading chain of multipliers. At frequencies above 80 GHz InSb hot electron bolometers are sometimes used for detection. These liquid helium cooled detectors provide a slightly better sensitivity in the 1-3 mm wave regime and are detectors of choice at sub-mm wavelengths.

7.2 BWO-THz-Spectrometer

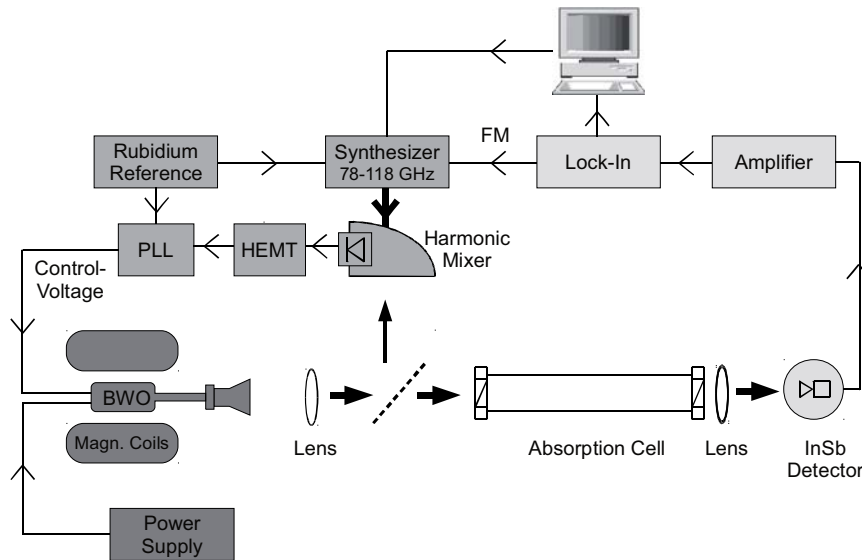


Figure 7.1: Setup of the THz - Spectrometer. The radiation is generated by the phase-stabilized BWO, guided through the absorption cell and detected with an InSb hot electron bolometer. 2F detection technique is used to increase the signal to noise ratio.

The Backward Wave Oscillator (BWO)-THz-Spectrometer (Fig. 7.1) has been successfully operated in Cologne for more than a decade for the recording of absorption spectra with high sensitivity in the frequency range up to 1 THz [69, 70]. The spectral coverage is provided by several backward wave oscillators offering tuning ranges of 20 % around their center frequency and output powers in the order of several up to several tenth of mW. Despite tremendous technological progress in the development of multiplier chains in the past years, such output powers are still barely achieved in this frequency range by harmonic generation. In this section the main elements and the principles of operation will be discussed.

Backward wave oscillators are electron tubes, generating sub-mm-wave (130 – 1200 GHz) radiation with powers in the order of several milliwatts over their entire tuning range, which is around 20% of the center frequency. The principle of such BWO's is depicted in Fig. 7.2. An electron beam (1) is emitted from a filament (2) and accelerated by a high voltage in the order of 2000–6000 V between the cathode (3) and the anode (5). A strong axial magnetic field collimates and focuses the beam through a periodic structure (4) within a waveguide situated between cathode and anode. The electromagnetic wave (7) is coupled out at the forward end of the waveguide into an overmoded waveguide (8). A horn antenna is usually used to transfer the waveguide modes into free space modes. The frequency is adjusted by tuning the acceleration voltage. Since free running frequency fluctuations and drifts of the order of several MHz within 1 minute are larger than the typical Doppler width of the spectral lines, active frequency stabilization is essential for the operation of BWOs. For this purpose, the spectrometer contains a phase lock loop unit. A small fraction of the radiation generated by the BWO is reflected by a beam splitter (<10 %) in the horn of a harmonic mixer. In the harmonic mixer this signal is downconverted by an appropriate harmonic of a synthesizer to obtain a difference frequency of 350 MHz. By comparing the phases of this difference signal with the 35th harmonic of a 10 MHz rubidium reference signal a correction voltage is obtained and fed to the anode of the BWO to adjust the frequency of the BWO. The frequency stability of the BWO radiation achieved in this setup is $\Delta\nu/\nu < 10^{-11}$.

Commercial InSb liquid helium cooled hot electron bolometers (QMC Instruments, Cardiff) are used as detectors. The sensitivity provided by these broad band detectors is in the range of 10^{-12} W/ $\sqrt{\text{Hz}}$. In order to increase the detectable frequency region these devices are tuned with an inhomogeneous magnetic field. This allows sensitive detection from 100 GHz up to 2.3 THz. Due to short relaxation times (1 μs) fast detection is feasible and allows modulation frequencies up to 1 MHz. The spectra are typically recorded by the use of $2f$ frequency modulation with modulation frequencies of several ten kHz and amplitudes of 0.1 – 1 MHz (one third of the line width). The absorption cells consists of pyrex glas tubes sealed by HDPE (high density polyethylene) windows. HDPE has a reasonably low absorption coefficient in the THz frequency domain and is, therefore, also used for the hyperbolic lenses to guide the radiation through the absorption cell and into the detector. Static Pressures in the absorption cell are typically in the range between 1-100 μbar . Such pressures are achieved by a rotary vane pump followed by a turbo molecular pump.

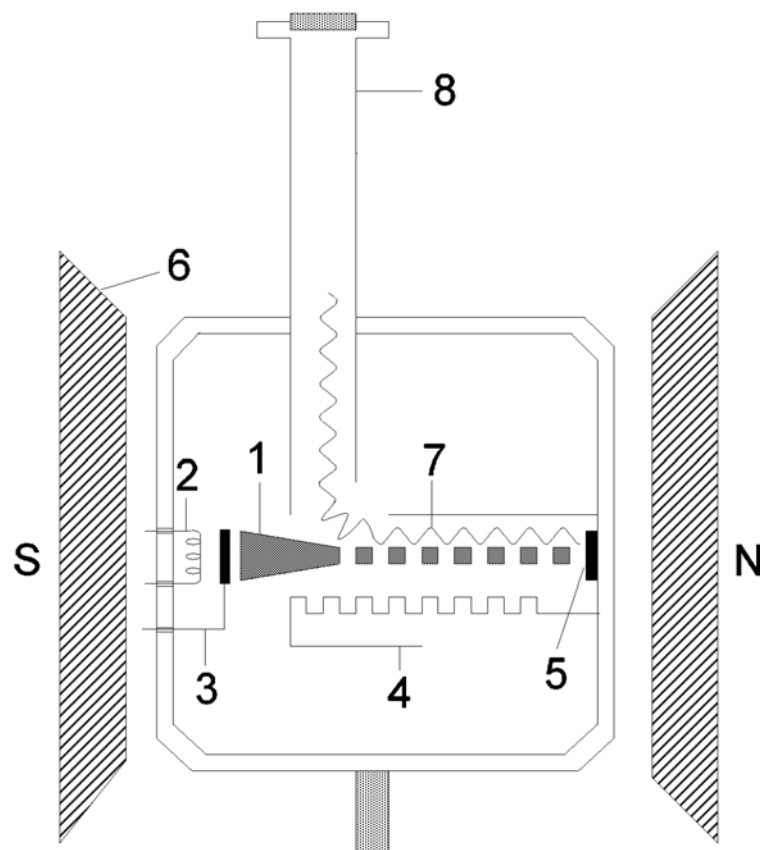


Figure 7.2: Schematic of the BWO. An electron beam (1) is emitted from the filament (2) and accelerated by a high voltage between the cathode (3) and the anode (5). A strong axial magnetic field of a magnet (6) collimates and focuses the beam through a periodic structure (4). The electromagnetic wave (7) is coupled out at the forward end of the waveguide into an overmoded waveguide (8).

8

Superlattice Spectrometer

8.1 The Superlattice Device

The SL devices used in the current multiplier setups are made up of 18 monolayers GaAs and 4 monolayers AlAs with a total number of 18 periods (length 112 nm) [71]. For testing purposes the current voltage characteristics of the device has been measured using a commercial curve tracer. The result of this I/V curve is shown in Fig. 8.1. For small electric fields, corresponding to small voltages applied to the SL, the current, corresponding to the drift velocity of the electrons along the SL axis, shows a resistive behavior. Above a certain critical field strength, i.e. a critical voltage of $U_c \sim 0.5$ V, when the current exceeds a value of ~ 3.5 mA the SL device exhibits a negative differential conductance. This strong non-linearity gives rise to the formation of higher order harmonics when instead of a DC field a high frequency field of appropriate strength, i.e. exceeding the critical value, is applied. The I/V curve is antisymmetric and therefore only odd numbered harmonics shall be generated in such a device, if no bias is applied. The curve shown in Fig. 8.1 is in good agreement with the results of previous studies [72] and with theoretical predictions [51, 73]. The hysteresis and jumps, which occur above the critical voltage are assumed to originate from domain formation processes.

The design and understanding of SL devices is an active field of research [53, 74, 75, 76, 77, 78, 73, 71, 72, 79]. According to recent work by Scheurer *et al.* frequency multiplication by propagating dipole domains is feasible in a frequency range $\omega\tau < 1$, where $\tau (\simeq 10^{-13}\text{s})$ is the intraminiband relaxation time, that is at least, up to frequencies of about $\omega \sim 1$ THz [80]. The application of SLs as frequency multipliers in high resolution THz spectroscopy is therefore a very promising approach whose realization for the use as a source for molecular spectroscopy was one of the purposes of the presented thesis. Another interesting aspect of the SL device is that it is considerably more robust to electrostatic discharge than a Schottky diode since the induced current is limited above the critical voltage U_c as can be seen from Fig. 8.1.

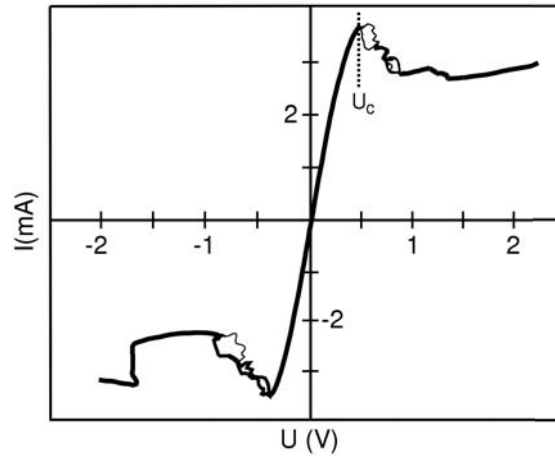


Figure 8.1: I/V-Curve of a SL device measured with a commercial curve tracer. For effective multiplication the voltage has to exceed the critical voltage U_c in order to reach the region of strongest non-linearity and domain formation.

8.2 Spectrometer Setup

In the present spectrometer setups two different SLs designed for input frequencies centered at 100 GHz (SL I) and 250 GHz (SL II) have been used. They have been assembled at the State University N. Novgorod (Russia) by D. G. Paveliev. The waveguides have been designed in inline configuration and manufactured in split block technique. The cut-off frequencies of the output waveguides are 250 GHz and 750 GHz, respectively. A feed horn is integrated in the SL I device, while a Pickett-Potter horn is flanged on the SL II. According to the I/V-curve shown in Fig. 8.1 the input power coupled into the SL has to exceed 1.75 mW ($0.5 \text{ V} \times 3.5 \text{ mA}$) in order to reach the region of strong non-linearity. The critical value of the field could be lowered when applying a bias current to the SL. However, this would destroy the antisymmetry of the current voltage behavior and lead to the generation of even numbered harmonics in addition to the odd numbered harmonics. In all experiments presented here only unbiased SLs were used in order to maximize the power fed into the odd numbered harmonics.

The SL multipliers have been used in combination with two continuously tunable backward wave oscillator (BWO) tubes (ISTOK, Moscow region, Russia) [81] as input radiation sources, delivering output powers of 10-60 milliwatts throughout the entire frequency range from 78 to 118 GHz for SL I and from 130 to 260 GHz for SL II. The BWOs are stabilized in frequency via a phase locked loop (PLL) w.r.t. a rubidium reference with a frequency accuracy $\Delta f/f = 10^{-11}$. For detection of SL output power below 2.33 THz a magnetically tuned InSb Hot Electron Bolometer ($\text{NEP} = 3.5 \text{ pW}/\sqrt{\text{Hz}}$) has been deployed, while a Ga doped Ge photoconductor with significantly higher sensitivity ($\text{NEP} = 0.6 \text{ pW}/\sqrt{\text{Hz}}$) has been used for higher frequencies. A sketch of the spectrometer setup is shown in Fig. 8.2. The main fraction of

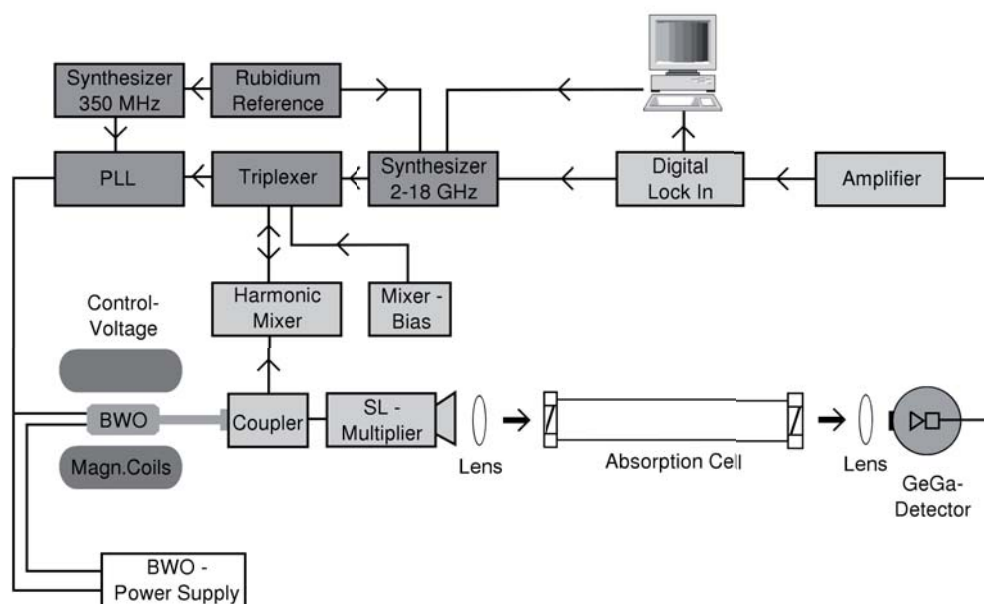


Figure 8.2: Setup of the THz-Spectrometer with superlattice multiplier.

the fundamental output radiation generated by the BWO is coupled into the SL multiplier and only a small fraction is used for the PLL circuitry. Two high density polyethylene lenses focus the harmonics generated in the SL through a 3.5 m long absorption cell into the detector. The detector signal is frequency selectively amplified, and demodulated by a lock-in amplifier. In all cases the $2f$ frequency modulation technique is used for recording spectra.

8.3 Spectra

Spectra have been recorded over the whole frequency range provided by the fundamental input radiation sources using harmonics up to the 11th and in some favorable cases up to the 13th. The measurements show that harmonics up to the 11th order can be used for spectroscopic purposes. As sample gases CO, methanol, dimethyl ether, deuterated ammonia, and deuterated water were introduced. These molecules exhibit rich spectra of strong rotational lines in the THz frequency region. Due to intensive previous spectroscopic investigations of these species our predictions were sufficiently good for line assignment. In some cases bandpass filters have been used to enhance spectral purity. The measurements shown in the following subsections shall demonstrate that (A) the SL operated sources are indeed producing higher order odd harmonics in sufficient supply for laboratory spectroscopy, (B) very high line accuracies can be achieved, (C) broad band scans are feasible and (D) overall very high frequencies up to 3.1 THz can be used for spectroscopy.

8.3.1 Output Intensities at Higher Harmonics

To roughly estimate the fraction of power in each harmonic, measurements on the rotational spectra of CO in the vibrational ground state have been performed. As a diatomic molecule CO has rotational transitions which are spaced by $2B \approx 115$ GHz. These transitions are very suitable, since 115 GHz is in the operational range of the BWO and for every harmonic generated by the SL a rotational transition of CO can be found. Consequently, the fundamental frequency has to be tuned only by a few MHz in order to measure several CO transitions using higher harmonics generated by SL I. The frequency and the line strength of CO transitions is very precisely known [82]. Line intensities have been determined as rectified voltage levels of a lock-in amplifier. To obtain a value for the SL output power at various harmonics the line strength variations due to the Boltzmann distribution of the rotational levels as well as detector sensitivity have been accounted for. The intensity ratios of transitions recorded with different harmonics generated with the SL have been used to calculate the attenuation between the harmonics.

$$a = 10 \log(U/U_0),$$

where U is the corrected voltage measured at the lock-in amplifier and U_0 is the corrected voltage measured for the 3rd harmonic.

The rotational transitions $J = 3 \leftarrow 2$, $J = 5 \leftarrow 4$, $J = 7 \leftarrow 6$, $J = 9 \leftarrow 8$, and $J = 11 \leftarrow 10$ of CO have been measured in the vibrational ground state at room temperature using the *3rd*, *5th*, *7th*, *9th*, and *11th* harmonic, respectively. All spectra have been recorded with 17 kHz modulation frequency, 320 ms integration time, and with 20 kHz steps at the fundamental frequency. The modulation depth of the fundamental BWO carrier signal was 150 kHz. Each spectrum was recorded in a single scan, except the ones recorded with the *9th* and the *11th* harmonic. In the latter cases 2 and 10 scans were added, respectively. The measured transitions are summarized in Tab. 8.1 together with their intensities, and the attenuation a . Fig. 8.3 illustrates the decrease of output power with increasing order of harmonics generation. The slope is in the order of 11.5 dB between two consecutive odd harmonics and 0.053 ± 0.004 dB/GHz. This is even better compared to Schottky diodes, which reach typical values of 0.08 dB/GHz [83]. Small deviations from the antisymmetry of the I/V-curve cause also even harmonics to be generated. The even harmonics are suppressed by a factor of roughly 200 for the *2nd* harmonic (see Fig. 8.4). The transition $J = 2 \leftarrow 1$ has been recorded using the *2nd* harmonic generated by SL I. The measured intensity is at the order of the *5th* harmonic. The *4th* harmonic was below the detection limit. The total output power of the SL was $P_{tot} = 200 \pm 50 \mu\text{W}$. This measurement was performed by using a calorimeter, which was directly connected to the output waveguide of the SL. The determination of the total output power allows to calculate the power of each harmonic using the attenuation a from Tab. 8.1,

$$P = P_0 \cdot 10^{-a/10}$$

Table 8.1: Intensities U (voltage at the lock-in amplifier) of the CO measurements recorded with the low frequency BWO in combination with the SL I multiplier. The intensities U are corrected values taking Boltzmann factors of line strengths and frequency dependence of the detector into account. a gives the attenuation relative to the third harmonic and P the resultant power in each harmonic.

n	J	Frequency [GHz]	Intensity U [V]	a [dB]	P [μ W]
3	3 \leftarrow 2	345.8	43.116	0 ^a	200
5	5 \leftarrow 4	576.3	0.773	17.5	3.5
7	7 \leftarrow 6	806.7	0.0492	29.4	0.23
9	9 \leftarrow 8	1037.0	0.004478	39.8	0.021
11	11 \leftarrow 10	1267.0	0.000498	49.4	0.0023

^aper def.

and $P_0 \simeq P_{tot}$, assuming that the total power is strongly dominated by the power in the third harmonic. The calculated values are shown in Tab. 8.1. At the 11th harmonic (~ 1.27 THz) 2 nW are still available which is sufficient for spectroscopic measurements of medium and strong transitions.

8.3.2 Accuracy in Frequency

Since rotational transition frequencies of CO are known within 500 Hz accuracy for frequencies below 800 GHz and 5 kHz for higher frequencies [82], CO is a very suitable probe for the verification of the frequency accuracy of the SL spectrometer. This reference data, based on a fit of Doppler and precise subdoppler measurements is given in Tab. 8.2 together with the CO transition frequencies measured in this work for comparison. Transition frequencies measured up to the 7th harmonic (806 GHz) of the SL match better than 3 kHz. The uncertainties in these measurements are dominated by the signal to noise ratio and baseline effects, which became disadvantageous at higher frequencies.

Table 8.2: The table shows center frequencies of the CO measurements recorded with the low frequency BWO in combination with the SL I multiplier and the precise frequencies measured by Winnewisser *et al.* [82] for comparison.

n	J	Frequency [MHz]		Residual [kHz]
		This work	Winnewisser <i>et al.</i> [82]	
3	3 \leftarrow 2	345795.987(10)	345795.9899(5)	-2.9
5	5 \leftarrow 4	576267.929(20)	576267.9305(5)	-1.5
7	7 \leftarrow 6	806651.805(20)	806651.806(5)	-1.0
9	9 \leftarrow 8	1036912.358(50)	1036912.393(5)	-35
11	11 \leftarrow 10	1267014.434(50)	1267014.486(5)	-52

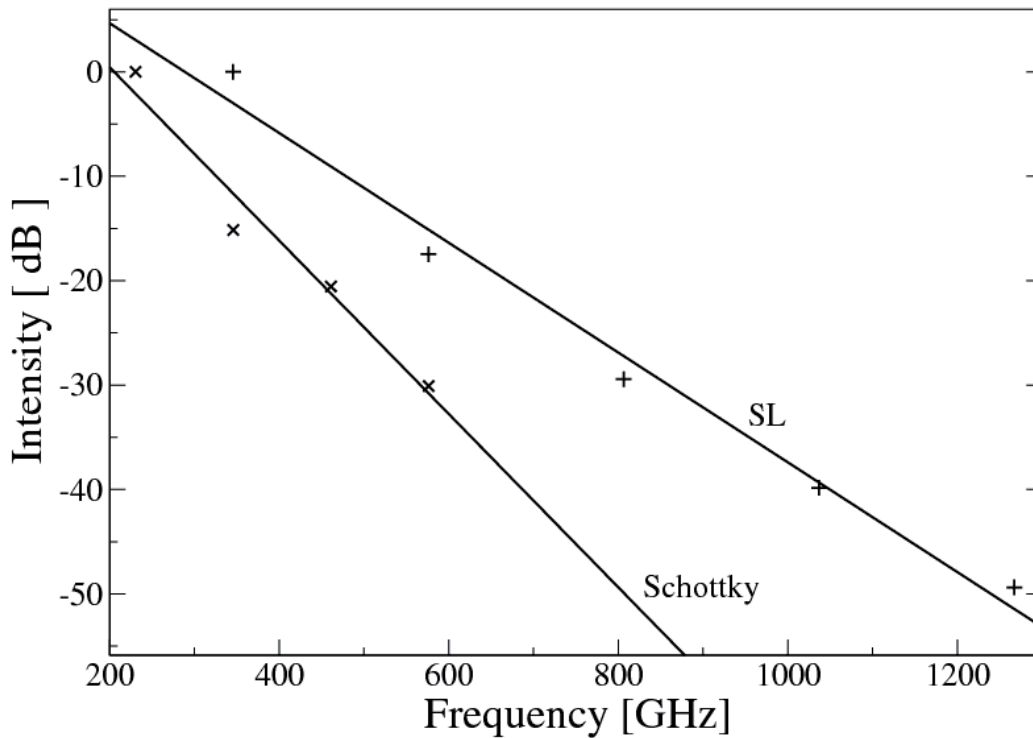


Figure 8.3: Relative intensities of rotational transitions in CO in dependence of the harmonic associated with this measurement. All measurements were performed with the low frequency BWO. For comparison, measurements performed by Maiwald *et al.* with a Schottky multiplier are also shown.

8.3.3 Broadband Scan of Methanol

In order to study the broadband tunability of the SL device a large number of methanol and dimethyl ether spectra were recorded in the frequency range from 170 to 1200 GHz by using harmonics from the 3rd to 13th generated by SL I. In particular, scans over a broad frequency range of several GHz were of interest. These scans are feasible with the low frequency BWO setup, because this spectrometer setup is fully controllable via a PC. Dichroic plates were used as bandpass filters. As an example, a 1.4 GHz broad scan with line precisions of several kHz is shown in Fig. 8.5. The scan was recorded with the seventh harmonic of SL I using 17 kHz as modulation frequency, 100 kHz modulation depth of the fundamental BWO carrier signal, 20 kHz frequency steps at the fundamental frequency, an integration time of 200 ms per datapoint, and a total integration time of 33 min. The pressure in the absorption cell was kept between 1 and 100 μ bar for all measurements. The estimated frequency accuracy is 10 kHz for strong and 200 kHz for weaker transitions. These measurements verified that the SL multiplier covers the THz range. The coverage is only limited by the tuning width (78-118 GHz) of the fundamental frequency and the usable harmonic order.

Additional measurements of methanol spectra have been performed at 1 THz using the 11th harmonic of SL I in order to prove the frequency ac-

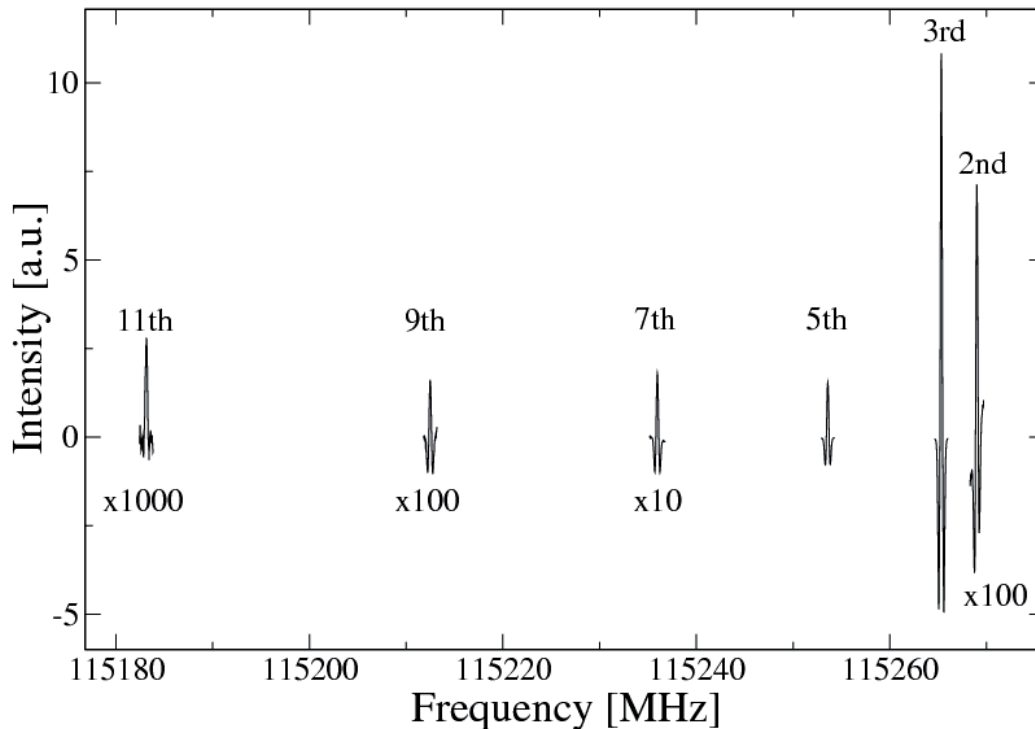


Figure 8.4: Spectra of rotational transitions of CO recorded with different harmonics generated in the SL I. The intensity of weaker lines is magnified by the factor denoted below the transition. Typical integration time ~ 150 s per transition.

curacy of the SL spectrometer. The transition frequencies were compared to measurements by Belov *et al.* [40] using the fundamental frequency of a high frequency BWO. Both measurements agree within errorbars which demonstrates that SL multiplication does not deteriorate the frequency accuracy (see Tab. 8.3) and shows the high internal consistency of the two different methods.

8.3.4 Spectra above 1.5 THz

To test the high frequency performance of SL devices, a large number of transitions of D_2O , HDO, NH_2D and ND_2H in the range from 0.7 to 3.1 THz using multiplication factors up to the 13th have been recorded. For spectroscopic details on ND_2H see Endres *et al.* [84]. For high frequency measurements a BWO (180 - 260 GHz) has been used in combination with the SL II. Pressures in the absorption cell were typically in the range of 0.5-15 μ bar, but in cases of weak lines pressures up to 150 μ bar were used. To record frequencies above 2.3 THz a GeGa detector was used. Mostly, uncertainties of 20-200 kHz for the transition frequencies were estimated. These estimations have been checked by calculations of appropriate combination differences, which form a closed cycle in the energy level diagram (Ritz combination principle). Detailed analysis of the data on D_2O [85], HDO, ND_2H [84] has

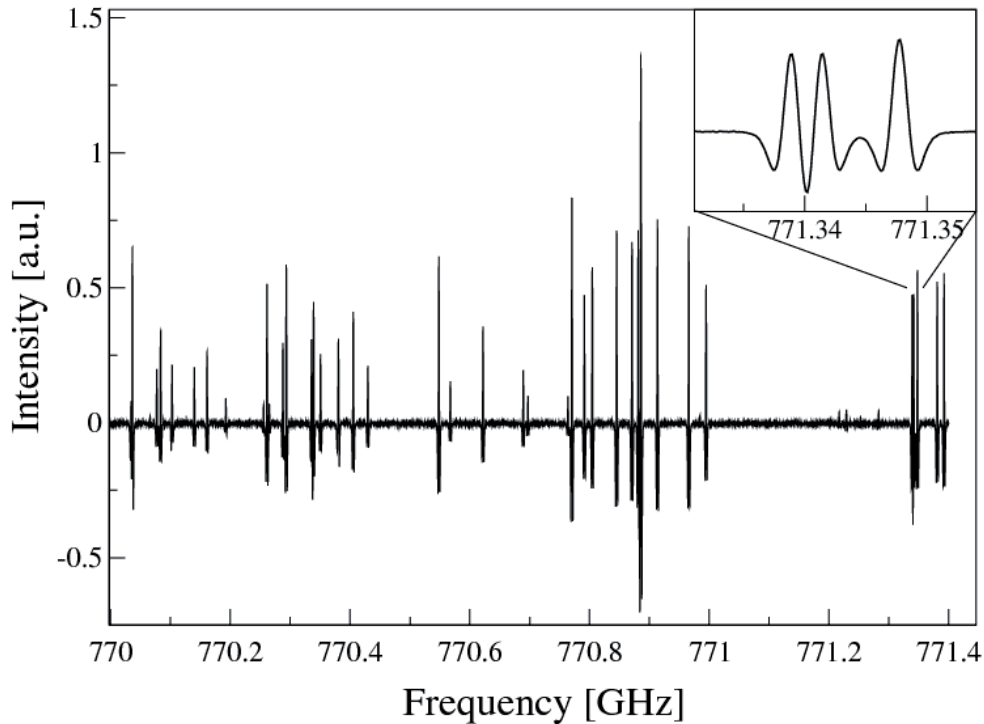


Figure 8.5: Broadband scan of methanol using the 7th harmonic generated by SL I. In the upper right corner a blow-up is shown, which demonstrates the high spectral resolution of the measurement and the low noise.

been published recently and is available via the Cologne database for Molecular Spectroscopy [38, 37, 86]. Spectra up to frequencies of 3.098 THz have been recorded (see Fig. 8.6), which demonstrate the suitability of the SL device for THz spectroscopy. To the knowledge of the author, this is the highest frequency ever reached with frequency multipliers.

8.4 Conclusion

In this work the new superlattice multiplier has been introduced to high resolution microwave spectroscopy. It has been shown that superlattice multipliers are competitive sources for the terahertz range. The present results show advantages in the efficiency of harmonic generation when compared to the performance of Schottky diodes. This makes them very attractive to spectroscopy since only moderate input frequencies are necessary for the production of THz radiation. In the present study 3.1 THz has been generated at an input frequency of 250 GHz. In comparison two doublers and a tripler had to be used at an input frequency of 258 GHz to achieve comparable results. Very broad spectral ranges can be tuned by the SL as shown here for the first time. Setting up a chain of SLs will enable to obtain almost 100% tuning range with only two elements operating as triplers. Moreover, the SL

Table 8.3: Center frequencies of methanol at 1 THz measured with the SL I. For comparison earlier measurements performed by S. P. Belov [40] with the Cologne THz spectrometer are also given.

Frequency [MHz]		Residual [kHz]
This work	Belov [40]	
1000719.087(10)	1000718.982(50)	105
1003529.866(20)	1003529.861(50)	5
1006028.222(20)	1006028.222(50)	0
1006081.258(50)	1006081.187(50)	71
1006111.113(50)	1006111.077(50)	36
1006125.035(50)	1006125.054(50)	-19
1062312.246(20)	1062312.217(50)	29

devices are less vulnerable to electrostatic discharge than Schottky diodes which becomes even more attractive when only a single element has to be used as described above. In the near future a full solid state THz spectrometer will be assembled where a quadrupler or tripler fed by the radiation of a commercial synthesizer will be used to replace the BWO source used in the present investigation.

Technological progress and improved theoretical understanding in the new field of SL devices was immense during the last decade. Future aspects of further SL development concern the use of higher input frequencies like 350 GHz or even 600 GHz instead of 250 GHz in order to reach even higher output frequencies and higher output power. Much better performance of the SL is expected for cooled devices since ohmic losses shall be reduced considerably. In the present setups only fixed waveguide configurations have been used. Enhanced performance shall be attainable when online tuning elements are added to the waveguides.

The development of THz radiation sources is a very dynamic field of research, in which new devices such as the SLs outdate the widely used Schottky diode spectrometers. Considering the wide tuning range combined with the rather high frequencies reached, SL multipliers are presently one of the most interesting devices for THz spectroscopy.

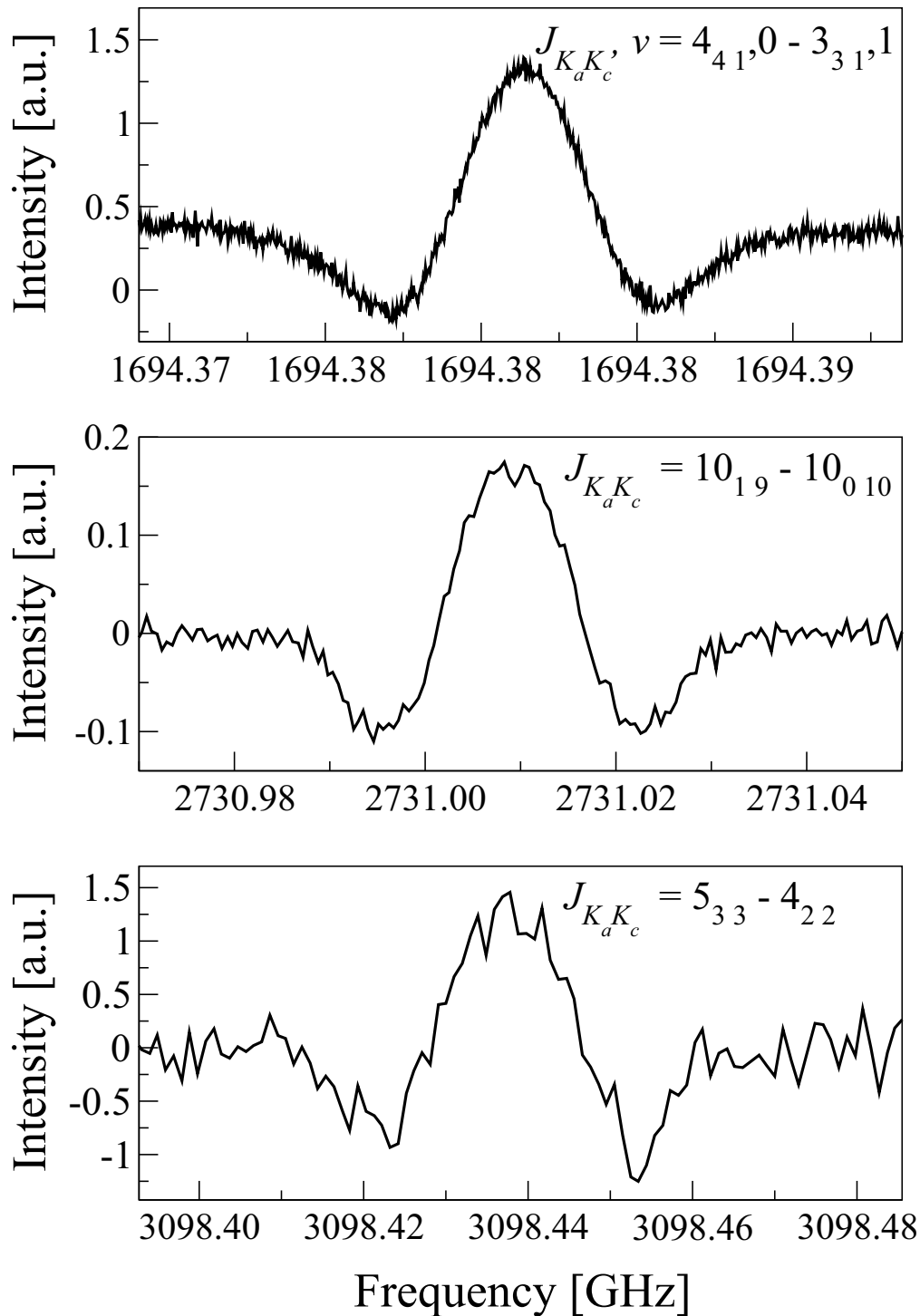


Figure 8.6: Spectra of ND_2H (upper panel) and D_2O (lower panels) recorded with a BWO (OB-24) and the SL II using the 7th (7.12 kHz modulation frequency, 300 kHz modulation depth of the fundamental BWO carrier signal, 300 ms time constant, 5 kHz frequency steps at the fundamental frequency, 3 scans) and 11th harmonics (7.12 kHz modulation frequency, 1 MHz modulation depth of the fundamental BWO carrier signal, 200 ms time constant, 50 kHz frequency steps at the fundamental frequency, 10 scans), respectively. The D_2O -spectra at lowest panel around 3.1 THz is recorded at the highest frequency reached with a SL multiplier using the 13th harmonic (205 scans, 200 ms time constant and 1 MHz modulation depth at the fundamental BWO carrier signal, 75 kHz frequency steps at the fundamental frequency).

Heterodyne Detection Techniques

The exploration of the THz frequency domain strongly depends on the development of compact powerful radiation sources and sensitive detector systems. Usually, incoherent detection techniques based on Schottky diodes, bolometers or photoconductors are applied in ordinary absorption spectrometers. Their relatively constant sensitivity as a function of wavelength is often a desirable property of these detectors. At THz frequencies where the power of the radiation sources are quite limited (in the order of $1 \mu\text{W}$) the detector sensitivity is crucial and only detector systems applying cryogenic techniques attain the required sensitivity. Composite bolometers, such as Si composite bolometers, achieve high sensitivities in the order of $10^{-14} \text{ W}/\sqrt{\text{Hz}}$ [87, 88, 89], but they show relative large response times, which limits the applicable modulation frequencies to below 1 kHz. Relatively fast detection up to 1 MHz is obtained with Indium Antimonide (InSb) hot electron bolometers. Their sensitivity is in the order of several $10^{-12} \text{ W}/\sqrt{\text{Hz}}$ [87, 88, 89]. Above 2.3 THz, photoconductors can be applied. If modulation frequencies of 50 kHz are used, their sensitivity is still better than $10^{-12} \text{ W}/\sqrt{\text{Hz}}$ [87, 88]. Their cut-off frequency can be reduced to about 1.4 THz if the detector crystal is mechanically stressed, even though this reduces their sensitivity. Best sensitivities are obtained with transition edge sensors (TES), which are operated at the superconducting transition of a superconductor ($\text{NEP} \ll 10^{-16} \text{ W}/\sqrt{\text{Hz}}$ [90]). However, if applied in laboratory spectrometers, they are exposed to background radiation of the surrounding 300 K hot environment, which degrades their sensitivity considerably as they are sensitive to a broad spectral range and get saturated [89]. The photon noise generated by the laboratory environment at room temperature is in the order of $10^{-13} - 10^{-14} \text{ W}/\sqrt{\text{Hz}}$ for a typical bolometric detector system with more than 1 THz bandwidth. In the laboratory, the photon noise of the background can only be reduced by a reduction of bandwidth or by limiting the number of detectable spatial modes.

An alternative detection technique is heterodyne detection, which is a coherent detection technique. The incoming radio-frequency (RF) radiation is downconverted by a non-linear device to a considerably lower frequency

band, the intermediate frequency (IF), under conservation of frequency and phase information. The downconverted frequency is subsequently spectrally resolved by a spectrometer, which typically splits the several GHz wide IF band into many thousand channels of 1 MHz or less width. Thus it is subjected to a narrow band filter in the order of MHz. This reduces the photon noise by a factor of 10^6 . Heterodyne detectors are widely used in astronomical receiver systems as they provide a high spectral resolution of the astronomical spectrum. By the use of superconductive mixer elements, such as superconductor-insulator-superconductor (SIS) or hot-electron bolometers (HEB) devices, extremely high sensitivities close to the quantum limit are obtained. Analogous to their application at telescopes, they can be applied to record emission spectra in the laboratory. Due to their spectral sensitivity, they can also be used in combination with extremely low power monochromatic sources (<1 pW) in order to record absorption spectra with good signal to noise levels. Unwanted harmonics or sidebands, often present in sources based on frequency multipliers appear at different IF frequencies and do not disturb the detection of the carrier signal. This makes this detection technique in particular interesting in combination with SL multipliers, where a large number of harmonics is present in the outgoing radiation. Mixer elements used in THz heterodyne receivers are also extremely fast devices and response times below 1 ps are naturally guaranteed. They are therefore also well suited to study fast processes with time-resolved measurements. As heterodyne instruments are easily calibrated, they can directly measure absolute line intensities and might therefore also be an useful tool to study line profiles as the line shapes are not distorted by modulation techniques.

In the scope of this work, two heterodyne receivers developed for radio astronomy were operated in the laboratory in order to investigate their applicability to laboratory spectroscopy. Spectra of gas phase molecules, such as D_2O , HDO, and methanol, have been recorded. The spectral lines are observed in emission against a cold absorber background, and in absorption against a monochromatic radiation source. Both receivers, the 1.5 THz superconductive HEB heterodyne receiver CONDOR [48] and the 800 GHz NANTEN 2 SIS test receiver system, have been designed and constructed for operation at radio telescopes by the Cologne instrumentation groups and achieve high quantum efficiency.

In combination with monochromatic radiation sources the obtained sensitivity is often limited by the dynamic range in the post detection process, i.e. analog to digital conversion or the noise generated in the backend spectrometer. For radiation sources with around $1 \mu W$ less sensitive mixer elements at room temperature, such as Schottky or SL diodes, might therefore already provide sufficient signal to noise levels. Such a very compact heterodyne system working at room temperature was realized in the sub-mm - region within this work, based on superlattice (SL) devices as mixer elements. It was successfully used to record spectra of dimethyl ether by employing different post detection techniques. Although less sensitive, it provides fast detection, large tuning range, but very narrow bandwidths detection at room temperature

with a very compact setup. The ability to detect only one harmonic generated by a SL multiplier source makes it again a very interesting source in combination with SL radiation sources. With currently available analog to digital converters it is possible to directly digitize the IF signal and to apply digital filters in the computer analysis. Two post detection techniques have been applied within this work. The first one uses a power detector to record the continuum after a relatively narrow bandpass filter ($B \simeq 40$ MHz). This method is equivalent to incoherent detection within the narrow bandpass and frequency as well as amplitude modulation techniques can be applied. The second technique downconverts the IF signal again and records the power directly without any modulation.

The aim of these feasibility studies, described in this section, was to qualitatively and quantitatively characterize the prospect for application of heterodyne detectors in high resolution laboratory spectroscopy. Therefore the proof of principle, the determination of signal to noise levels, and the estimation of integration times for future applications are investigated.

9.1 Principles of Heterodyne Detection

In contrast to incoherent detection methods, coherent detection methods allow to record thousands of frequency channels simultaneously. Basic technology is a heterodyne system as depicted in Fig. 9.1, which down-converts the incoming radio-frequency (RF) signal to a lower intermediate frequency (IF) without loss of phase-information. Usually, IF frequencies in the range of up to a few GHz are chosen that can easily be processed by commercial low noise electronics in the signal post detection process. In order to obtain a frequency-domain spectrum, the IF output signal is resolved by a high resolution spectrometer, such as acousto-optical spectrometers (AOS) [91] or fast digital Fourier transform spectrometers (FFTS) [92]. Advances in computer technology led to increasing popularity of the latter in the past few years.

The down-conversion is realized with devices as mixer elements, which exhibit non-linear electric characteristic, i.e. in their IV-curves. As shown in the figure, the mixer is the first active device in such a receiver system. Typically, the incoming signal $E_{sig} \cos(\omega_{sig}t + \phi_{sig})$ is superimposed with the signal of a local oscillator (LO) $E_{LO} \cos(\omega_{LO}t + \phi_{LO})$, which is several magnitudes higher in power and tuned to a frequency defined by the IF frequency range of the receiver, e.g. typically 1-10 GHz away from the signal frequency.

Using the simplified assumption that the output IF signal is proportional to the square of the amplitude, the current in the mixer element is:

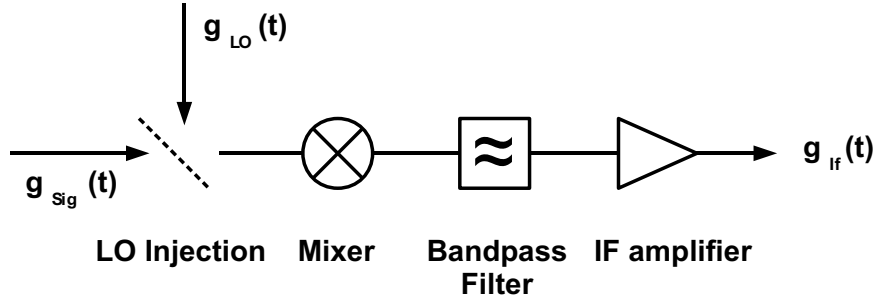


Figure 9.1: Fundamental layout of a heterodyne receiver. The signal of a local oscillator $g_{LO}(t)$ and the source signal $g_{sig}(t)$ are combined on the mixer device. Among others, the difference signal (so-called intermediate frequency - IF) is generated in the mixer, which is filtered by the bandpass filter and subsequently amplified.

$$\begin{aligned}
 I &\propto (E_{sig} \cos(\omega_{sig}t + \phi_{sig}) + E_{LO} \cos(\omega_{LO}t + \phi_{LO}))^2 \\
 &= E_{sig}^2(1/2)(1 + \cos(2\omega_{sig}t + 2\phi_{sig})) + E_{LO}^2(1/2)(1 + \cos(2\omega_{LO}t + 2\phi_{LO})) \\
 &\quad + E_{sig}E_{LO}[\cos((\omega_{sig} + \omega_{LO})t + (\phi_{sig} + \phi_{LO})) \\
 &\quad + \cos((\omega_{sig} - \omega_{LO})t - (\phi_{sig} + \phi_{LO}))]
 \end{aligned} \tag{9.1}$$

For an ideal mixer with unity mixer gain and $V_s = V_{LO} = 1$, the mixer IF signal output g_{IF} after passing through an appropriate bandpass filter, becomes

$$g_{IF}(t) = \cos(|\omega_{sig} - \omega_{LO}|t \mp \phi_{IF}) \tag{9.2}$$

Thus, the IF signal is at the difference frequency of the LO and the input signal. ϕ_{IF} is the down-converted phase ($\phi_{sig} + \phi_{LO}$).

If the signal frequency is greater than the LO frequency, the corresponding intermediate frequency is positive. Such a signal is said to be in the upper sideband (USB). If the signal frequency is less than the LO frequency the intermediate frequency is mathematically negative, and the signal will reside in the lower sideband (LSB). As negative IF frequencies do not exist, the down-converted lower sideband will be present as positive frequency in the double sideband (DSB) receiver IF output, albeit with 180 phase shift. For a double sideband receiver, the upper and lower sidebands fold in the IF. Sideband separation can be obtained with single sideband mixers, which are designed to suppress one of the sidebands making use of the phase relation. Otherwise, the sidebands can be distinguished, e.g. by a second measurement recorded with a slightly detuned LO frequency, as shown in Sec. 9.2.5.

In addition to the full phase information of the input signal, its amplitude information is conserved in the IF signal. The IF signal is commonly

amplified with a chain of low-noise amplifiers and filtered with an appropriate bandpass filter before it is processed in the post detection unit, i.e. a spectrometer.

9.2 Detection with Superconducting Mixers

Currently, the most sensitive mm, sub-mm, and THz heterodyne receivers are based on superconductive mixer elements. Superconductor-insulator-superconductor (SIS) tunnel junctions are preferably used as mixers as they are extremely broadband in the intermediate frequency, are comparatively stable, and are relatively simple to operate in a receiver. Their operation is based on the principle of photon-assisted tunneling and the extremely non-linear quasi-particle tunneling current is used for mixing. The best material combination for SIS mixers at lower frequencies (<700 GHz) is Nb-Al₂O-Nb based on Niobium as superconductor. The applicable frequency range is theoretically limited for SIS junction by the energy gap of the superconductor, which is 1.4 THz for an SIS junction with two Niobium electrodes. Above this limit frequency a different mixer concept has to be used. Superconductive Hot Electron Bolometer mixers, made of NbTiN for example, do not have an upper frequency limit. Their operation uses bolometric effects and rely on the temperature dependence of the resistance of a superconducting micro-bridge near the superconducting transition temperature. As they react on the square of the sum of the signal and the local oscillator electrical field, the temperature fluctuations only can follow the beat frequency due to the internal time constants of the device.

The development of superconductive mixers is a very active field of research. For further reading the works [93, 94, 95] are recommended. The KOSMA Superconducting Devices and Mixers Group at the Cologne university is active in developing, producing, and improving both types of mixers. The superconductive mixers used in the heterodyne receivers applied within this work have been build in-house by this group and the measurements have been performed in close collaboration.

9.2.1 Receiver Noise Temperature

The sensitivity of heterodyne receivers is characterized by the receiver noise temperature T_{rec} , which includes all noise contributions from all components of the receiver system. T_{rec} is obtained by measuring the power spectrum of a black body at two different temperatures, usually an absorber at room temperature and at liquid nitrogen temperature (77 K) [91]. The spectrum measured at the receiver output is then:

$$\begin{aligned} z_L &= (T_L + T_{rx})G && \text{Cold Load} \\ z_H &= (T_H + T_{rx})G && \text{Hot Load} \end{aligned} \tag{9.3}$$

Table 9.1: Receiver noise temperature T_{rec}^{DSB} for some selected heterodyne instruments. The HIFI receivers are aboard the space observatory Herschel. SHeFI T2 is a receiver constructed for the Apex telescope and Condor which has been used in this work, has also been applied to the Apex telescope [48].

Receiver	Mixer Type	Frequency range [GHz]	T_{rec}^{DSB} [K]
Schottky diode @300 K [96]	Schottky diode	585	2380
Schottky diode @77 K [96]	Schottky diode	585	1240
Schottky diode @4.2 K [96]	Schottky diode	585	880
Condor [48]	HEB	1250 – 1530	1600
HIFI - Band 1 [97]	SIS	480 – 640	50 – 60
HIFI - Band 2 [97]	SIS	640 – 800	130 – 200
HIFI - Band 3 [97]	SIS	800 – 960	200
HIFI - Band 4 [97]	SIS	960 – 1120	300
HIFI - Band 5 [97]	SIS	1120 – 1280	600 – 900
HIFI - Band 6 [97]	HEB	1410 – 1910	900 – 1500
SHeFI T2, APEX [98]	HEB	1250 – 1390	1050 – 1500

The noise temperature T_{rec} corresponds to the output signal produced when no external source is connected. $G(\nu)$ and z are the gain transfer as a function of frequency and the receiver output. G cancels out if the quotient

$$y = z_H/z_L \quad (9.4)$$

is calculated and Eq. 9.3 can be solved in order to calculate T_{rec} :

$$T_{rec} = \frac{T_H - yT_L}{y - 1} \quad (9.5)$$

As heterodyne receivers preserve frequency and phase information, their sensitivity is fundamentally limited by the quantum nature of the radiation and thus the quantum noise, which is $h\nu/k_B$ (i.e. 4.8 K/100 GHz) given in units of temperature. Current heterodyne receivers already reach sensitivities, which are only few times this limit. For example, the quantum noise limit is 24 K at 500 GHz. Receiver noise temperatures for some exemplary heterodyne receivers are tabulated in Tab. 9.1.

9.2.2 Experimental Setup

The heterodyne THz receiver CONDOR was used to record spectra at frequencies in the range 1.35-1.50 THz. The receiver was designed to be operated at THz frequencies and its operation was successfully demonstrated at the Apex observatory by recording a CO ($J = 13 - 12$) emission line from Orion FIR4 at 1496.922909 GHz. Its local oscillator consists of a multiplier chain (multiplication factor of 108), which is fed by the signal of a commercial Agilent synthesizer (14 GHz) and generates 0.5 – 10 μ W of output power in the frequency range 1.25–1.53 THz. This signal is combined with the source signal in a Martin-Puplett interferometer, and subsequently directed

onto the NbTiN superconducting Hot Electron Bolometer (HEB)[99] which acts as the frequency mixer. The intermediate frequency is amplified by a low-noise HEMT, which is placed together with the HEB inside a He cryostat cooled to approximately 4.2 K. After passing the bandpass filter the IF signal is processed in an acousto-optical spectrometer (AOS). One Array of the 4x1 GHz Array AOS ([100]) was used, which resolved 1 GHz of the IF signal in 2048 channels. The channel spacing is 558 kHz and the resolution bandwidth of each channel is 1.6 MHz. The emission lines of a test molecule, inside the 50 cm long gas cell with high density polyethylene windows, were recorded against a continuum background, realized by an absorber in a liquid nitrogen (77 K) bath. A schematic sketch of the setup is shown in Fig. 9.2.

The second heterodyne receiver (NANTEN 2 test receiver) was used for further studies focused on quantifying and comparing a heterodyne setup with a conventional bolometer setup. This receiver was designed for frequencies between 780–880 GHz. The local oscillator consists of a phase locked Gunn oscillator as radiation source followed by several frequency multipliers generating the 15th harmonic of the Gunn signal. A SIS mixer placed in a cryostat and cooled to temperatures around 4.2 K, generates the difference frequency (IF-Frequency) of local oscillator and incoming radiation. The IF signal is subsequently amplified by a low-noise HEMT amplifier, also placed in the cryostat. As the IF frequency band ranges from 700 to 2200 MHz the IF signal was afterwards down-converted to the frequency range 0-1500 GHz by the use of a IF processor. The IF signal was spectroscopically resolved by a Fast Fourier Transform Spectrometer (FFTS) (Max-Planck-Institute for Radio astronomy / Radiometer Physics GmbH), which covers the frequency band to 1.5 GHz with 8192 channels. The equivalent noise bandwidth of each channel is 212 kHz. The FFTS can be operated in two phase and four phase signal reference mode (chopped mode) in order to record and integrate up to four spectra simultaneously. This mode is advantageous as it allows long integration times (exceeding the Allan time [101], which specifies the time when the crossover from white noise to 1/f, and drift noise occurs.). Analogous to the first setup, the emission lines of a sample gas were recorded against a continuum background, realized by an absorber in a liquid nitrogen (77 K) bath. The absorption cell was 35 cm long and hermetically sealed by Teflon windows. The chopper wheel was placed between the cooled absorber and the absorption cell.

9.2.3 System Noise Temperature

The system noise temperatures T_{sys} measured for both heterodyne systems are shown in Figs. 9.3 (CONDOR) and 9.4 (NANTEN 2 test receiver). The measurement setup is identical to Sec. 9.2.1 with the only difference being the absorption cell in front of the hot and cold load (Fig. 9.2). Thus, they include noise contributions from the absorption cell and the Teflon windows ($T_{\text{sys}} = T_{\text{rec}} + T_{\text{optic}}$). Spectra of hot-cold measurements often obey a frequency dependence, which is caused by a variety of effects. In general,

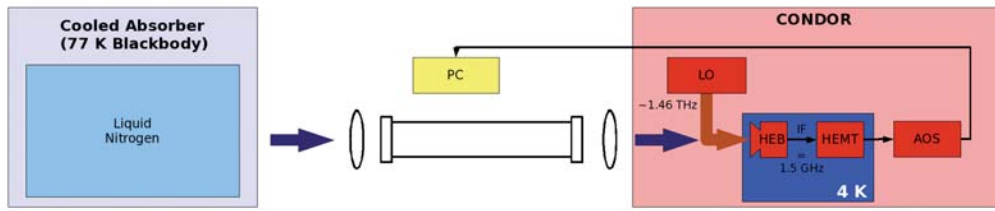


Figure 9.2: Schematic of the spectrometer setup using the CONDOR heterodyne receiver for detection. The emission lines of a sample gas are recorded against a continuum background, realized by an absorber in a liquid nitrogen (77 K) bath. The mixer element is a superconductive hot electron bolometer. The IF signal is finally detected and spectrally resolved with an AOS spectrometer.

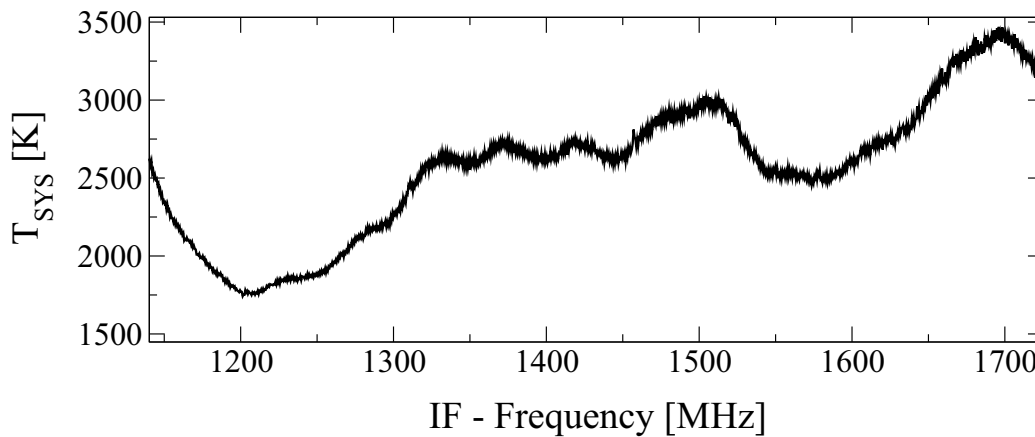


Figure 9.3: System noise temperature T_{Sys}^{DSB} of CONDOR at $f_{LO} = 1463.074$ GHz.

standing waves in the optical path arising from reflection losses at windows or lenses, as well as standing waves in the cable between mixer and low noise amplifier have the predominant influence. The hot cold measurements with the CONDOR receiver have been recorded through the empty absorption cell. At an IF Frequency of 1500 MHz a system temperature of $T_{sys} = 3000$ K was determined.

The system temperatures of the NANTEN 2 test receiver have been determined for four different configurations. Curves a) and b) correspond to measurements where the absorption cell is removed from the signal path between detector and load, whereas the measurements c) and d) are measured through the evacuated absorption cell. As expected T_{sys} is considerably higher in the latter case because the emission and absorption at the Teflon windows of the absorption cell contribute considerably to T_{sys} . In case b) and d) a mechanical chopper is used ($f = 40$ Hz) in order to integrate the spectrum of the cold and the hot load simultaneously. In measurement a) and c) cold and hot spectrum is recorded consecutively. The larger T_{sys} in case of the chopped measurement is due to the finite time required by the chopper to mask the optical path to the cold absorber completely. In these measurements part of the cold background signal is integrated to the hot load measurement and vice versa, which results to an effective increase/decrease of the measured temperature of the cold/hot load.

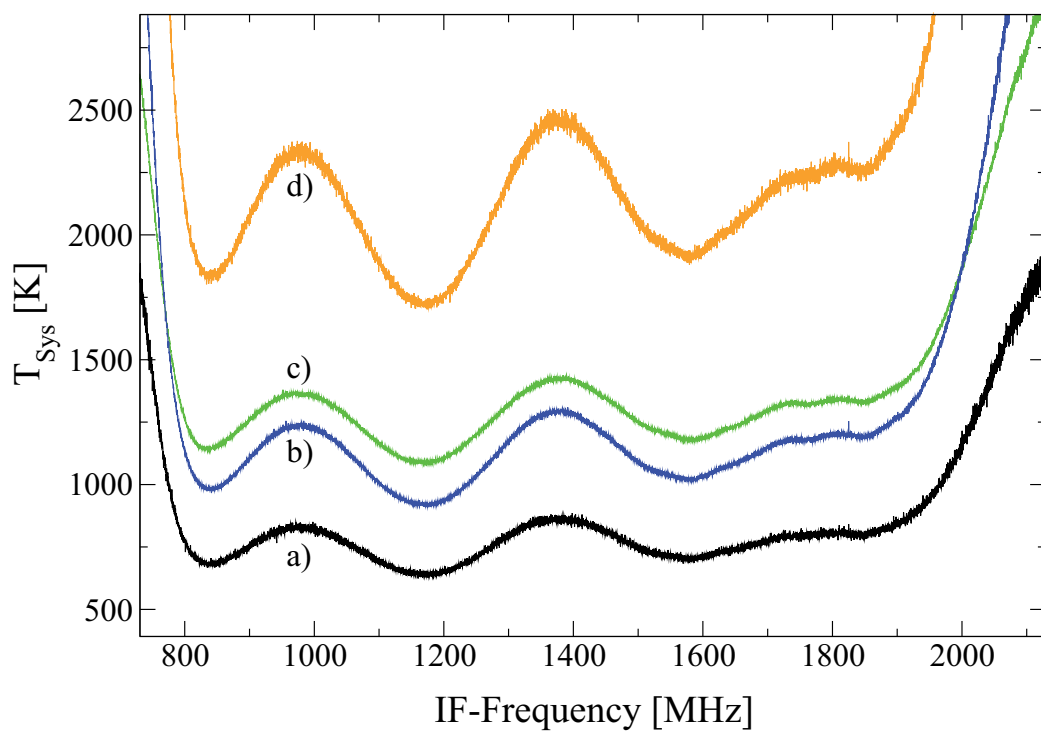


Figure 9.4: System noise temperature T_{Sys}^{DSB} of the NANTEN 2 test receiver at $f_{LO} = 825.800$ GHz. The noise temperature is shown for four different setups: a) Direct measurement without absorption cell. b) Measurement with chopper and without absorption cell. c) Measurement without chopper through evacuated absorption cell. d) Measurement with chopper through evacuated absorption cell.

Once the system temperature is known, a lower limit of the achievable minimum noise ΔT can be calculated by using the radiometer formula [102]:

$$\Delta T = \frac{T_{\text{sys}}}{\sqrt{\Delta\nu \cdot \tau}} \quad (9.6)$$

$\Delta\nu$ is the equivalent noise bandwidth of the spectrometer backend and τ the integration time. As long as no systematic noise contribution affects the spectrum, the noise ΔT decreases with the square root of the integration time τ .

9.2.4 Emission Spectra

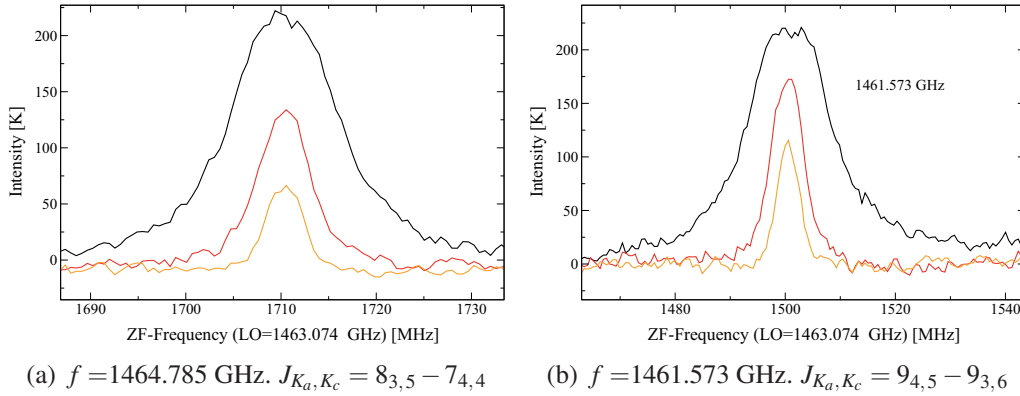


Figure 9.5: Emission spectrum of D_2O recorded with the CONDOR heterodyne system against liquid N_2 background. The spectrum is recorded at three different pressures in the absorption cell: $8 \mu\text{bar}$ (orange), $25 \mu\text{bar}$ (red), and $150 \mu\text{bar}$ (black).

Emission spectra of D_2O have been recorded using a LO frequency of $f_{LO} = 1463.074$ GHz (Fig. 9.5). The measurements have been carried out at three different pressures ($8 \mu\text{bar}$, $25 \mu\text{bar}$, $150 \mu\text{bar}$) with a total integration time of 10 s each. The transitions shown in the figure belong to the transition frequencies $f = 1461.573$ GHz ($J_{K_a, K_c} = 9_{4,5} - 9_{3,6}$) and $f = 1464.785$ GHz ($J_{K_a, K_c} = 8_{3,5} - 7_{4,4}$) and are thus located in different sidebands. At a pressure of $150 \mu\text{bar}$ both transitions are optically thick and thus the maximum intensity is reached, which is $(300-77)$ K = 223 K for a background temperature of 77 K provided by observing against a liquid nitrogen cooled absorber. This fact allowed the absolute calibration of the recorded spectra. Intensities have been derived by fitting the line profile using a Voigt-function. In Tab. 9.2 intensities are compared to predicted values taken from the *Cologne Database for Molecular Spectroscopy* (CDMS). All experimental values match well with the theoretical value. After 10 s integration time a noise level of

$$\Delta T = 2\sqrt{2} \frac{3000 \text{ K}}{\sqrt{1.6 \text{ MHz} \cdot 10 \text{ s}}} = 2.1 \text{ K} \quad (9.7)$$

Table 9.2: Calculated and measured intensities derived from emission spectra (Fig. 9.5) recorded at three different pressures. Calculated intensities are taken from the Cologne Database for Molecular Spectroscopy (CDMS).

Transition	Pressure [μbar]	Intensity [10^{-16} MHz/(molecules/cm ²)]
f=1464.785 GHz $J_{K_a, K_c} = 8_{3,5} - 7_{4,4}$	calculated	1.799
	8	2.06
	25	1.85
	150	1.84
f=1461.573 GHz $J_{K_a, K_c} = 9_{4,5} - 9_{3,6}$	calculated	3.342
	8	3.33
	25	3.29
	150	3.03

is expected. Factor of two accounts for the single sideband (The emission line is just in one of the sidebands) and the factor $\sqrt{2}$ considers the fact that the spectra shows the difference of two spectra (with and without gas sample for background subtraction). The AOS spectrometer used with CONDOR has an equivalent noise bandwidth of $\nu = 1.6$ MHz. The experimentally determined rms noise of $\Delta T \approx 3$ K in the spectra agrees within a factor of two with the theoretical value.

By recording 100 subsequent scans of the same portion of the rotational spectrum of methanol at a pressure of 7 mTorr, the dependence of noise on the integration time (Eq. 9.6) was experimentally investigated with the NANTEN 2 test receiver. The scans have been consecutively recorded with a total integration time of $2 \cdot 25$ s per scan (simultaneous hot and cold measurement) using the chopper configuration ($f_{chopper} = 40$ Hz). The noise corresponding to an integration time of $n \cdot 50$ s was determined by averaging n consecutive scans and calculating the rms noise over 40 adjacent channels free of molecular emission in the averaged spectrum. In Fig. 9.6 this rms noise normalized to the value obtained after 1 scan (50 s) is plotted versus the integration time in double logarithmic scale. After 100 scans the rms noise is reduced to one tenth of the rms noise of the first scan, as expected. Data reduction yields a power factor of $a = -0.48 \pm 0.07$ (blue curve) which coincides within errorbars to the theoretical value $a = -0.5$ derived from the radiometer formula.

The spectrum averaged over all 100 scans is shown in Fig. 9.7. The intensity scale is calibrated to absolute intensities given in K :

$$p = 2(T_{Hot}^{backgr} - T_{Cold}^{backgr}) \frac{(z_{Hot}^{backgr} - z_{Cold}^{backgr}) - (z_{Hot}^{gas} - z_{Cold}^{gas})}{(z_{Hot}^{backgr} - z_{Cold}^{backgr})} \quad (9.8)$$

with $T_{Hot}^{backgr} = 300$ K and $T_{Cold}^{backgr} = 77$ K. z_{Hot}^{backgr} and z_{Cold}^{backgr} are the power spectra of Hot and Cold load measured through the evacuated absorption cell. Again, the factor of 2 accounts for the fact that discrete lines are just in one of the sidebands but the continuum radiation is detected in both

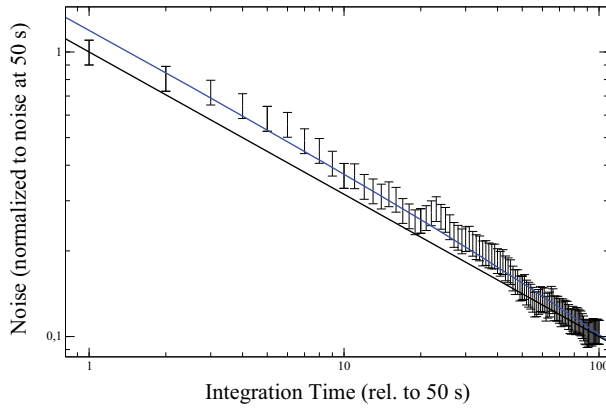


Figure 9.6: Relative rms noise in dependence of the integration time. The rms noise is normalized to the rms noise obtained at an integration time of 50 s. The uncertainty of the rms noise is estimated to be 10 % of the absolute value. The solid lines show the relative rms noise in dependence of integration time as theoretically expected (black) and obtained from a regression to the experimental values (blue).

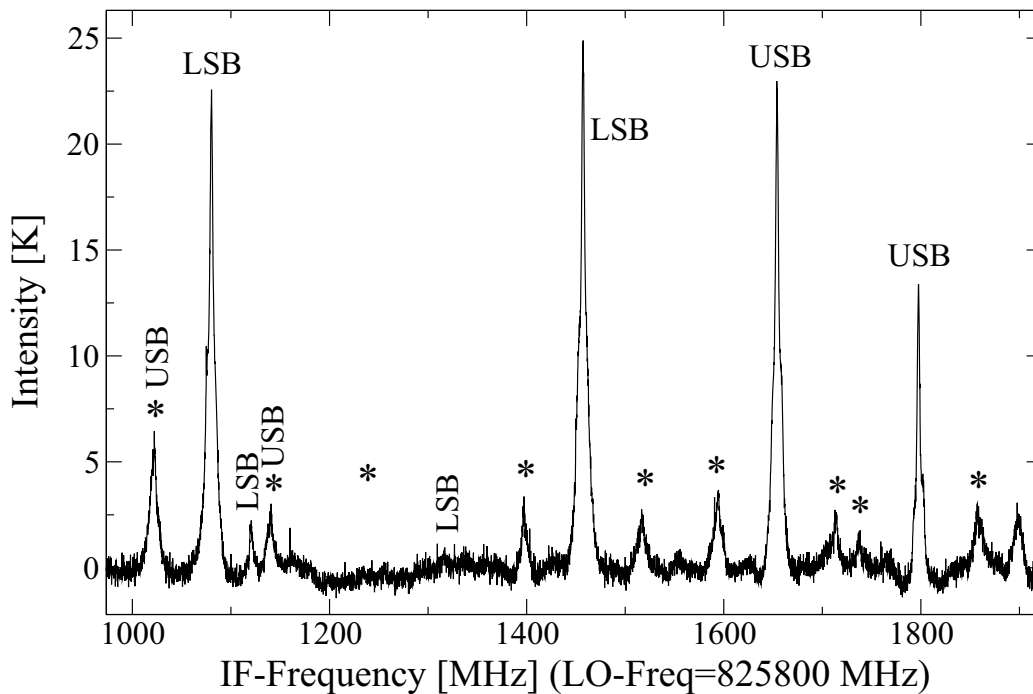


Figure 9.7: Emission spectrum of methanol after 5000 s integration time. The spectrum is recorded using a chopper to simultaneously record the spectrum against cold (77 K) and warm (300 K) background.

Table 9.3: Experimental frequencies and intensities of methanol. Experimental frequencies are compared to previous works. The calculated intensities are based on the analysis done by Li Hong Xu [103]. Blended lines are indicated by the letter *b* behind the IF frequency. The tabulated experimental intensities refer to the observed line, whereas the calculated values denote the intensity of the transition.

Transition $J'_{K'_a, K'_c}, v'_t - J''_{K''_a, K''_c}, v''_t$	IF Frequency [MHz]	Exp. Transition Frequency [MHz]		Peak Intensity [K]	
		This work	Prev. work [103]	Exp.	Calc.
28 _{5,24,0} -28 _{4,24,0}	1021.501(150)b	826821.501(150)	826822.506(50)	6.4	4.2
20 _{-1,20,0} -19 _{0,19,0}	1080.087(150)	824719.913(150)	824719.749(50)	22.8	24.7
30 _{5,26,0} -30 _{4,26,0}	1120.455(150)	824679.545(150)	824679.491(50)	2.2	2.9
22 _{11,12,0} -23 _{10,13,0}	1140.165(150)b	826940.165(150)	826936.887(50)	3.2	0.42
22 _{11,11,0} -23 _{10,13,0}	1140.165(150)b	826940.165(150)	826936.887(50)	3.2	0.42
6 _{6,1,0} -7 _{5,3,0}	1316.168(300)	824483.832(300)	824483.901(50)	0.8	0.35
6 _{6,0,0} -7 _{5,3,0}	1316.168(300)	824483.832(300)	824483.901(50)	0.8	0.35
17 _{-2,16,0} -16 _{-2,15,0}	1457.226(150)	824342.774(150)	824342.689(50)	25.1	24.1
17 _{1,16,0} -16 _{1,15,0}	1654.043(150)	827454.043(150)	827453.973(100)	23.2	25.2
8 _{4,4,1} -9 _{5,5,1}	1797.555(150)	827597.555(150)	827597.349(100)	13.6	8.75
8 _{4,5,1} -9 _{5,5,1}	1797.555(150)	827597.555(150)	827597.349(100)	13.6	8.75

sidebands. Artifacts from the Gunn phase-lock show up in the spectra, which are indicated by a star above the peak. They arise from spectral impurities of the LO radiation and occur at frequencies of 60 MHz above and below the transition frequencies. The 60 MHz signal originates from the IF signal of the Gunn phase lock loop. Although such impurities due to sideband effects or spurious harmonics may occur, they are usually at least 30 dB below the carrier signal in good quality LOs.

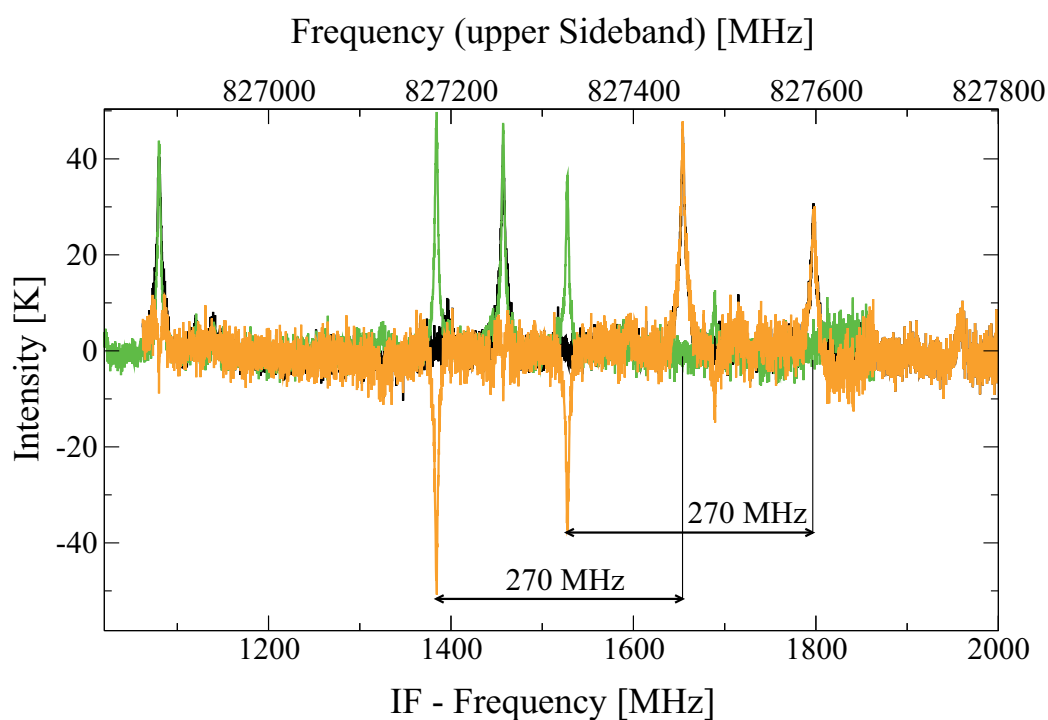
Experimental frequencies and peak intensities have been determined in this spectrum and are summarized in Tab. 9.3 together with experimental frequencies determined by L. H. Xu [103]. Based on her work, peak intensities have been calculated, which are also shown in this table. All frequencies agree within errorbars except for blended transitions. Also the intensities are in relatively good agreement. The weakest transition, which has been determined in this spectrum has an intensity of 0.7 K and is just slightly above the noise level. By calculating the rms value of the recorded spectrum as an average over 40 channels, a noise level of $\Delta T \approx 420$ mK is obtained, which is less than a factor of two above the theoretical value of $\Delta T = 270$ mK. The maximum signal achieved for an optically thick emission line, if the gas is at room temperature and the cold load is a liquid nitrogen cooled absorber, is 223 K. Thus, the maximum signal-to-noise ratio for an optically thick transition after an integration time of $2 \cdot 2500$ s (hot and cold measurement) is $\text{SNR} = 530$ in this setup. This corresponds to minimum detectable absorption coefficient of $\alpha = 5.39 \cdot 10^{-6} \text{ cm}^{-1}$, if a 350 cm long gas cell would be applied. At a pressure of 100 mTorr and a linewidth of 1 MHz at half-width at half-height the minimum detectable line intensity is $I = 1.8 \cdot 10^{-25} \text{ cm}^{-1}/(\text{molecules}/\text{cm}^{-1})$.

9.2.5 Sideband Identification

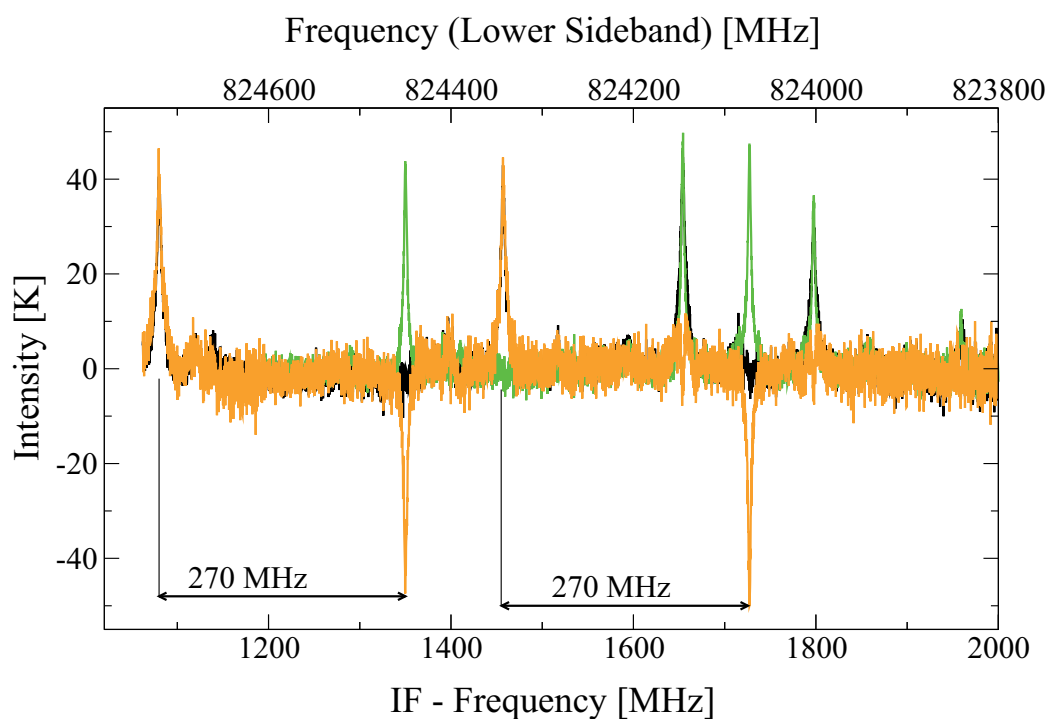
Principally, heterodyne detectors detect upper and lower sideband simultaneously. Sideband filtering or separation can be implemented in receivers, but demand a significantly larger technological effort. Both the Nanten 2 test receiver and the CONDOR receiver are double sideband detectors. In recorded spectra it cannot be distinguished if the absolute frequency of a line is above or below the frequency of the local oscillator, because only the absolute value of the difference frequency is determined. But by recording another spectra with a slightly shifted LO frequency, it is possible to unambiguously assign the sideband of a spectral line and thus its absolute frequency. If the LO frequency is shifted towards higher frequencies lines which occur in the lower sideband are shifted by the same amount towards higher frequencies in the IF band whereas lines in the upper sideband are shifted towards lower frequencies in the IF band. One possibility to identify the sidebands in the spectra is to overlay both spectra by adding the arbitrarily chosen difference of the LO frequencies from the frequency of second spectrum as done in Fig. 9.8(a). The black curve is the spectrum recorded at an LO frequency of 825800 MHz and the green curve is the spectrum recorded at an LO frequency of 825935 MHz. Afterwards 135 MHz is subtracted from the IF frequency of the second spectrum. Thus lines which occur in the upper sideband of both spectra lie on top of each other. If the difference between both spectra is calculated as shown in orange color, lines in the upper sideband cancel out and lines which are in the lower sideband occur twice, once with positive intensity and once with negative intensity. Those with negative intensity are shifted by $2 \cdot 135$ MHz towards lower IF frequencies compared to their positive mirrors. Now the transition frequencies can be directly determined, because lines with positive intensities are those which occur in the lower sideband and their frequency is just $f = f_{LO} - f_{IF} = 825800 \text{ MHz} - f_{IF}$. Lines of the upper sideband can be determined analogously by subtracting 135 MHz from the IF frequency of the second spectrum (Fig. 9.8(b)). The uncertainty of the determined transition frequency can easily be determined by fitting the line profile of the positive and the negative feature. As both obtained frequencies have to be shifted exactly by 270 MHz, the deviation of this difference to 270 MHz indicates the accuracy of the experimentally obtained transition frequencies.

9.2.6 Detection of Monochromatic Signals

The signal strength obtained in emission spectra, recorded against cold backgrounds is limited by the difference of the temperatures of the cooled absorber and the gas sample times the transition strength. If the cooled absorber is replaced by a radiation source, the intensity difference of the background signals (Hot, now corresponding to the background, and Cold, now corresponding to the gas sample) can be increased drastically and absorption spectra are obtained.



(a) Upper Sideband.



(b) Lower Sideband.

Figure 9.8: Separation of sidebands. The methanol spectrum is recorded at LO frequencies of 825800 MHz (black) and 825935 MHz (green). The IF frequency of the latter spectrum is shifted by 135 MHz to lower (a) and upper frequencies (b) in order to overlay lines which appear in the lower and upper sideband, respectively. In the difference spectra (orange) only such spectral lines appear, which are either in the upper (a) or in the lower (b) sideband. In the difference spectra each line occurs twice. Transitions at $f_{IF} = |f_{center} - 825800| \text{ MHz}$ have positive intensity and are mirrored at $f_{IF} = |f_{center} - 825800| \pm 270 \text{ MHz}$ with negative intensity.

In the following, heterodyne detection of monochromatic radiation sources will be presented and discussed. Based on these first quantitative results, the perspective and scope of application of such an approach will be outlined. The setup shown in Fig. 9.9 uses the CONDOR heterodyne receiver in combination with the 17th harmonic generated by a superlattice frequency multiplier as radiation source. The SL multiplier is fed by the radiation generated with a phase locked Gunn oscillator operating at ≈ 86 GHz. The signal is downconverted after passing the absorption cell with the heterodyne system described earlier (Sec. 9.2.2) and the IF signal is integrated without modulation techniques by the AOS.

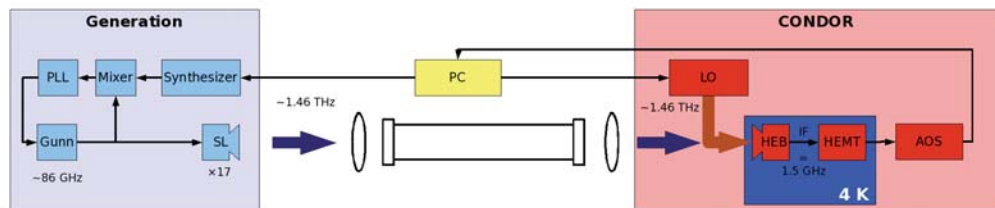


Figure 9.9: Schematic of the absorption spectrometer setup using the CONDOR heterodyne receiver for detection. The radiation is generated by a phase-locked Gunn oscillator. The 17th harmonic generated in the cascaded SL multiplier passes the absorption cell and is detected with the CONDOR heterodyne receiver at 1.46 THz. The mixer element is a superconductive hot electron bolometer. The IF signal is finally detected with an AOS spectrometer.

Linewidth of SL-Harmonics

As the intermediate Frequency (IF) signal between the Condor LO system and the 17th harmonics generated by the SL gives valuable insights on the frequency accuracy, noise properties and the output power of the SL device, the properties of the SL radiation are investigated first. Both signals are independently phase-locked to a single reference oscillator (10 MHz) and thus the line width of the IF signal gives an upper limit of the line width and the frequency stability of the 17th harmonic generated by the SL at 1500 GHz. In Fig. 9.10 this IF signal is shown together with the PLL lock signal of the Gunn oscillator, which acts as radiation source for the SL multiplier. The line width is mainly dominated by the phase noise. The phase noise present in the Gunn signal is amplified by frequency multiplication and leads to an amplification of the amplitude of the sideband signal by the multiplication factor N . The noise power increases by a factor $20 \log(N)$. The minimum reduction of the signal to noise ratio expected for the 17th harmonic of the Gunn signal is thus $20 \log(17)$ dB = 24.6 dB. As can be seen in Fig. 9.10 the signal to noise ratio is decreased by 28 dB after the multiplication, which is just slightly above this theoretically expected value. As the contributions from the Condor LO signal are unknown, the source of the additional noise contributions cannot be distinguished. The line width of the 17th harmonic is better than 3 kHz at half maximum.

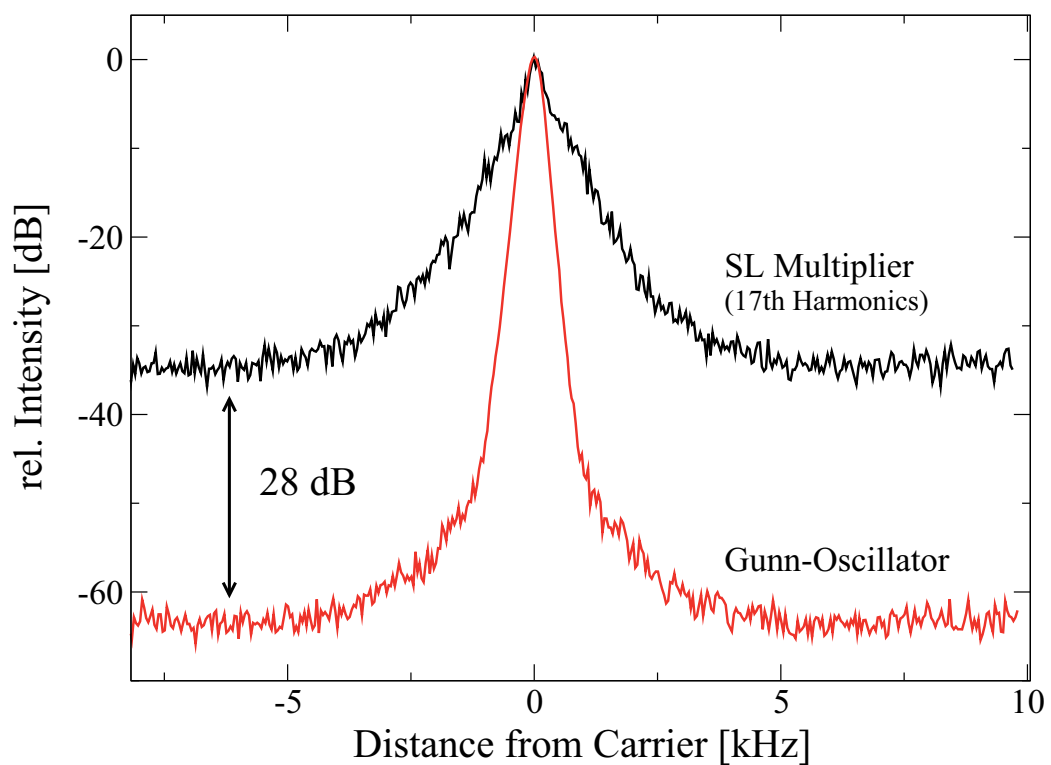


Figure 9.10: IF-Signal of the 17th Harmonics generated by the SL and detected with Condor (1498.5 GHz), and the IF-Signal of the Gunn-Oscillator (125.8 MHz). Both IF-Frequencies have been recorded at a resolution bandwidth of 300 Hz by the use of a spectrum analyzer.

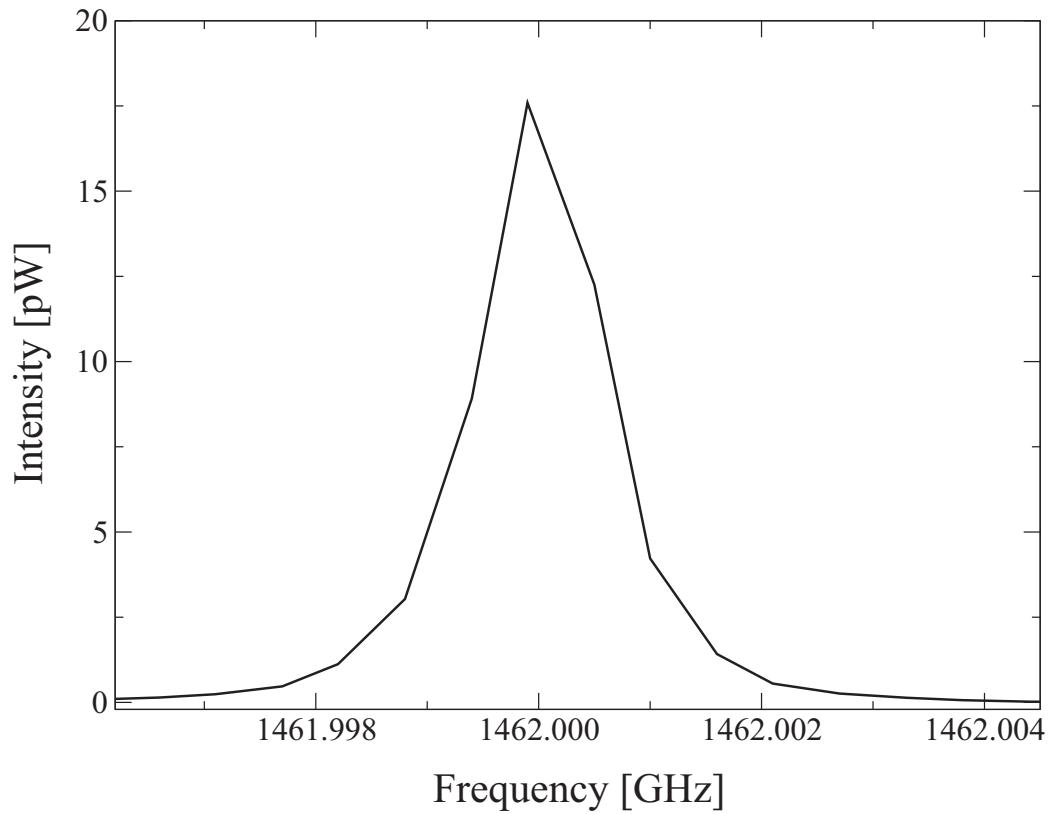


Figure 9.11: Signal of the 17th harmonic generated by the SL multiplier, detected with the CONDOR heterodyne receiver and the AOS.

Calibration with Hot-Cold-Load

The 17th harmonic of the SL at 1.462 THz has been detected in heterodyne mode with the AOS. Hot and cold load spectra have been recorded in order to calibrate the intensity. Each channel of the spectrum shown in Fig. 9.11, has been calibrated using

$$P_{power} = k_B \cdot 0.558 \text{ MHz} \cdot (295 \text{ K} - 77 \text{ K}) \cdot \frac{z_{SL}}{z_{hot} - z_{cold}} \quad (9.9)$$

The power of the SL signal is distributed over several channels (spacing = 558 kHz) of the AOS spectrometer. The total power of the 17th harmonic generated by the SL is achieved by summing the power recorded in each channel. Thus a total power of 50 pW is achieved. Considering the multiplication efficiency derived in Sec. 8.3.1, a power level between 2 and 200 pW was expected. A power level of 2 pW is expected for the 17th harmonic if the input frequency is 115 GHz as in Sec. 8.3.1. If the expected power is calculated using 0.053 ± 0.004 dB/GHz, 200 pW, is expected. As the input frequency is lower than in Sec. 8.3.1 a power level in between is expected, which is in good agreement with the 50 pW determined by the heterodyne detection.

9.2.7 Absorption Spectra

Absorption spectra of D₂O at $f = 1461.573$ GHz ($J_{K_a, K_c} = 9_{4,5} - 9_{3,6}$) were recorded at two different pressures ($p_1 = 8$ μ bar, $p_2 = 25$ μ bar) using the configuration shown in Fig. 9.9. In comparison to the setup used for the emission spectra (Sec. 9.2.2), the liquid nitrogen background source was replaced by a monochromatic radiation source. The radiation is generated by a phase-locked Gunn oscillator running at frequencies around 90 GHz, which feeds the input of a SL frequency multiplier. The 17th harmonic generated by the SL is detected by the CONDOR heterodyne receiver. For absorption spectra a 50 cm long absorption cell was inserted into the beam path. During the measurement, the LO frequency was fixed and only the SL frequency was varied. For each SL frequency one spectrum was recorded with the AOS backend. A closeup (Fig. 9.11) into one of these spectra shows the detected SL signal. Due to the fluctuation bandwidth of the AOS the monochromatic signal causes a Gaussian shaped peak and power is distributed over several adjacent channels. The signal-to-noise ratio of the SL signal (7000 counts) compared to the rms noise of the background (1.5 counts at $\tau_1 = 200$ ms, 0.3 counts at $\tau_2 = 5$ s) is 1/4600 at an integration time of $\tau_1 = 200$ ms and 1/23000 at $\tau_2 = 5$ s. The ratio of both signal-to-noise ratios is in agreement with the expected decrement of $\sqrt{\tau_1/\tau_2} = \sqrt{200/5000} = 0.2$. Thus, the rms noise for one single scan is $\sqrt{20} \cdot 1.5$ counts = 6.7 counts. This is in good agreement with the calculated rms noise, induced by the dark current in the CCD of the AOS, which is $\approx \sqrt{2} \cdot 3 = 4.2$ counts (the factor of $\sqrt{2}$ arises due to the subtraction of the zero-measurement) [104, 100]. However, strong signals (max. $2^{14} = 16384$ counts) cause shot noise in the CCD, which can exceed the noise contribution of the dark current. At around 16000 counts, roughly 10^6 electrons cause a SNR of $1000000/\sqrt{1000000} = 1000$, which corresponds to a rms noise of 16 counts. By integrating the intensity over the illuminated channels and assigning them to the frequency of the SL for all recorded AOS spectra, absorption spectra are obtained (Fig. 9.12). The spectra recorded at a pressure of 8 μ bar were recorded with an integration time of 5 s, whereas the spectra at a pressure of 25 μ bar were integrated over 200 ms. Despite the factor of 25 in integration time, both absorption spectra exhibit the same rms noise of 0.005 (determined at a position offset from the absorption peak). Although the rms noise is in good agreement with the calculated shot noise expected for the short scan (rms \approx 0.0035), the rms noise does not decrease with integration time and exceeds the calculated shot noise level of rms \approx 0.00068 for the 5 s long scan. This might be caused by slightly different amplifications in different AOS frequency channels, which are not taken into account, long term stability effects of the SL source and receiver system and the assumption that the total detected power of SL signal can be calculated as a Riemann sum. Both absorption spectra have been analyzed by fitting a Voigt-profile to the line shape, which reveals the absorptance. Taking the pressure into account as well as the absorption path length the intensities tabulated in Tab. 9.4 are obtained. The theoretical intensities are taken from the CDMS. Although the agreement between experimental and

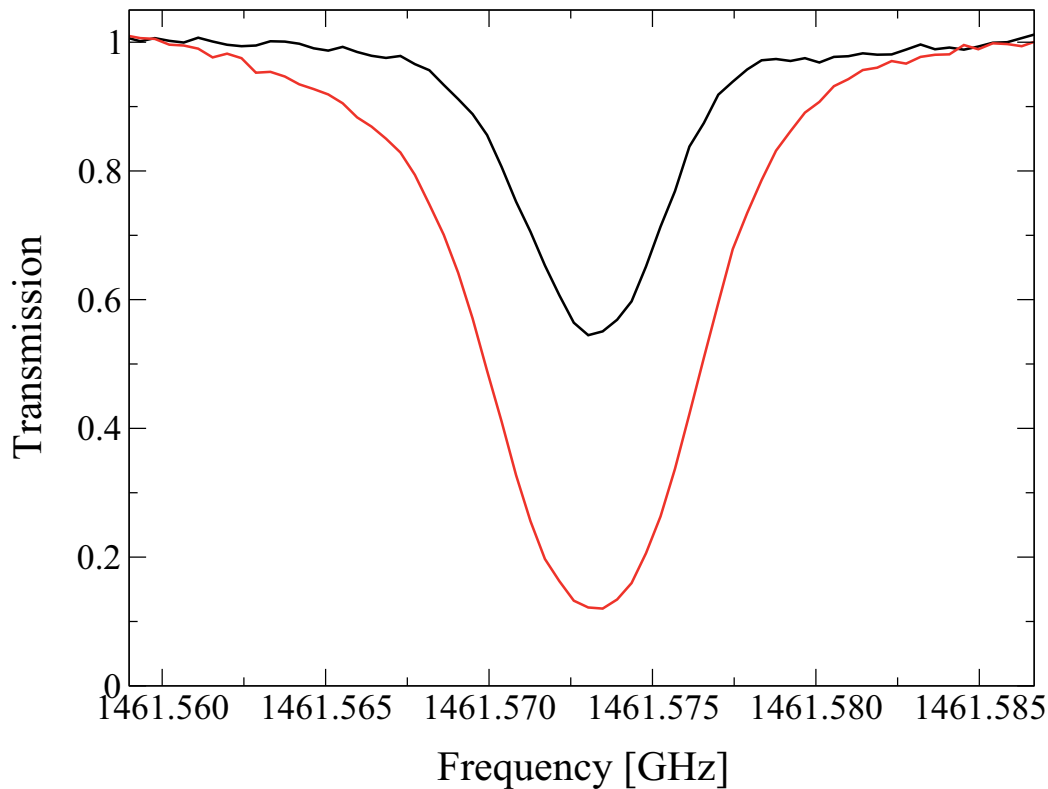


Figure 9.12: Absorption spectra of D_2O recorded with the CONDOR heterodyne system and the 17th harmonic generated by the SL. $J_{K_a, K_c} = 9_{4,5} - 9_{3,6}$ at pressures $p = 8\mu\text{bar}$ (black) and $p = 25\mu\text{bar}$ (red).

Table 9.4: Calculated and measured intensities derived from absorption spectra (Fig. 9.12) recorded at two different pressures. Calculated intensities are taken from the Cologne Database for Molecular Spectroscopy (CDMS).

Transition	Pressure [μbar]	Intensity [10^{-16} MHz/(molecules/cm ²)]
f=1461.573 GHz	calculated	3.342
$J_{K_a, K_c} = 9_{4,5} - 9_{3,6}$	8 ± 5	3.91 ± 1
	25 ± 5	4.76 ± 1

theoretical values is not as good as in Tab. 9.2, the results are quite consistent. As the spectral resolution of the AOS is not essential in this setup, because the frequency is known from the monochromatic source, different post detection techniques as discussed in the next Sec. 9.3, are favorable. They provide possible solutions in order to overcome the limitations caused by the AOS.

9.3 Detection with Superlattice Mixers

In this section two alternative post detection methods will be discussed. If a monochromatic signal is detected with a heterodyne receiver as shown in Sec. 9.2.7, the spectral resolution provided by FFTS or AOS spectrometer

backends is not required in order to obtain the spectral resolution, because the benefit from simultaneously recording a broad frequency range is unused. Therefore, the two setups apply narrow bandpass filters (≈ 40 MHz, and ≈ 5 kHz) to the IF signal and detect only the power within this reduced bandpass without resolving the IF frequency.

9.3.1 Experimental Setups

In the setup discussed first, the intensity of the source signal is recorded by rectifying the squared IF signal after a bandpass filter. The second investigated approach makes use of a second mixer, which downconverts the IF signal to frequencies below 100 kHz. By tuning the LO of the heterodyne instrument appropriately, the second IF frequency can be constrained to an arbitrary fixed frequency. The amplitude of the latter IF frequency is measured after a narrow bandpass filter ($\Delta f = 5$ kHz) by an ordinary digital AC-voltmeter.

For this investigation a different heterodyne instrument is used, which works at room temperature up to 600 GHz and uses a superlattice (SL) as mixer element. As shown in Sec. 8.1, the strong non-linearity in the I/V-curve of SL devices makes them not only a good choice as frequency multiplier, but in addition such devices are also highly qualified to act as frequency mixers in phase locked loop circuits or heterodyne detectors as has been shown by Renk *et al.* [105] and Vaks *et al.* [106]. The block design of the SL is slightly changed in the mixer configuration. Instead of an input horn antenna, a bias connector is attached to the block through which the LO signal is fed into the SL mixer. Although the SL mixer is by far not as sensitive as SIS or HEB mixers, its simple setup configuration at room temperature makes it an interesting device for some heterodyne applications. In particular, it can be subharmonically operated using extremely large harmonics of the LO and thus, commercially available LOs running at medium and low frequencies (< 20 GHz) can be applied. Although stronger IF signals and thus a better sensitivity are expected at higher LO frequencies, the use of high harmonics simplifies the setup considerably, because LOs at low frequencies are more widespread. Also the signal linkage to the mixer is much easier to realize at low frequencies. In the measurements here the superlattice mixer is operated with harmonics in the order of the 19th up to 51st of a synthesizer running at frequencies around 16 GHz. By using appropriate harmonics the heterodyne detection system works continuously from frequencies of 240 up to at least 600 GHz. The IF frequency was in the vicinity of 350 MHz. The radiation is generated by a superlattice (SL) frequency multiplier, which is fed by the quadrupled frequency of a synthesizer with an estimated output power of approximately $200 \mu\text{W}$ at 240–360 GHz and $20 \mu\text{W}$ at 400–600 GHz, as discussed in Chp. 8.

9.3.2 Continuum Detector

In this setup, shown in Fig. 9.13, the amplified intermediate frequency at 350 MHz is rectified by an in-house developed continuum detector and subsequently demodulated by a lock-in amplifier. AM as well as FM modulation of the source signal can be used. The continuum detector has a frequency bandwidth of 330 to 370 MHz. The DME spectrum shown in Fig. 9.14 is recorded in $2f$ modulation using the $3rd$ harmonic generated by the SL frequency multiplier and an integration time $\tau = 10$ ms per frequency point. The pressure in the absorption cell was $20 \mu\text{bar}$. The rms signal-to-noise ratio obtained in this spectrum ($J_{K_a, K_c} = 17_{0,17} - 16_{1,16}$) is of the order of $\Delta I/I = 2 \cdot 10^{-3}$. The detection limit for this spectrometer setup can be estimated by calibrating the intensity scale by the use of calculated line intensities. Using the predictions derived in Part I, an absorptivity of 0.2 is obtained for the given conditions. Thus, the detection limit (SNR=1) is obtained at an absorbance of $A = 4.0 \cdot 10^{-5}$ after 1 s of integration time. This corresponds to an absorption coefficient of $\alpha = 1.47 \cdot 10^{-7} \text{ cm}^{-1}$ in the 300 cm long absorption cell. At a pressure of 10 mTorr and a linewidth of 1 MHz at half-width at half-height the minimum detectable line intensity (SNR=1) is $I = 4.8 \cdot 10^{-26} \text{ cm}^{-1}/(\text{molecules}/\text{cm}^{-1})$ after 1 s integration time per frequency point.

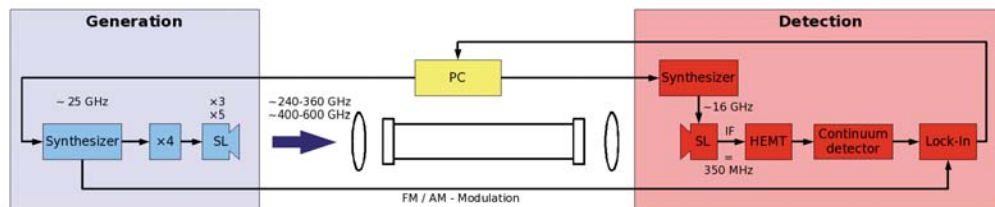


Figure 9.13: Schematic setup of the SL heterodyne spectrometer. The IF signal at 350 MHz is amplified by a HEMT, subsequently rectified in a continuum detector and finally analyzed by a Lock-In Amplifier. Amplitude and frequency modulation can be applied to increase sensitivity.

9.3.3 Double Heterodyne Detection

In this alternative setup the intermediate frequency at 350 MHz is amplified by a HEMT (bandwidth 320-380 MHz) and subsequently downconverted once more with a Schottky mixer and a second synthesizer (350.08 MHz) to obtain an intermediate frequency of 80 kHz. The amplitude of the IF signal is measured behind a narrow-bandpass filter ($Q=2-100$) by a digital voltmeter (Keithley 2000). No modulation is used, but as in AM detection, the obtained spectra can be calibrated, which allows to measure line intensities. Rotational spectra of DME have been measured at various frequencies in region of 300 GHz and 500 GHz using the $3rd$ and $5th$ harmonic generated by the SL. Two exemplary spectra are shown in Fig. 9.16, which were

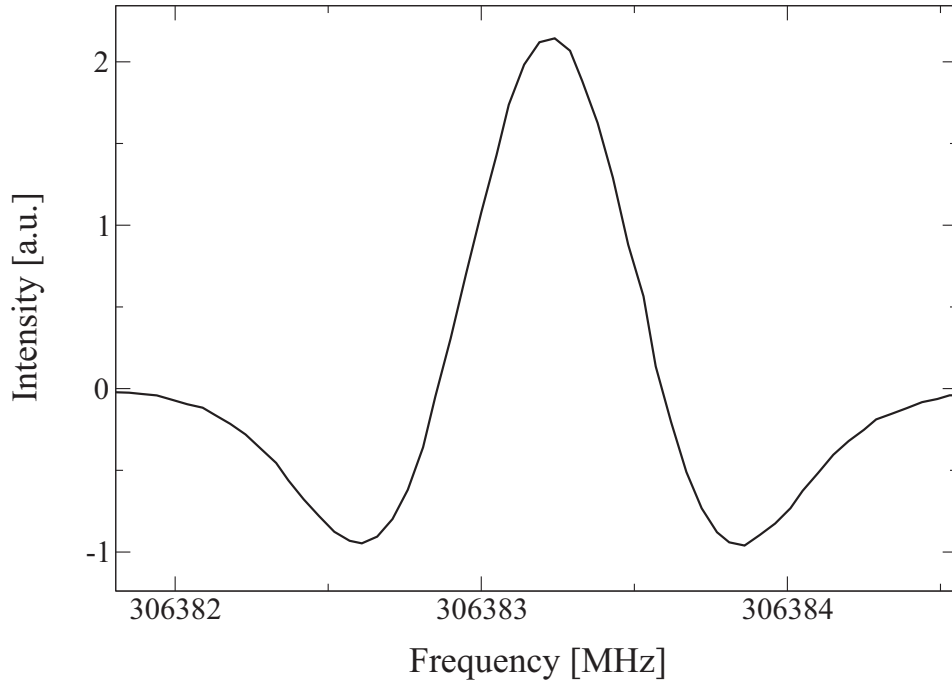


Figure 9.14: Rotational transition within the vibrational groundstate of DME recorded in $2f$ modulation with the 3rd harmonic generated by the SL frequency multiplier as radiation source ($J_{K_a, K_c} = 17_{0,17} - 16_{1,16}$). The pressure in the 3 m long absorption cell was 20 μ bar and an integration time of 10 ms per frequency point was used.

recorded at a pressure of 20 μ bar and an integration time of 4 ms per frequency point. The spectra represent typical results obtained at ~ 300 GHz (Fig. 9.16(a)) and ~ 500 GHz (Fig. 9.16(b)). Under consideration of pressure and absorption pathlength, intensities were determined, which are shown in Tab. 9.5. Calculated intensities were taken from predictions derived in Part I. They are in relative good agreement with the experimental values for the $J_{K_a, K_c} = 34_{4,31} - 34_{3,32}$ transition. The $J_{K_a, K_c} = 28_{1,28} - 27_{0,27}$ transition agrees within a factor of two. Both spectra have been analyzed in order to estimate the detection limit of this spectrometer configuration. Therefore, the rms noises of both spectra were determined. A signal-to-noise ratio of one is obtained if the absorptivity equals the noise level. The rms noises determined in these spectra are $\Delta I/I = 5 \cdot 10^{-4}$ at 300 GHz and $\Delta I/I = 2 \cdot 10^{-3}$ at 500 GHz. Hence, after 1 s of integration time per frequency point, absorptivities of $A_{min} = 3.2 \cdot 10^{-5}$ (300 GHz) and $A_{min} = 1.3 \cdot 10^{-4}$ are expected to be detectable with an SNR of unity. The detection limit at 1 mm wavelength is thus quite similar between both post detection techniques.

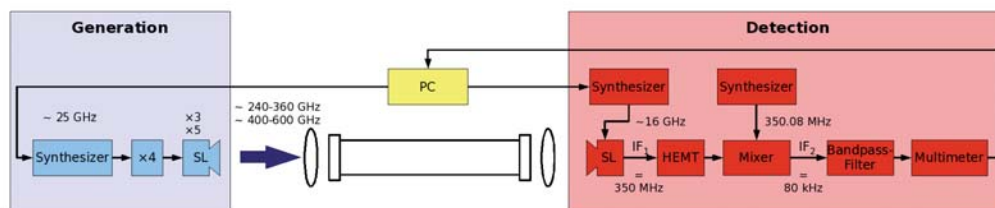


Figure 9.15: Schematic setup of SL heterodyne spectrometer using a second mixer to obtain an IF frequency below 100 kHz. The amplitude of this IF signal is finally measured after a narrow bandpass filter by an ac-voltmeter.

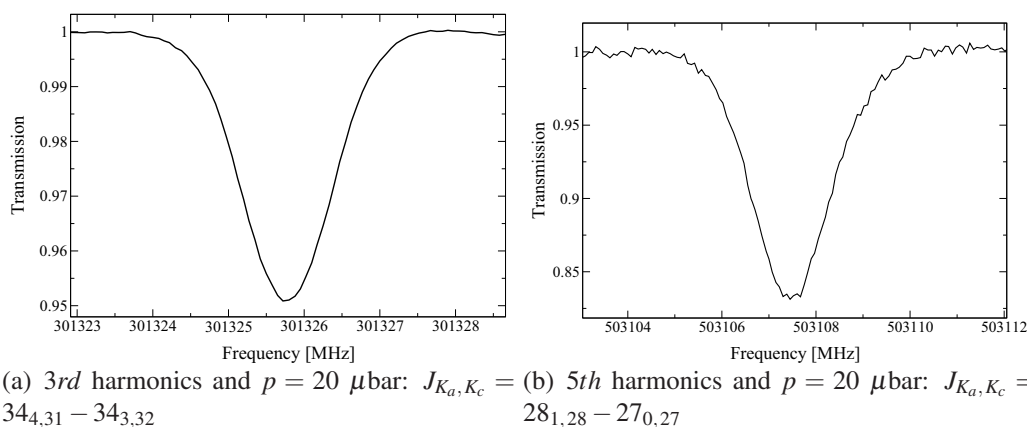


Figure 9.16: Rotational transitions within the vibrational groundstate of DME recorded without modulation using the 3rd (a) and 5th (b) harmonic generated by the SL frequency multiplier as radiation source. Both spectra were recorded at a pressure of 20 μ bar and an integration time of 4 ms per frequency point.

9.3.4 Bolometer

In common absorption spectrometers using bolometric detectors, the sensitivity of the spectrometer is usually not limited by the NEP of the bolometer. Often the detected noise level is dominated by noise contributions due to amplitude fluctuations of the source signal. It is therefore difficult to give a general statement for the detection limit of bolometers as it is strongly correlated to the quality of the source signal. For comparison here, the rotational spectra of CO, discussed in Sec. 8.3.1, have been investigated in terms of their signal-to-noise ratio. They have been recorded with comparable sources. The SNR determined in these spectra is the peak intensity compared to the rms noise level. For all recorded transitions, the absorptivity for the given conditions has been calculated using line intensities provided by the CDMS. The absorptivity at the detection limit A_{min} (SNR=1) is calculated as the quotient of the absorptivity at the center frequency divided by the SNR. The SNR values have been multiplied by $\sqrt{(1000.s/360.s)}$ in order to give the SNR regarding 1 s of integration time for better comparison. In Tab. 9.6, a summary of the results is shown. The table also shows the absorption coefficient and the line intensity at the detection limit related to an absorption

Table 9.5: Calculated and measured intensities derived from absorption spectra (Fig. 9.16) recorded at a pressure of 20 μ bar. Calculated intensities are taken from predictions obtained in part I.

Transition	Frequency	Calc. Intensity	Exp. Intensity
	[MHz]	[$10^{-23} \text{ cm}^{-1}/(\text{molecules}/\text{cm}^2)$]	
$J_{K_a, K_c} = 17_{0,17} - 16_{1,16}$	306383.2	11.1	
$J_{K_a, K_c} = 34_{4,31} - 34_{3,32}$	301325.5	2.72	2.43
$J_{K_a, K_c} = 28_{1,28} - 27_{0,27}$	503107.3	26.2	12.5

Table 9.6: Sensitivity obtained with InSb Bolometers. The absorptivity at the detection limit A_{min} (SNR=1) is calculated as the quotient of the absorptivity at the center frequency divided by the SNR. The SNR values have been multiplied by $\sqrt{(1000s/360s)}$ in order to give the SNR regarding 1 s of integration time for better comparison. Absorption coefficients α_{min} , and the line intensity I_{min} at the detection limit are related to an absorption pathlength of 300 cm, sample pressure of 10 mTorr, and a linewidth of 1 MHz half width at half height. A rough estimation of the noise equivalent power is given by ΔP , calculated as A_{min} times the estimated output power in the harmonic generated by the SL multiplier.

n	SNR	A_{min}	$\alpha_{min} [\text{cm}^{-1}]$	$I_{min} [\text{cm}^{-1} / \frac{\text{molecules}}{\text{cm}^2}]$	ΔP [nW]
3	10000	$4.6 \cdot 10^{-6}$	$1.3 \cdot 10^{-8}$	$5.0 \cdot 10^{-27}$	0.92
5	1000	$1.1 \cdot 10^{-4}$	$3.1 \cdot 10^{-7}$	$1.2 \cdot 10^{-25}$	0.39
7	130	$1.2 \cdot 10^{-3}$	$3.4 \cdot 10^{-6}$	$1.3 \cdot 10^{-24}$	0.28
9	25	$7.7 \cdot 10^{-3}$	$2.2 \cdot 10^{-5}$	$8.4 \cdot 10^{-24}$	0.16
11	5	$4.5 \cdot 10^{-2}$	$1.3 \cdot 10^{-4}$	$4.9 \cdot 10^{-23}$	0.10

pathlength of 300 cm, sample pressure of 10 mTorr, and a linewidth of 1 MHz half width at half height. The last column ΔP of the table shows the product of A_{min} and the estimated output power in the harmonic generated by the SL multiplier. This value gives a rough estimation of the noise equivalent power for this spectrometer setup. The decrease of ΔP matches with the frequency dependence of the bolometer specified by the manufacturer (QMC Instruments Ltd.).

9.4 Conclusion

The here presented investigations demonstrate the successful application of heterodyne detectors in laboratory spectroscopy in the Cologne laboratories. In particular, all experimental results agree with the underlying theory. The recorded emission spectra prove that achievable signal to noise ratios in these measurements can be estimated using the radiometer formula Eq. 9.6, i.e. the heterodyne receivers perform in the laboratory as predicted. Within reasonable integration times (not exceeding 1 hour), rms noises in the range of several 100 mK are achievable if the system temperature of the receiver sys-

tem is in the order of 1500 K. At an integration time of 8192 s absorptivities down to $1.5 \cdot 10^{-3}$ can be detected in emission with the NANTEN test receiver setup in the discussed configuration. Similar sensitivities are obtained in absorption with the 7th harmonic generated by the SL using an InSb bolometer for detection, if 8192 frequency points are subsequently recorded with an integration time of 1 s per point. Multiplier chains are nowadays available that generate several μW output power at around 1 THz. With such sources the sensitivity obtained in absorption applying InSb bolometers is expected to be around one order of magnitude more sensitive. The maximal signal strength in the emission spectra is limited by the temperature difference of the gas sample and the temperature of the absorber background. The maximum signal strength can thus be increased by the use of a hot background ($T > 533$ K) instead of the cold absorber background (e.g. glow bars) by heating the gas sample or if emission is induced in two-photon experiments. If radiation sources are used as background signals additional noise contributions have to be taken into account. In the recordings of the SL signal it has been shown that noise contributions of the spectrometer (AOS) dominate the spectrum.

As the IF spectrometer (AOS or FFTS) provides at least 1 GHz bandwidth, such configurations are also qualified to record time dependent spectra, which can be of interest for monitoring or for two-photon spectroscopy if the molecular lines are sufficiently strong. The FFTS used in these studies provides synchronization times down to 5 μs [92], which is thus the achievable time resolution for time-dependent studies based on this configuration. This spectral bandwidth combined with the time-resolution can therefore provide significant advantages for the search of new molecular species, in particular if they are unstable under laboratory conditions. Therefore, its combination with electrical discharge cells might be a promising future application.

In combination with monochromatic radiation sources, the signal frequency can be down-converted to any appropriate IF frequency and subsequently analyzed. As phase and amplitude information is conserved, digitizing the IF signal opens the opportunity to obtain extremely high time-resolution, which e.g. is desirable in molecular jet experiments. In molecular jet experiments, which use laser ablation sources, the pulse length of the molecular gas is usually in the order of 10 μs . While this time scale already reaches the limits of InSb bolometers particularly if FM modulation technique is applied, it is still several orders of magnitudes above the time resolution obtainable with heterodyne setups, which is currently limited by the post detection process.

The results obtained with the SL heterodyne setups demonstrate that these very compact detector systems already achieve good sensitivities at room temperature. At around 300 GHz, the achieved sensitivity is only one order of magnitude below the sensitivity obtained with the bolometer setup. Sensitivities at around 500 GHz are already quite comparable. This might be explained by the amplitude fluctuation noise generated by the third harmonic, which contributes to the noise detected with the bolometer, because

all odd harmonics are present in the SL signal. Due to the narrow band-pass in the heterodyne setup, only one harmonic is detected. As extremely high harmonics of the LO can be used for the downconversion process, the demands on the LO can easily be fulfilled by commercially available synthesizers connected via cable to the SL mixer. The replacement of the voltmeter in the double heterodyne detection system by an analog-to-digital converter is certainly a more appropriate solution. This will allow a complete computer based analysis of the recorded signal afterwards and will allow to fully time-resolve the signal only limited by the sampling speed. Probably digital filters may even improve the signal-to-noise ratio. Due to their compactness and their applicability at room temperature they are an interesting alternative to liquid He cooled bolometers.

Conclusion and Outlook

In the present thesis, an extensive dataset of pure rotational transitions within the vibrational ground state and the torsional excited states (10) and (01) has been worked out. This dataset comprises transitions covering the mm-wave region as well as THz frequencies up to around 2 THz and provides a reliable basis for the astronomical analysis of current and future spectra. The comparison with astronomical line surveys has revealed a variety of spectral features in each line survey, which can be explained by rotational transitions within the excited states. Especially the number of clear detections in the line survey of *G327.3 – 06* underlines the relevance of the torsional excited states for the analysis of astronomical observations. The new generation of telescopes will even provide increased sensitivity and new spectral ranges. In particular, the ALMA observatory will grant high spatial resolution and sensitivity by the use of interferometric techniques and the large number of antennas. It is expected that the spatial resolution will resolve regions obeying different environments concerning temperature and chemical composition. In the hottest environments, temperatures up to several hundreds of Kelvin are expected. At these temperatures, torsional levels of DME are substantially populated and the accurate knowledge of transition frequencies of their rotational spectrum become essential for the analysis.

Although the analysis of the excited states pinpointed to the limits of the applied computer programs ERHAM and SPFIT, the effective Hamiltonian suggested by P. Groner, on which these routines are based on, has proven to be robust and accurate enough to deal with this large dataset of experimental transitions. The consistent implementation in SPFIT or the inclusion of interaction terms in ERHAM, is expected to significantly improve the addressed inaccuracies, which currently still occur in the treatment of the excited states. Anyhow, the experimental datasets provide a reliable and comprehensive basis for the improvement of theoretical and computational concepts, e.g. the development of even more refined fitting routines. The spectroscopic parameters obtained by this effective Hamiltonian, have been used to interpolate the torsional potential functions, including infrared and Raman measurements as well as parameters obtained from the analysis of the pure rotational spectrum as shown in Chp. 4.5. This might provide important constraints and insights in the torsional motions.

Extensive laboratory measurements in the entire frequency range have been the prerequisite for deriving the accurate dataset of predicted transition frequencies due to the complexity of the rotational spectrum of DME. The spectral coverage has been granted by different spectrometers. Particularly, the introduction of the SL multiplier has been an essential tool to access even very high frequencies and to record broad scans at sub-mm wavelength. Within the scope of this thesis, the first successful application of a SL multiplier to laboratory spectroscopy is presented. Its properties like output power, frequency accuracy and spectral coverage have been discussed in detail. The recording of the D₂O transition at a frequency above 3 THz presents the current record of frequencies which have been so far achieved by frequency multiplication and has impressively demonstrated the potential of such devices. These investigations have been complemented by the application of heterodyne receivers, which have been used to study spectral purity and to extend the investigations towards output efficiency. Extended feasibility studies on heterodyne detection in laboratory spectroscopy have led to quantitative and qualitative insights, which provide a basis for the applicability and design of future spectrometers setups in the sub-mm and THz regime. For the first time, SL devices have been used as mixer elements in heterodyne receivers which have been used as room temperature detectors in a spectrometer. In combination with SL multipliers as radiation source, reasonable sensitivities have been achieved. Although they are not as sensitive as liquid He cooled InSb detectors, it has been shown by means of rotational spectra, that signal-to-noise ratios are achievable which are just one order of magnitude below the signal-to-noise ratio obtained with cryogenic detectors in a comparable setup. Furthermore they allow the selective detection of just one harmonic generated by the SL multiplier source with a very compact setup. Preliminary studies concerning high sensitive heterodyne detection with superconductive mixer elements have been performed. The analysis of emission spectra of rotational spectra against a cooled absorber background revealed that good signal-to-noise ratios are obtained, but signal-to-noise ratios achieved with ordinary absorption spectrometers are not entirely reached within comparable integration times. Signal-to-noise ratios might be increased considerably if either line emission is increased or the cold absorber background is replaced by a hot background ($T > 533$ K). This has to be shown in further studies. Nevertheless, the opportunity to observe broad spectra (>1 GHz) within short integration times (1s) might be a useful tool to monitor medium and strong transitions in time, and to identify transitions whose frequencies are largely unknown.

Part III

Appendix

A

Useful Tables

Table A.1: Permutation operations of the molecular symmetry group G_{36} . The labeling of the nuclei follows the notation shown in Fig.3.1. The element representing the class in the character table is shown in bold.

Operation	Position of the nuclei
E	(12345678)
(123)(456)	(31264578)
(132)(465)	(23156478)
(14)(26)(35)(78)*	(46513287)
(15)(24)(36)(78)*	(54621387)
(16)(25)(34)(78)*	(65432187)
(123)(465)	(31256478)
(132)(456)	(23164578)
(132)	(23145678)
(123)	(31245678)
(465)	(12356478)
(456)	(12364578)
(142635)(78)*	(54613287)
(152436)(78)*	(65421387)
(153624)(78)*	(46521387)
(416253)(78)*	(46532187)
(163425)(78)*	(54632187)
(143526)(78)*	(65413287)
(14)(25)(36)(78)	(45612387)
(15)(26)(34)(78)	(56431287)
(16)(24)(35)(78)	(64523187)
(142536)(78)	(64512387)
(263415)(78)	(45631287)
(351624)(78)	(56423187)
(416352)(78)	(45623187)
(534261)(78)	(64531287)
(625143)(78)	(56412387)
(23)(56)*	(13246578)
(23)(45)*	(13254678)
(23)(46)*	(13265478)
(12)(45)*	(21354678)
(12)(46)*	(21365478)
(12)(56)*	(21346578)
(13)(45)*	(32154678)
(13)(46)*	(32165478)
(13)(56)*	(32146578)

Table A.2: Character table of G_{36} , the molecular symmetry group of dimethyl ether. The irreducible representations of $C_{3v}^- \times C_{3v}^+$ are given in brackets behind the representations of G_{36} . The transformation of the torsional angles τ_1 , τ_2 as well as τ^+ and τ^- are also tabulated. In the last rows the corresponding operations of the symmetry groups $C_{3v}^- \times C_{3v}^+$ and C_{2v} are shown.

	E	(123)(456)	(14)(26)(35)(78)*	(123)(465)	(132)	(142635)(78)*	(14)(25)(36)(78)	(142536)(78)	(23)(56)*
	1	2	3	2	4	6	3	6	9
$A_1(A_1A_1)$	1	1	1	1	1	1	1	1	1
$A_2(A_2A_1)$	1	1	1	1	1	1	-1	-1	-1
$A_3(A_1A_2)$	1	1	-1	1	1	-1	1	1	-1
$A_4(A_2A_2)$	1	1	-1	1	1	-1	-1	-1	1
$E_1(EA_1)$	2	2	2	-1	-1	-1	0	0	0
$E_2(EA_2)$	2	2	-2	-1	-1	1	0	0	0
$E_3(A_1E)$	2	-1	0	2	-1	0	2	-1	0
$E_4(A_2E)$	2	-1	0	2	-1	0	-2	1	0
$G(EE)$	4	-2	0	-2	1	0	0	0	0
τ_1	τ_1	$\tau_1 + \frac{2\pi}{3}$	$-\tau_2$	$\tau_1 + \frac{2\pi}{3}$	$\tau_1 - \frac{2\pi}{3}$	$-\tau_2$	τ_2	$\tau_2 + \frac{2\pi}{3}$	$-\tau_1$
τ_2	τ_2	$\tau_2 + \frac{2\pi}{3}$	$-\tau_1$	$\tau_2 - \frac{2\pi}{3}$	τ_2	$-\tau_1 + \frac{2\pi}{3}$	τ_1	τ_1	$-\tau_2$
$\tau^+(A_2)$	τ^+	$\tau^+ + \frac{4\pi}{3}$	$-\tau^+$	τ^+	$\tau^+ - \frac{2\pi}{3}$	$-\tau^+ + \frac{2\pi}{3}$	τ^+	$\tau^+ + \frac{2\pi}{3}$	$-\tau^+$
$\tau^-(B_1)$	τ^-	τ^-	τ^-	$\tau^- + \frac{4\pi}{3}$	$\tau^- - \frac{2\pi}{3}$	$\tau^- - \frac{2\pi}{3}$	$-\tau^-$	$-\tau^- + \frac{2\pi}{3}$	$-\tau^-$
$C_{3v}^- \otimes C_{3v}^+$	$E \otimes E$	$E \otimes (C_{31}C_{32})$	$E \otimes C_{2z}$	$(C_{31}C_{32}^2) \otimes E$	$(C_{31}C_{32}^2) \otimes (C_{31}C_{32})$	$(C_{31}C_{32}^2) \otimes C_{2z}$	$C_{2x} \otimes E$	$C_{2x} \otimes (C_{31}C_{32})$	$C_{2x} \otimes C_{2z}$
C_{2v}	E	-	σ_{bc}	-	-	-	C_2	-	σ_{ab}

Table A.3: Direct products of the elements of the molecular symmetry group G_{36}

	A1	A2	A3	A4	E1	E2	E3	E4	G
A1	A1	A2	A3	A4	E1	E2	E3	E4	G
A2	A2	A1	A4	A3	E1	E2	E3	E4	G
A3	A3	A4	A1	A2	E2	E1	E3	E4	G
A4	A4	A3	A2	A1	E2	E1	E4	E3	G
E1	E1	E2	E3	E4	A1 ⊕ A2 ⊕ E1	A3 ⊕ A4 ⊕ E2	G	G	E3 ⊕ E4 ⊕ G
E2	E2	E1	E4	E3	A3 ⊕ A4 ⊕ E2	A1 ⊕ A2 ⊕ E1	G	G	E3 ⊕ E4 ⊕ G
E3	E3	E4	E3	E4	G	G	A1 ⊕ A3 ⊕ E3	A2 ⊕ A4 ⊕ E4	E1 ⊕ E2 ⊕ G
E4	E4	E3	E4	E3	G	G	A2 ⊕ A4 ⊕ E4	A1 ⊕ A3 ⊕ E3	E1 ⊕ E2 ⊕ G
G	G	G	G	G	E3 ⊕ E4 ⊕ G	E3 ⊕ E4 ⊕ G	E1 ⊕ E2 ⊕ G	E1 ⊕ E2 ⊕ G	A1 ⊕ A2 ⊕ A3 ⊕ A4 ⊕ E1 ⊕ E2 ⊕ E3 ⊕ E4 ⊕ G

Bibliography

- [1] P. Schilke, T.D. Groesbeck, G.A. Blake, and T.G. Phillips. A line survey of Orion KL from 325 to 360 GHz. *Astrophys. J. Suppl. Ser.*, 108:301–337, 1997.
- [2] P. Schilke, D. J. Benford, T. R. Hunter, D. C. Lis, and T. G. Phillips. A line survey of Orion-KL from 607 to 725 GHz. *Astrophys. J. Suppl. Ser.*, 132:281–364, 2001.
- [3] L. E. Snyder, D. Buhl, P. R. Schwartz, F. O. Clark, D. R. Johnson, F. J. Lovas, and P. T. Giguere. Radio Detection Of Interstellar Dimethyl Ether. *Astrophys. J.*, 191:L79–L82, 1974.
- [4] R.T. Garrod and E. Herbst. Formation of methyl formate and other organic species in the warm-up phase of hot molecular cores. *Astron. Astrophys.*, 457:927–936, 2006.
- [5] R. T. Garrod, S. L. W. Weaver, and E. Herbst. Complex chemistry in star-forming regions: An expanded gas-grain warm-up chemical model. *Astrophys. J.*, 682:283–302, 2008.
- [6] R. J. Myers and E. B. Wilson. Application of Symmetry Principles To The Rotation-Internal Torsion Levels Of Molecules With 2 Equivalent Methyl Groups. *J. Chem. Phys.*, 33:186–191, 1960.
- [7] U. Blukis, R. J. Myers, and P. H. Kasai. Microwave Spectra And Structure Of Dimethyl Ether. *J. Chem. Phys.*, 38:2753–2760, 1963.
- [8] J. R. Durig, Y. S. Li, and P. Groner. Analysis of torsional splittings in the microwave spectra of dimethylether, CH_3OCH_3 and its isotopes, CD_3OCH_3 and CD_3OCD_3 . *J. Mol. Spectrosc.*, 62:159–174, 1976.
- [9] F. J. Lovas, H. Lutz, and H. Dreizler. Microwave-Spectra Of Molecules Of Astrophysical Interest .17. Dimethyl Ether. *J. Phys. Chem. Ref. Data*, 8:1051–1107, 1979.
- [10] W. Neustock, A. Guarnieri, J. Demaison, and G. Wlodarczak. The Millimeter And Submillimeter-Wave Spectrum Of Dimethylether. *Z. Naturforsch., A: Phys. Sci.*, 45:702–706, 1990.

- [11] P. Groner, S. Albert, E. Herbst, and F. C. De Lucia. Dimethyl ether: Laboratory assignments and predictions through 600 GHz. *Astrophys. J.*, 500:1059–1063, 1998.
- [12] P. Groner. Effective rotational Hamiltonian for molecules with two periodic large-amplitude motions. *J. Chem. Phys.*, 107:4483–4498, 1997.
- [13] H. Lutz and H. Dreizler. Microwave-spectra of dimethylether (CH₃)₂O and (CD₃)₂O in excited torsional states. *Z. Naturforsch., A: Phys. Sci.*, 33:1498–1510, 1978.
- [14] Y. Niide and M. Hayashi. Microwave spectrum of two top molecules in the excited states dimethyl ether, dimethyl sulfide, and dimethyl silane. *J. Mol. Spectrosc.*, 223:152–165, 2004.
- [15] P. Groner and J. R. Durig. Analysis Of Torsional Spectra Of Molecules With 2 Internal C3V Rotors .2. Far IR And Low-Frequency Raman-Spectra Of Dimethylether Isotopes. *J. Chem. Phys.*, 66:1856–1874, 1977.
- [16] Y. G. Smeyers and M. N. Bellido. Internal Dynamics of Nonrigid Molecules .1. Application to Acetone. *Int. J. Quantum Chem.*, 19:553–565, 1981.
- [17] P. R. Bunker and P. Jensen. *Molecular Symmetry and Spectroscopy*. National Research Council Canada, Ottawa, Ottawa, 1998.
- [18] W. G. Fateley and F. A. Miller. Torsional Frequencies In The Far Infrared .2. Molecules With 2 Or 3 Methyl Rotors. *Spectrochim. Acta*, 18:977–993, 1962.
- [19] P. Groner. Large-amplitude motion tunneling parameters in effective rotational Hamiltonians from rotation-internal rotation theory. *J. Mol. Spectrosc.*, 156:164–189, 1992.
- [20] H. M. Pickett. The Fitting and Prediction of Vibration-Rotation Spectra with Spin Interactions. *J. Mol. Spectrosc.*, 148:371–377, 1991.
- [21] B. J. Drouin, J. C. Pearson, A. Walters, and V. Lattanzi. THz measurements of propane. *J. Mol. Spectrosc.*, 240:227–237, 2006.
- [22] J. K. G. Watson. Determination of centrifugal distortion coefficients of asymmetric-top molecules. *J. Chem. Phys.*, 46:1935–1949, 1967.
- [23] J. K. G. Watson. Aspects of quartic and sextic centrifugal effects on rotational energy levels. In J. R. Durig, editor, *Vibrational Spectra and Structure*, volume 6, chapter 1. Elsevier, Amsterdam, Oxford and New York, 1977, 1977.
- [24] W. Gordy and R. L. Cook. *Microwave Molecular Spectra*. John Wiley & Sons, 1984.

- [25] H. M. Pickett. Theoretical studies of internal rotation for an asymmetric top. *J. Chem. Phys.*, 107:6732–6735, 1997.
- [26] F. Lewen, R. Gendriesch, I. Pak, D. G. Paveliev, M. Hepp, R. Schieder, and G. Winnewisser. Phase locked backward wave oscillator pulsed beam spectrometer in the submillimeter wave range. *Rev. Sci. Instr.*, 69:32–39, 1998.
- [27] B. J. Drouin, F. W. Maiwald, and J. C. Pearson. Application of cascaded frequency multiplication to molecular spectroscopy. *Rev. Sci. Instr.*, 76:093113, 2005.
- [28] Y. Niide and M. Hayashi. Reinvestigation of microwave spectrum of dimethyl ether and $r(s)$ structures of analogous molecules. *J. Mol. Spectrosc.*, 220:65–79, 2003.
- [29] C. P. Endres, F. Lewen, T. F. Giesen, S. Schlemmer, D. G. Paveliev, Y. I. Koschurinov, V. M. Ustinov, and A. E. Zhucov. Application of superlattice multipliers for high-resolution terahertz spectroscopy. *Rev. Sci. Instr.*, 78:043106, 2007.
- [30] P. Groner. private communication, 2007.
- [31] P. Schilke. private communication, 2009.
- [32] A. Belloche, K. M. Menten, C. Comito, H. S. P. Müller, P. Schilke, J. Ott, S. Thorwirth, and C. Hieret. Detection of amino acetonitrile in Sgr B2(N). *Astron. Astrophys.*, 482:179–196, 2008.
- [33] A. Belloche. private communication, 2009.
- [34] S. Jørgensen-Bisschop. private communication, 2009.
- [35] E. Gibb, A. Nummelin, W. M. Irvine, D. C. B. Whittet, and P. Bergman. Chemistry of the organic-rich hot core G327.3-0.6. *Astrophys. J.*, 545:309–326, 2000.
- [36] P. Groner. Experimental two-dimensional torsional potential function for the methyl internal rotors in acetone. *J. Mol. Struct.*, 550:473–479, 2000.
- [37] H. S. P. Müller, F. Schlöder, J. Stutzki, and G. Winnewisser. The Cologne Database for Molecular Spectroscopy, CDMS: a useful tool for astronomers and spectroscopists. *J. Mol. Struct.*, 742:215–227, 2005.
- [38] H. S. P. Müller, S. Thorwirth, D. A. Roth, and G. Winnewisser. The Cologne Database for Molecular Spectroscopy, CDMS. *Astron. Astrophys.*, 370:L49–L52, 2001.

- [39] H. M. Pickett, R. L. Poynter, E. A. Cohen, M. L. Delitsky, J. C. Pearson, and H. S. P. Müller. Submillimeter, millimeter, and microwave spectral line catalog. *J. Quant. Spectrosc. Radiat. Transfer*, 60:883–890, 1998.
- [40] S. P. Belov, G. Winnewisser, and E. Herbst. The High-Resolution Rotational Torsional Spectrum Of Methanol From 0.55 To 1.2 Thz. *J. Mol. Spectrosc.*, 174:253–269, 1995.
- [41] F. Lewen, E. Michael, R. Gendriesch, J. Stutzki, and G. Winnewisser. Terahertz laser sideband spectroscopy with backward wave oscillators. *J. Mol. Spectrosc.*, 183:207–209, 1997.
- [42] E. Rusinek, H. Fichoux, M. Khelkhal, F. Herlemont, J. Legrand, and A. Fayt. Subdoppler Study of the ν_7 Band of C_2H_4 with a CO_2 Laser Sideband Spectrometer. *J. Mol. Spectrosc.*, 189:64–73, 1998.
- [43] K. M. Evenson, D. A. Jennings, and F. R. Petersen. Tunable far-infrared spectroscopy. *Appl. Phys. Lett.*, 44:576–578, 1984.
- [44] L. R. Zink, P. de Natale, F. S. Pavone, M. Prevedelli, K. M. Evenson, and M. Inguscio. Rotational far infrared spectrum of ^{13}CO . *J. Mol. Spectrosc.*, 143:304–310, 1990.
- [45] D. Rabanus, U.U. Graf, M. Philipp, O. Ricken, J. Stutzki, B. Vowinkel, M.C. Wiedner, C. Walther, M. Fischer, and J. Faist. Phase locking of a 1.5 Terahertz quantum cascade laser and use as a local oscillator in a heterodyne HEB receiver. *Opt. Express*, 17:1159–1168, 2009.
- [46] F. Lewen, S. P. Belov, F. Maiwald, T. Klaus, and G. Winnewisser. A quasi-optical multiplier for terahertz spectroscopy. *Z. Naturforsch., A: Phys. Sci.*, 50:1182–1186, 1995.
- [47] F. Maiwald, F. Lewen, V. Ahrens, M. Beaky, R. Gendriesch, A. N. Koroliev, A. A. Negirev, D. G. Paveliev, B. Vowinkel, and G. Winnewisser. Pure rotational spectrum of HCN in the terahertz region: use of a new planar Schottky diode multiplier. *J. Mol. Spectrosc.*, 202:166–168, 2000.
- [48] M. C. Wiedner, G. Wieching, F. Biela, K. Rettenbacher, N. H. Volgenau, M. Emprechtinger, U. U. Graf, C. E. Honingh, K. Jacobs, B. Vowinkel, K. F. Menten, L.-Å. Nyman, R. Güsten, S. Philipp, D. Rabanus, J. Stutzki, and F. Wyrowski. First observations with CONDOR, a 1.5 THz heterodyne receiver. *Astron. Astrophys.*, 454:L33–L36, 2006.
- [49] T. de Graauw, E. Caux, R. Güsten, F. Helmich, J. Pearson, T. G. Phillips, R. Schieder, X. Tielens, P. Saraceno, J. Stutzki, C. K. Wafelbakker, and N. D. Whyborn. The Herschel-Heterodyne Instrument for the Far-Infrared (HIFI). In *Bull. Am. Astron. Soc.*, page 1219, 2005.
- [50] R. A. Davies, M. J. Kelly, and T. M. Kerr. Tunneling between two strongly coupled superlattices. *Phys. Rev. Lett.*, 55:1114–1116, 1985.

- [51] L. Esaki and R. Tsu. Superlattice and negative differential conductivity in semiconductors. *IBM J. Res. Dev.*, 14:61, 1970.
- [52] A. Sibille, J. F. Palmier, H. Wang, and F. Mollot. Observation of Esaki-Tsu negative differential velocity in GaAs/AlAs superlattices. *Phys. Rev. Lett.*, 64:52–55, 1990.
- [53] E. Schomburg, T. Blomeier, K. Hofbeck, J. Grenzer, S. Brandl, I. Linggott, A. A. Ignatov, K. F. Renk, D. G. Paveliev, Yu. Koshurinov, B. Ya. Melzer, V. M. Ustinov, S. V. Ivanov, A. Zhukov, and P. S. Kop'ev. Current oscillation in superlattices with different miniband widths. *Phys. Rev. B*, 58:4035–4038, 1998.
- [54] A. Wacker and A. P. Jauho. Quantum transport: The link between standard approaches in superlattices. *Phys. Rev. Lett.*, 80:369–372, 1998.
- [55] M. Haeussler, R. Scheuerer, K. F. Renk, Yu. Koshurinov, and D. G. Paveliev. Microwave frequency multiplication by use of space charge domains in semiconductor superlattice. *Electron. Lett.*, 39:628–629, 2003.
- [56] R. Scheuerer, D. G. Paveliev, K. F. Renk, and E. Schomburg. Frequency multiplication using induced dipole domains in a semiconductor superlattice. *Physica E*, 22:797–803, 2004.
- [57] D. G. Paveliev, Y. I. Koshurinov, V. M. Ustinov, A. E. Zhukov, and P. S. Kop'ev. Investigation of the Detection, Mixing and Frequency Multiplication in the Planar Semiconductor Elements Based on the High Doped GaAs/AlAs, Superlattices in MM and Smm Wavelength Bands. *Phys. Eng. Millimeter and Submillimeter Waves“: symposium proceedings: Kharkov, Ukraine, June 4-9*, page 744, 2001.
- [58] D. G. Paveliev, Y. I. Koschurinov, F. Lewen, C. P. Endres, A. M. Baryshev, V. M. Ustinov, and A. E. Zhukov. Frequency dependence of the harmonic radiation power emitted by a GaAs/AlAs superlattice diode in the terahertz frequency range. In *The Joint 30th International Conference on Infrared and Millimeter Waves and 13th International Conference on Terahertz Electronics, 2005. IRMMW-THz 2005.*, volume 1, pages 140–141, 2005.
- [59] W. Caminati and J-U. Grabow. *Frontiers of Molecular Spectroscopy*, chapter Microwave spectroscopy: Experimental techniques. Elsevier, 2008.
- [60] R. D. Suenram, F. J. Lovas, G. T. Fraser, J. Z. Gillies, C. W. Gillies, and M. Onda. Microwave-spectrum, structure, and electric-dipole moment of Ar-CH₃OH. *J. Mol. Spectrosc.*, 137:127–137, 1989.
- [61] J. U. Grabow and W. Stahl. A Pulsed molecular-beam microwave Fourier-transform spectrometer with parallel molecular beam and resonator axes. *Z. Naturforsch.*, 45a:1043–1044, 1990.

- [62] C. Chuang, C. J. Hawley, T. Emilsson, and H. S. Gutowsky. Computer-based controller and averager for the Balle-Flygare spectrometer. *Rev. Sci. Instr.*, 61:1629–1635, 1990.
- [63] C. Keussen, R. Schwarz, U. Andresen, and H. Dreizler. Improved version of a microwave fourier-transform spectrometer in the frequency band from 26 to 40 GHz. *Z. Naturforsch.*, 45a:711–714, 1990.
- [64] J. U. Grabow, E. S. Palmer, M. C. McCarthy, and P. Thaddeus. Supersonic-jet cryogenic-resonator coaxially oriented beam-resonator arrangement Fourier transform microwave spectrometer. *Rev. Sci. Instr.*, 76:093106, 2005.
- [65] T. J. Balle and W. H. Flygare. Fabry-Perot cavity pulsed fourier-transform microwave spectrometer with a pulsed nozzle particle source. *Rev. Sci. Instr.*, 52:33–45, 1981.
- [66] W. F. Kolbe and B. Leskovar. 140-GHz pulsed Fourier-Transform Microwave Spectrometer. *Rev. Sci. Instr.*, 56:97–102, 1985.
- [67] D. Herberth. Aufbau eines all-solid-state MM-Spektrometers. Diploma thesis, University of Cologne, 2007.
- [68] M. Koerber, O. Baum, U. Hahn, J. Gauss, T. F. Giesen, and S. Schlemmer. The rotational gas-phase spectrum of trans- and cis-HSSOH at 100 GHz. *J. Mol. Spectrosc.*, 257:34–39, 2009.
- [69] G. Winnewisser. Spectroscopy in the terahertz region. *Vib. Spectrosc.*, 8:241–253, 1995.
- [70] G. Winnewisser, A. F. Krupnov, M. Y. Tretyakov, M. Liedtke, F. Lewen, A. H. Saleck, R. Schieder, A. P. Shkaev, and S. V. Volokhov. Precision broad-band spectroscopy in the terahertz region. *J. Mol. Spectrosc.*, 165:294–300, 1994.
- [71] K. F. Renk, A. Stahl, A. Rogl, T. Janzen, D. G. Paveliev, Y. I. Koshurinov, V. Ustinov, and A. Zhukov. Subterahertz Superlattice Parametric Oscillator. *Phys. Rev. Lett.*, 95:126801, 2005.
- [72] F. Klappenberger, K. N. Alekseev, K. F. Renk, R. Scheuerer, E. Schomburg, S. J. Allen, G. R. Ramian, J. S. S. Scott, A. Kovsh, V. Ustinov, and A. Zhukov. Ultrafast creation and annihilation of space-charge domains in a semiconductor superlattice observed by use of Terahertz fields. *Eur. Phys J. B*, 39:483–489, 2004.
- [73] A. A. Ignatov, F. Klappenberger, E. Schomburg, and K. F. Renk. Detection of THz radiation with semiconductor superlattices at polar-optic phonon frequencies. *J. Appl. Phys.*, 91:1281–1286, 2002.

- [74] E. Schomburg, M. Henini, J. M. Chamberlain, D. P. Steenson, S. Brandl, K. Hofbeck, K. F. Renk, and W. Wegscheider. Self-sustained current oscillation above 100 GHz in a GaAs/AlAs superlattice. *Appl. Phys. Lett.*, 74:2179–2181, 1999.
- [75] E. Schomburg, S. Brandl, S. Winnerl, K. F. Renk, Ledentsov. N. N., V. M. Ustinov, A. Zhukov, P. S. Kop'ev, H.-W. Hübers, J. Schubert, H. P. Röser, A. Rosenauer, D. Litvinov, D. Gerthsen, and J. M. Chamberlain. Miniband transport in a GaAs/AlAs superlattice with submonolayer barriers in a static and THz electric field. *Physica E*, 7:814–818, 2000.
- [76] S. Winnerl, E. Schomburg, S. Brandl, O. Kus, K. F. Renk, M. C. Wanke, S. J. Allen, A. A. Ignatov, V. Ustinov, A. E. Zhukov, and P. S. Kop'ev. Frequency doubling and tripling of terahertz radiation in a GaAs/AlAs superlattice due to frequency modulation of Bloch oscillations. *Appl. Phys. Lett.*, 77:1259–1261, 2000.
- [77] E. Schomburg, K. Hofbeck, R. Scheuerer, M. Haeussler, K.F. Renk, A.K. Jappsen, A. Amann, A. Wacker, E. Scholl, D.G. Pavel'ev, and Y.I. Koschurinov. Control of the dipole domain propagation in a GaAs/AlAs superlattice with a high-frequency field. *Phys. Rev. B*, 65:155320, 2002.
- [78] R. Scheuerer, K. F. Renk, E. Schomburg, W. Wegscheider, and M. Bichler. Nonlinear superlattice transport limited by Joule heating. *J. Appl. Phys.*, 92:6043–6046, 2002.
- [79] K. N. Alekseev, M. V. Gorkunov, N. V. Demarina, T. Hyart, N. V. Alexeeva, and A. V. Shorokhov. Suppressed absolute negative conductance and generation of high-frequency radiation in semiconductor superlattices. *Europhys. Lett.*, 73:934–940, 2006.
- [80] R. Scheuerer, M. Haeussler, K. F. Renk, E. Schomburg, Y. I. Koshurinov, D. G. Paveliev, N. Maleev, V. Ustinov, and A. Zhukov. Frequency multiplication of microwave radiation by propagating space-charge domains in a semiconductor superlattice. *Appl. Phys. Lett.*, 82:2826–2828, 2003.
- [81] J. W. Gewartowski and H. A. Watson. Principles of electron tubes. D. Van Nostrand Company, INC., New York, 1965.
- [82] G. Winnewisser, S. P. Belov, T. Klaus, and R. Schieder. Sub-Doppler measurements on the rotational transitions of carbon monoxide. *J. Mol. Spectrosc.*, 184:468–472, 1997.
- [83] F. Maiwald. Frequenzvervielfacher für die THz-Spektroskopie. PhD thesis, Universität zu Köln, 1998.

- [84] C. P. Endres, H. S. P. Müller, S. Brünken, D. G. Paveliev, T. F. Giesen, S. Schlemmer, and F. Lewen. High resolution rotation-inversion spectroscopy on doubly deuterated ammonia, ND₂H, up to 2.6 THz. *J. Mol. Struct.*, 795:242–255, 2006.
- [85] S. Brünken, H. S. P. Müller, C. P. Endres, F. Lewen, T. Giesen, B. Drouin, J. C. Pearson, and H. Mäder. High resolution rotational spectroscopy on D₂O up to 2.7 THz in its ground and first excited vibrational bending states. *Phys. Chem. Chem. Phys.*, 9:2103–2112, 2007.
- [86] CDMS. Cologne Database for Molecular Spectroscopy: <http://www.cdms.de>.
- [87] QMC Instruments Ltd. <http://www.terahertz.co.uk>.
- [88] Inc. IRLabs. www.irlabs.com.
- [89] F. C. De Lucia. Noise, detectors, and submillimeter-terahertz system performance in nonambient environments. *J. Opt. Soc. Am. B: Opt. Phys.*, 21:1273–1279, 2004.
- [90] M. Kenyon, P. K. Day, C. M. Bradford, J. J. Bock, and H. G. Leduc. Background-limited membrane-isolated TES bolometers for far-IR/submillimeter direct-detection spectroscopy. *Nucl. Instrum. Methods Phys. Res., Sect. A*, 559:456–458, 2006.
- [91] K Rohlfs and T. L. Wilson. Tools of Radio Astronomy. Springer, Berlin, 2nd ed. edition, 1996.
- [92] Radiometer Physics GmbH. RPG-FFTS Manual.
- [93] T. van Duzer and C. W. Turner. Principles of Superconductive Devices and Circuits. Prentice Hall PTR, 2nd ed. edition, 1998.
- [94] J. W. Kooi. Advanced Receivers for Submillimeter and Far Infrared Astronomy. PhD thesis, Rijksuniversiteit Groningen, 2008.
- [95] J. Zmuidzinas and P. L. Richards. Superconducting detectors and mixers for millimeter and submillimeter astrophysics. *proc. IEEE*, 92:1597–1616, 2004.
- [96] J. L. Hesler, W. R. Hall, T. W. Crowe, R. M. Weikle, B. S. Deaver, R. F. Bradley, and S. K. Pan. Fixed-tuned submillimeter wavelength waveguide mixers using planar Schottky-barrier diodes. *IEEE Trans. Microwave Theory Tech.*, 45:653–658, 1997.
- [97] T. de Graauw, N. Whyborn, E. Caux, T. Phillips, J. Stutzki, A. Tielens, R. Güsten, F. Helmich, W. Luinge, J. Martin-Pintado, J. Pearson, P. Planesas, P. Roelfsema, P. Saraceno, R. Schieder, K. Wildeman, and K. Wafelbakker. The Herschel-Heterodyne Instrument for the Far-Infrared (HIFI). In L. Paganì & M. Gerin, editor, *EAS Publications Series*, volume 34 of *EAS Publications Series*, pages 3–20, 2009.

- [98] V. Vassilev, D. Meledin, I. Lapkin, V. Belitsky, O. Nystrom, D. Henke, A. Pavolotsky, R. Monje, C. Risacher, M. Olberg, M. Strandberg, E. Sundin, M. Fredrixon, S. E. Ferm, V. Desmaris, D. Dochev, M. Pantaleev, P. Bergman, and H. Olofsson. A Swedish heterodyne facility instrument for the APEX telescope. *Astron. Astrophys.*, 490:1157–1163, 2008.
- [99] P. Muñoz, S. Bedorf, M. Brandt, T. Tils, N. Honingh, and K. Jacobs. Fabrication and characterization of phonon-cooled hot-electron bolometers on freestanding 2- μ m silicon nitride membranes for THz applications. *SPIE*, 5498:834–841, 2004.
- [100] J. Horn. The development of an array acousto-optical spectrometer. PhD thesis, University of Cologne, 1997.
- [101] D. W. Allan. Statistics of atomic frequency standards. *proc. IEEE*, 54:221, 1966.
- [102] O. Hachenberg and B. Vowinkel. Technische Grundlagen der Radioastronomie. B.I. Wissenschaftsverlag Mannheim/Wien/Zürich, 1982.
- [103] L. H. Xu. private communication, 2009.
- [104] R. Schieder. private communication, 2009.
- [105] K.F. Renk, A. Rogl, B.I. Stahl, A. Meier, Y.I. Koschurinov, D.G. Paveliev, V. Ustinov, A. Zhukov, N. Maleev, and A. Vasilyev. Semiconductor-superlattice frequency mixer for detection of submillimeter waves. *Int. J. of Infrared and Millimeter Waves*, 27:373–380, 2006.
- [106] V. L. Vaks, Y. I. Koshurinov, D. G. Paveliev, and A. N. Panin. Development and design of a phase-locked loop in the subterahertz and terahertz ranges for a harmonic of the signal of a centimeter-wave synthesizer. *Radiophys. Quantum Electron.*, 48:831, 2005.

Danksagung

An dieser Stelle möchte ich mich herzlich bei allen bedanken, die zum Gelingen dieser Arbeit und zu der außergewöhnlich guten Arbeitsatmosphäre am Institut beigetragen haben. Ich danke insbesondere

- Prof. Dr. Thomas Giesen für die Betreuung dieser Arbeit und für die vielfältige intensive fachliche und private Unterstützung, die ich immer von ihm erfahren habe
- Prof. Dr. Stephan Schlemmer, der stets ein offenes Ohr für meine Anliegen hatte, mit viel Interesse das Fortschreiten meiner Arbeiten verfolgte und sich als Zweitgutachter zur Verfügung stellte
- Prof. Dr. Per Jensen, der er sich freundlicherweise zur Übernahme des Drittgutachtens bereit erklärt hat
- Prof. Dr. Axel Klein für die Bereitschaft, den Vorsitz der Disputationsprüfung zu übernehmen
- Dr. Frank Lewen für seine engagierte fachliche und technische Unterstützung, die wesentlich zum Gelingen der Arbeit beigetragen hat, sowie für die ausführlichen Gespräche und die gemeinsamen Stunden auf der Suche nach neuen Frequenzrekorden
- Dr. Brian Drouin and Dr. John Pearson from the spectroscopy group at the JPL for supplying me with spectra of DME and providing me precious assistance with the SPFIT routine
- Prof. Dr. Peter Groner für sein stets schnelles Feedback, seine fachliche Unterstützung und die Bereitstellung der in Columbus gemessenen Spektren
- Dr. D.G. Paveliev for his collaboration and the exciting SL devices
- den Instrumentierungsgruppen von Dr. Martina Wiedner, Dr. Urs Graf und Dr. Karl Jacobs, die die Messungen mit den zwei Heterodyn-Empfängern CONDOR und dem NANTEN2 Testempfänger ermöglichten, sowie Oliver Ricken, Dr. Patrick Pütz und Dr. Netty Honingh für ihre Hilfe bei den Messungen

- Prof. Dr. Peter Schilke, Dr. Suzanne Jørgensen-Bisschop und Dr. Arnaud Beloeche für ihre Anpassung meiner Daten an ihre astronomischen Spektren und die Zeit die sie sich dafür genommen haben
- Dr. Holger Müller für die gute Zusammenarbeit und die vielen Tipps bezüglich der Anpassung, die mir eine wertvolle Hilfe waren
- Dr. Sandra Brünken, die mir vor allem in der Anfangszeit engagiert beistand, mich mit zahlreichen Diskussionen und wichtigen Anregungen begleitet hat und meine Arbeit Korrektur las
- Dr. Frank Schmüling und Dr. Frank Schlöder für die umfangreiche Hilfestellung und die Geduld bei der Lösung aller Probleme, die ich mit meinem Computer hatte
- Dr. Karl Jacobs für die dichroischen Filter, mit denen das SL Spektrometer jetzt noch besser funktioniert
- Dr. Bernd Vowinkel, der mir häufig mit diversen Messgeräten, Verstärkern und Dioden ausgeholfen hat
- Dr. Patrick Pütz, Dr. Frank Lewen, Monika Koerber, Prof. Dr. Thomas Giesen sowie Indira Menke für das Korrekturlesen dieser Arbeit
- allen restlichen Mitgliedern der Spektroskopie-Gruppe für die tolle Zeit und die nette Arbeitsatmosphäre, vor allem meinen langjährigen Mitstreitern Dr. Petra Neubauer-Guenther, Dr. Oliver Baum, Dr. Michael Caris, Dr. Oskar Asvany, Dr. Leonid Surin, Monika Koerber, Doris Herberth, sowie Sabrina Gärtner für die leckeren Kuchen, Volker Lutter für Geschichten aus anderen Welten und meinen Zimmerkollegen Jürgen Krieg, Matthias Ordu und André Klemann für unterhaltsame Stunden
- allen Mitarbeitern der Feinmechanikwerkstatt für die stets schnelle und zuverlässige Anfertigung der Werkteile
- meiner Frau Sonja, die mich in all den Jahren mit viel Geduld begleitet und mir immer mit Rat und Tat zur Seite gestanden hat. Ohne sie wäre die Arbeit sicherlich nicht möglich gewesen.

Köln, im Oktober 2009

Erklärung

Ich versichere, dass ich die von mir vorgelegte Dissertation selbstständig angefertigt, die benutzten Quellen und Hilfsmittel vollständig angegeben und die Stellen der Arbeit - einschließlich Tabellen, Karten und Abbildungen-, die anderen Werken im Wortlaut oder dem Sinn nach entnommen sind, in jedem Einzelfall als Entlehnung kenntlich gemacht habe; dass diese Dissertation noch keiner anderen Fakultät oder Universität zur Prüfung vorgelegen hat; dass sie - abgesehen von unten angegebenen Teilpublikationen - noch nicht veröffentlicht worden ist sowie, dass ich eine solche Veröffentlichung vor Abschluss des Promotionsverfahrens nicht vornehmen werde.

Die Bestimmungen der Promotionsordnung sind mir bekannt. Die von mir vorgelegte Dissertation ist von Herrn Prof. Dr. T. F. Giesen betreut worden.

Teilpublikationen

- C. P. Endres, B. J. Drouin, J. C. Pearson, H. S. P. Müller, F. Lewen, S. Schlemmer, and T. F. Giesen. Dimethyl ether: laboratory spectra up to 2.1 THz. *Astron. Astrophys.* 402, 635–640, 2009
- C. P. Endres, F. Lewen, T. F. Giesen, S. Schlemmer, D. G. Paveliev, Y. I. Koschurinov, V. M. Ustinov, A. E. Zhucov. Application of superlattice multipliers for high-resolution terahertz spectroscopy. *Rev.Sci.Instr.* 78, 043106, 2007
- C. P. Endres, B. J. Drouin, J. C. Pearson, H. S. P. Müller, F. Lewen, S. Schlemmer, and T. F. Giesen. Dimethyl ether: Rotational spectra within the excited torsional states. in prep.
- S. Brünken, H. S. P. Müller, C. Endres, F. Lewen, T. Giesen, B. Drouin, J. C. Pearson, H. Mäder. High resolution rotational spectroscopy on D₂O up to 2.7 THz in its ground and first excited vibrational bending states. *Phys. Chem. Chem. Phys.* 9, 2103–2112 (2007)
- C. P. Endres, H. S. P. Müller, S. Brünken, D. G. Paveliev, T. F. Giesen, S. Schlemmer, F. Lewen. High resolution rotation inversion spectroscopy on doubly deuterated ammonia, ND₂H, up to 2.6 THz. *J. Mol. Struct.* 795, 242–255 (2006)

Lebenslauf

Christian P. Endres

Geburtstag: 9.2.1973
Geburtsort: Bergisch-Gladbach
Staatsangehörigkeit: deutsch
Familienstand: verheiratet

Schulausbildung

1979–1983 Süd-Schule Lechenich, Erftstadt
1983–1992 Städt. Gymnasium Erftstadt-Lechenich, Erftstadt
06/1992 Abitur

Studium

10/1992 Beginn des Studiums an der Universität zu Köln
Fachrichtung: Physik Diplom

10/2003–01/2005 Diplomarbeit am I. Physikalischen Institut
“Aufbau eines Multiplier-Terahertzspektrometers und seine Anwendung in der hochauflösenden Laborspektroskopie”

01/2005 Physik Diplom
02/2005 Beginn des Promotionsstudiums
Universität zu Köln

Berufserfahrung

07/1996–09/2003 Softwareentwickler,
KUTTIG Computeranwendungen GmbH, Troisdorf

10/2003–01/2005 Wissenschaftliche Hilfskraft am I. Physikalischen Institut
seit 02/2005 Wissenschaftlicher Mitarbeiter am I. Physikalischen Institut

